Structural Health Monitoring of Impact Damage for Composite Aircraft Structures

Investigating the Damage Severity Estimation of an Image Reconstruction Technique Using PZT Sensors

D.J. Mansvelder

TU Delft

KLM

Structural Health Monitoring of Impact Damage for Composite Aircraft Structures

Investigating the Damage Severity Estimation of an Image Reconstruction Technique Using PZT Sensors

by

D.J. Mansvelder

For obtaining the degree of Master of Science
in Aerospace Engineering at Delft University of Technology.

Thesis committee:		
Chair holder:	Dr. ir. R.C. Alderliesten	TU Delft
Comittee members:	Dr. D. Zarouchas	TU Delft
	Dr. B. Chen	TU Delft
	Ir. W. Kalfsbeek	KLM Engineering & Maintenance

Version	Final report –May 30, 2018
Student number:	4140923
Project duration:	July 1, 2017 – June 7, 2018

This thesis is confidential and cannot be made public until June 1, 2023.

TU Delft

KLM SKYTEAM

Acknowledgements

Firstly, I would like to thank my supervisor dr. D. Zarouchas for his guidance, feedback and support during the writing of this thesis. He provided many valuable suggestions and taught me the importance of one's individual engineering judgement. Moreover, I would like to thank my other supervisor ir. W. Kalfsbeek for his guidance, support, and for making it possible do research in an environment which allowed me to learn about the many different aspects of the MRO industry.
Also thanks to ir. P.A. Viegas Ochoa de Carvalho for his help and for making the complicated world of PZTs seem a little less complicated. I am furthermore grateful for the help of all the engineers at KLM Engineering & Maintenance, the technicians at the Delft Aerospace Structures and Materials Laboratory, and everyone else for their guidance and contribution in conducting this research and the experiments.
I am also very grateful to my family who have always showed their support and believe in me. And finally also thanks to my friends. It was great sharing the past years of studying together. Thanks for all your encouragement.

Summary

The high specific strength and stiffness of composite materials has resulted in a widespread introduction of composite structures in the commercial aviation industry. Although composite materials offer the possibility to design lightweight structures, they also suffer from complex failure modes of which the damage progression is not well understood. For the Maintenance, Repair and Overhaul (MRO) industry, this means that newer and smarter inspection methods of composite structures are required.

Composite aircraft structures are prone to impact resulting from for example ground operations, hail and, small size bird strikes which might result in Barely Visible Impact Damage (BVID). This type of internal damage may not be found during general visual inspections while conventional Non-Destructive Testing (NDT) techniques are expensive and time-consuming. Because BVID negatively affects the structural integrity, the industry fears this type of damage to be overlooked during ground operations and conventional inspections.

Structural Health Monitoring (SHM) systems are often put forward as an alternative to conventional inspection methods. SHM comprises a sensor or network of sensors embedded in or attached to a structure which can be used to determine the current state of the structure and monitor its deterioration over time. This new way of inspecting composite structures is often argued to be cheaper, faster and more safe as BVID needs not to be overlooked.

In this thesis the applicability of an active SHM method using image reconstruction is investigated from the perspective of an MRO. Piezoelectric (PZT) sensors are used to excite and capture a type of acoustic waves called Lamb waves which are sensitive to discontinuities inside a structure. An Image Reconstruction Algorithm (IMRA) was chosen, because it does not require all material properties to be known. By comparing the response of Lamb wave signals from the structure's pristine state to the current state, damage can be detected, located, and preferably also sized. This thesis aims to advance the understanding and functioning of IMRA by investigating the relationship between its outcome and damage severity. Sizing of damage using SHM would offer a great benefit to the MRO industry as this could lead to increased inspection intervals and deferred repairs.

The algorithm's behaviour is first analysed for a dataset obtained from the NASA Prognostics Data Repository. Damage Indices (DIs) based on the Pearson Correlation Coefficient (PCC) and the change in signal energy are used to compare response signals. It is found that delaminations cause a shift or mode conversion of the response signal which is detectable using the PCC, while the signal energy mainly captures disturbances from intralaminar matrix cracks. This finding suggests that damage types might be identified through the analysis of different DI formulations. It is also found that the excitation frequency of the wave excited by the actuator affects the DI's sensitivity to damage by a change in wavelength and its dispersive behaviour.

A case study is performed using composite panels resembling the Boeing 787's fuselage skin to evaluate IMRA's performance. Impact damage is induced and increased using a series of Quasi-Static Indentation (QSI) tests. The case study shows the importance of data acquisition, signal processing, and the complexity of validating an SHM system. It is demonstrated that not every NDT technique is capable of detecting the different damage mechanisms occurring after QSI. The study also shows that the quasi-isotropic lay-up of the test panels makes it more difficult to detect and identify damage compared to the cross-ply lay-up from the NASA dataset.

Finally, it is found that the failure of a sensor negatively affects the algorithm's capability to locate damage. Still, this should be further estimated during another test campaign for which the increase in damage is not only monitored using an SHM system but also using alternative techniques.

Overall, this report demonstrates the potential of an active SHM system based on acoustics to detect, locate, and monitor the growth of damage. However, the analysis also shows that the algorithm only works after a careful selection of several parameters which are identified as the limiting factors to IMRA.

For further research, it is thus recommended to explore the selection of these parameters by researching the relation between certain damage types and the specific DI formulations, able to capture this type of damage. Moreover, because of the difficulty to evaluate the performance of the algorithm, future research should focus on creating a database including data from the SHM system and conventional techniques. It could also be tried to combine newer techniques to validate the system's outcome. One possible solution would be to combine passive and active monitoring of impact damage.

Contents

Nomenclature

Table 1: List of abbreviations

Abbreviation	Definition
AD	Accidental Damage
AD	Airworthiness Directive
ADL	Allowable Damage Limits
AE	Acoustic Emission
ATL	Automated Tape Laying
BMS	Boeing Material Specification
BVID	Barely Visible Impact Damage
CBM	Condition-Based Maintenance
CFRP	Carbon Fiber Reinforced Polymer
CVM	Comparative Vacuum Monitoring
DASML	Delft Aerospace Structures & Materials Laboratory
DF	Data Fusion
DI	Damage Index
DOC	Direct Operating Costs
DSS	Door Surrounding Structures
DTL	Delamination Threshold Load
ED	Environmental Damage
FBG	Fiber Bragg grating
FD	Fatigue Damage
GW	Guided Waves
IBM	Inspection-Based Maintenance
IMRA	Image Reconstruction Algortihm
LVI	Low-Velocity Impact
MI	Mutual Information
MRB	Maintenance Review Board
MPD	Maintenance Planning Document
MRO	Maintenance, Repair and Overhaul
MSG	Maintenance Steering Group
NDT	Non-Destructive Testing
OEM	Original Equipment Manufacturer
PCC	Pearson's Correlation Coefficient
PIW	Pixel Influence Weight
PW	Plain Weave
PZT	Piezoelectric sensor
QSI	Quasi-Static Indentation
RAPID	Reconstruction Algorithm for Probabilistic Inspection of Defects
RDL	Repairable Damage Limits
RUL	Remaining Useful Life
SB	Service Bulletin
SH	Shear-Horizontal
SHM	Structural Health Monitoring
SRM	Structural Repair Manual
TAT	Turn-Around-Time
TBM	Time-Based Maintenance
ToA	Time of Arrival
UD	Uni-Directional
UT	Ultrasonic Testing

Table 2: List of symbols

Symbol	Definition	Units
σ_B	Standard deviation of baseline signal	[-]
σ_D	Standard deviation of damaged signal	[-]
β	Shape factor	[-]
ρ	Pearson Correlation Coefficient	[-]
μ_B	Mean of baseline signal	[V]
μ_D	Mean of damaged signal	[V]
a	Major axis	[m]
b	Minor axis	[m]
C_{BD}	Covariance between baseline and damaged signal	[-]
c_p	Phase velocity	[m/s]
d	Plate thickness	[m]
DI_{energy}	Damage Index based on signal energy	[-]
$DI_{pearson}$	Damage Index based on PCC	[-]
DI_{thres}	Threshold to DI value	[-]
E_B	Signal energy of baseline signal	$[V^2 \cdot s]$
E_D	Signal energy of damaged signal	$[V^2 \cdot s]$
f	Signal frequency	[Hz]
f_c	Central excitation frequency	[Hz]
f_s	Sampling frequency	[Hz]
n_c	Number of cycles in excited signal	[-]
n_s	Number of samples in x	[-]
n_r	Number of samples in first wave package of x	[-]
P_{change}	Change in pixel intensity	[-]
P_{int}	Pixel intensity	[-]
P_{thres}	Threshold to pixel intensity	[-]
R	Ratio between major axis and focal points	[-]
S	Pixel Distance Weight	[-]
V_{thres}	Threshold to relative pixel intensity	[-]
x	Lamb wave signal	[V]
x_h	Hilbert transform of signal x	[-]
x	X-coordinate of inspection area	[m]
x_{env}	Signal envelope of signal x	[-]
X_A,	X-coordinate actuator	[m]
X_B	Baseline signal	[V]
X_D	Damage signal	[V]
X_R,	X-coordinate receiver	[m]
y	Y-coordinate of inspection area	[m]
Y_A,	Y-coordinate actuator	[m]
Y_R,	Y-coordinate receiver	[m]

List of Figures

List of Tables

Introduction

Driven by the desire to reduce fuel consumption it is expected that by 2027, 58% of the commercial aircraft will belong to new-generation aircraft such as the Boeing 787 and Airbus A350 [1]. Besides having an effect on Original Equipment Manufacturers (OEMs) and aircraft operators, this will also affect the Maintenance, Repair & Overhaul (MRO) industry. While this industry keeps being pressured for a reduction in maintenance costs and an increase in fleet availability, the industry also has to familiarize itself with an increased use of composite materials in these aircraft designs.

The high specific strength and stiffness of composite materials offers the possibility to create structures with a high structural effectiveness allowing for lighter aircraft designs. However, their anisotropic behaviour also causes composite structures to show complex failure modes limiting the predictability of structural failures as little is known about damage progression inside these structures. As a result, composite designs as well as their maintenance programs often end up being conservative and therefore expensive in terms of both acquisition and their operational costs.

Composites aircraft structures are especially sensitive to a damage type called Barely Visible Impact Damage (BVID). This type of damage can result from Low-Velocity Impact (LVI) during ground operations, but also from a tool drop, small bird strike, or hail etc. It causes delaminations, intralaminar matrix cracks, and sometimes fiber failure to occur subsurface making a visual inspection impossible from the outside [2].

Moreover, if BVID grows unnoticed it can negatively affect the structural integrity which is why operators fear that this damage is overlooked. Moreover, the structural inspections of BVID which could be scheduled or triggered by a reported impact event are expensive and time-consuming. They require skilled personnel to perform Non-Destructive Testing (NDT) inspections such as an ultrasonic C-scan, Eddy current or X-ray inspection [3].

The primary goal of aircraft maintenance at MROs, is to achieve the highest availability and reliability of an airline's fleet in the most cost-effective way. Fundamental to aircraft maintenance are structural inspections, replacements and repairs. Its objective is to protect the continuous airworthiness of aircraft structures by evaluating deterioration from environmental, fatigue and accidental damage and, in the case of damage, retain their structural integrity [4].

Considering airframe or structural maintenance in particular, recently much research has been performed on Structural Health Monitoring (SHM). SHM could be seen as an alternative to NDT techniques by which the structural integrity can be monitored using NDT techniques attached to or embedded in the structure [5, 6]. This upcoming technology might be among the instruments which MROs can use to improve their composite maintenance and obtain a competitive advantage [7].

SHM shows a potential improvement of structural maintenance by introducing smarter and faster maintenance decision-making, reaching cost reductions by avoiding unnecessary (un)scheduled downtime, and by providing knowledge about the behaviour of damaged structures. With an increasing fleet of new-generation aircraft, the MRO KLM Engineering & Maintenance (E&M) also realises that SHM could be the future backbone of structural maintenance. For this reason, KLM E&M would like to investigate if SHM is applicable to the commercial aviation industry.

However, while SHM is presented as a potential solution or improvement by many in the research community, the technology is hardly ever applied in the commercial aviation industry. The implementation of SHM techniques progresses slowly and faces many challenges. Firstly, certification of a system is expensive and the business cases remain unclear. Furthermore, much of the research currently performed investigates damage localisation on very small structures with unrealistic types of damage, such as Teflon inserts to simulate delaminations. Many of the researched systems also require the design information of structures to be known while this is often only available to the OEM. This results in little validation data available for SHM systems in terms of their performance and their reliability. However, this is of key importance to the MRO industry as false-positive and false-negative results can affect costs and jeopardize safety.

A potential solution to this problem is the application of a type of ultrasonic waves, called guided waves. Guided waves are tiny elastic vibrations which can travel efficiently over relatively long distances in thin components such as panels and pipes [2]. They are extremely sensitive to changes in the properties of the medium they travel in and for this reason can be used in a variety of SHM applications. Recently much research has

been carried out on image reconstruction to localize damage of composite structures using guided waves. By extracting damage features from guided waves excited and captured by a network of piezoelectric (PZT) sensors, impact damage might be detected and located. For such a system to lead to immediate benefits, the algorithm is ideally also able to capture damage growth. Maintenance of a composite structure might then evolve from an Inspection-Based Maintenance (IBM) to a more Condition-Based Maintenance (CBM) strategy by deferring repairs or replacements to a moment of scheduled overhaul, which in term leads to financial benefits.

For these reasons, this research analyses the damage severity estimation capability of a data-analysis method for SHM data of composite structures using image reconstruction. Next to signal analysis and processing, this research also concentrates on the practicality of the system regarding the MRO environment, which is evaluated through multiple experiments on a Carbon Fiber Reinforced Polymer (CFRP) panel resembling the fuselage structure of a Boeing 787 with realistic impact damage. Lastly, sensor failure and its effect on the algorithm will be assessed as to the author's knowledge, no research has investigated the effects of sensor failure on image reconstruction algorithms yet. This research will thus not try to solve the lack of implementation of SHM in the commercial aviation industry, but should lead to more insight into image reconstruction for composite behaviour and might make MROs able to show OEMs and regulatory agencies that maintenance intervals can be increased or postponed as growth can be accurately monitored. Investigating such an analysis method which captures damage growth in a similar fashion to contemporary NDT techniques and does not require proprietary material information to be known, can therefore lead to a competitive advantage for MROs and be a major step forward in the application of SHM to the commercial aviation industry.

From this point of view, the research objective has been formulated:
To contribute to the further development of image reconstruction techniques for BVID by analysing the relationship between damage severity and damage probability distributions on one hand, and the effect of sensor failure on this probability distribution on the other.

The following research question is proposed:
What are the limits to an image reconstruction technique in terms of detecting, locating and quantifying BVID on CFRP structures with unknown material properties?

The following sub-questions have been formulated:

1. *"Can a relationship between the output of the image reconstruction and damage growth be found?"*
2. *"What is the influence of sensor failure on the damage locating and quantifying capability of the image reconstruction technique?"*

The first chapter of this report provides a general introduction to SHM. It elaborates on its main functions, motivation and position in the MRO industry. Chapter 2 explains why there is a benefit to be made from SHM of composite structures and what type of SHM system could be applied to monitor impact damage. The chapter also presents an introduction to the use of guided waves. Hereafter, the functioning of the image reconstruction algorithm is explained in Chapter 3. The output of the image reconstruction algorithm is analysed and verified in the subsequent chapter, Chapter 4. A case study using CFRP panels similar to the fuselage skin of the Boeing 787 is used for the validation of the algorithm in a more realistic environment. This is discussed in Chapter 5. Finally, the conclusions and recommendations for this research are discussed in the last chapter of this report, Chapter 6.

1

An Introduction to Structural Health Monitoring

In this chapter a general introduction to the principles of SHM is provided. The first section describes the functions of SHM. Hereafter, the main motivations for applying SHM are presented in Section 1.2. The third section, Section 1.3 analyses SHM in combination with the commercial aviation industry.

1.1. Defining structural health monitoring

The purpose of implementing an SHM system is to be able to continuously or with predefined intervals, monitor the health or deterioration of a structure by means of a sensor network which is either attached to or embedded in the structure [4]. The health state is determined by extracting damage characteristics from the SHM system's response data and analysed using physical and statistical models [8]. Literature generally defines five levels of SHM [9]:

- *Level 1 Detection:* The system gives an indication that damage is present in the structure.
- *Level 2 Localisation:* The system provides the location(s) of damage.
- *Level 3 Severity:* The system assesses the damage severity, e.g. the size of damage.
- *Level 4 Type:* The system identifies the damage type, e.g. delamination, intralaminar cracks, etc.
- *Level 5 Prediction:* The system provides an estimation on how damage progresses and the time to ultimate failure of the structure or its Remaining Useful Life (RUL).

In the short term SHM can be used to determine the structural integrity by rapid screening after the occurrence of discrete and unanticipated events like hard landings, impact with ground vehicles or bird strikes. When an SHM system is used to monitor a structure's response over time, it allows operators to monitor the accumulating structural damage that results from ageing and degradation from the operational environment.

Ideally, physical and statistical models can be used to diagnose damage, but can also be used to make predictions about future states of the structure. And eventually, SHM could be used to improve maintenance decision-making and lead to Condition-Based Maintenance (CBM) strategies. Operators will then not only be able to decide if immediate maintenance is necessary, i.e. repairs or replacements, but it will also allow them to make predictions about required maintenance activities and optimise their timelines in the future.

The next section investigates some of the reasons for applying SHM systems in the commercial aviation industry in more detail.

1.2. Motivating SHM

The main motivator for the implementation of SHM in the commercial aviation industry is a potential reduction of costs while maintaining a similar level of aviation safety. Currently, maintenance activities are estimated to be responsible for at least 12% of the Direct Operating Costs (DOC) [10]. Aircraft maintenance affects the financial situation of an operator in two ways. Firstly, maintenance itself, inspections, repairs and replacements, affect the direct costs of maintenance. Secondly, maintenance involves taking aircraft out of service which induces indirect maintenance costs due to a loss in aircraft availability. Consequently, by

achieving a reduction in inspection time, both direct and indirect financial benefits can be obtained. This section elaborates on the ways SHM leads to a potential reduction of costs.

Direct costs of maintenance
At KLM E&M, labour costs take up about 60% of the direct costs of airframe maintenance. When comparing SHM to conventional inspections, e.g. a general visual inspection, SHM requires less labour in terms of gaining access, surface preparations and inspection time [4].

Direct costs can furthermore be reduced using an SHM system by detecting damage at an earlier stage or by preventing unscheduled ground times due to unexpected damage. Alternatively, it allows operators to postpone repairs until an aircraft is scheduled for overhaul in case SHM allows them to monitor the propagation of damage [10]. Of course this should be in-line with the prescribed regulations.

SHM also offers the possibility to estimate the life span of structures in a more precise manner while local stresses and actual flight parameters can be measured for each aircraft individually. This can in the first place lead to life extensions of fatigue critical components or an adjustment of flight profiles to minimise operational loads [4]. It can also help MROs to save costs when reviewing Service Bulletins (SB) and Airworthiness Directives (AD), which are currently issued based on an aircraft's age in terms of flight hours or flight cycles. By assessing each aircraft individually, maintenance can be applied based on the aircraft's individual history [5].

Indirect costs of maintenance
Additionally, indirect costs of maintenance can be reduced by increasing structural inspection intervals. Nowadays, structural inspections are scheduled based upon the Maintenance Planning Document (MPD), which is provided by the OEM and among others contains the maximum allowed intervals between inspections. The OEMs use high safety factors to establish these intervals as they are standardized for all aircraft of a certain type and based upon assumptions of the loads and environmental operating conditions an aircraft experiences over time. An SHM system could furthermore allow for a more accurate measurement of the operating conditions, so that inspection intervals can be established more precisely, thereby making them less conservative [11].

Operational or usage monitoring using an SHM system furthermore provides a benefit to MROs which function as lessors. Instead of charging customers for lease time, they can charge them for the actual usage. As an example, aircraft which frequently fly through harsh environments like desserts, require longer and more costly forms of maintenance. On the other hand, it can also aid an MRO in case of warranty claims against OEMs or suppliers whose parts do not fulfil their intended function as contracted.

Learning from SHM
The paragraphs above have all prescribed a cost benefit to the MRO industry. However, SHM also allows to obtain a better understanding of a structure's behaviour. The increased use of composite materials in aircraft structures has added to the complexity of structural behaviour due to their anisotropy. While different failure modes of composite structures have been identified, little is known about what triggers them and how they interact. SHM can thus be used to monitor the behaviour of composite structures and improve our understanding of these failure modes. Lastly, SHM could also be used to establish databases for the statistical analysis of a certain material or structure.

1.3. SHM and the commercial aviation industry
In the previous sections, SHM has been introduced as an alternative to conventional NDT techniques. In order to understand how this relatively new technique fits into the MRO industry, a brief overview of aircraft maintenance strategies is provided in the first subsection. Hereafter, the second and third subsection discuss the implementation of SHM into the commercial aviation industry.

1.3.1. Aircraft maintenance strategies
Structural maintenance of aircraft structures comprises inspections, repairs and or replacements. In the early days aircraft structures were designed according to safe-life principles, which means that damage is not allowed to occur during a predefined design service life. Today, many structural components are based on a damage-tolerant design, implying that the process of damage development is understood well enough to be

controlled using a program of inspections which aims to detect damage well before it negatively affects flight safety. Damage-tolerant structures and structural maintenance therefore go hand in hand. The benefit of a damage-tolerant design philosophy is that it allows for lighter designs, and through the use of inspections, is often regarded to be safer than safe-life designs of which initial flaws or unexpected damage might grow unnoticed. However, it should be mentioned that several safety critical items or components which are hard to inspect are still designed according to a safe-life or fail-safe principle where redundancy is built into the design to avoid a loss of structural integrity, e.g. the primary structure of the main landing gear [11].

Not only did design philosophies change over time, also the view towards structural maintenance has changed. Where maintenance was initially perceived as an unavoidable and costly activity, it is now seen as a business which affects a company's profit by not only the direct costs of maintenance but also by the indirect costs through the operational efficiency and reliability. Besides, environmental concerns, the assurance of safe operation and ageing structures have contributed to operators acquiring multiple maintenance policies to increase the efficiency of their operation over time.

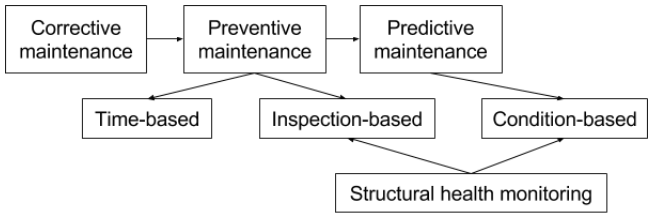

Figure 1.1: Evolution of structural maintenance strategies, based on [11].

Corrective maintenance

An evolution of several maintenance strategies is shown in Figure 1.1. In the early days, operators mainly used a form of corrective maintenance, also sometimes referred to as a fire-fighting strategy. This type of maintenance is not scheduled into the operation and components are only repaired or replaced in case they fail to perform their intended function. Nowadays, many companies have shifted towards a proactive strategy, which includes preventive as well as predictive maintenance strategies. The idea behind these is to prevent failure by repairing or replacing components prior to failure [11].

The advantage of utilising a corrective strategy is that structural components will be used for their full lifetime. Therefore, these structures are either designed according fail-safe or safe-life principles. The downside of this strategy is that it often leads to over-designed and thus heavier structures. Moreover, once failure of a structure is detected, the structure must be repaired during operable conditions. This can have large (financial) impacts on the operation of an airline as it leads to unplanned downtime. Lastly, while the structure is not inspected on a regular basis, secondary safety critical damage might be inflicted by failure of other components, impairing safety as well as maintenance costs [2].

Preventive maintenance

In the beginning, preventive maintenance strategies were often Time-Based (TBM), resulting in hard time limits. Assuming that the probability of failure increases with time, components are replaced, regardless of their RUL, after a fixed number of flight cycles, flight hours or days, etc. [11]. Although failure can be prevented in this way, the downside of TBM is that too conservative limits and thus too early replacements lead to high costs and low availability. On the other hand, too late replacements lead to unscheduled downtime and unexpected maintenance costs or failures.

A later form of preventive maintenance is Inspection-Based Maintenance (IBM). It aims to find the optimal timing for repairs or replacements based on the state of a damage-tolerant structure which is determined through frequent inspections. It is the kind of scheduled maintenance carried out at MROs today and replaces the hard time limits with the exception of structures designed according to the safe-life and fail-safe philosophy. Thus, current structural maintenance is based on a series of periodic inspections upon which further maintenance activities are based.

Advantages of a preventive maintenance strategy are that workloads and parts inventory can be planned according to the maintenance schedule. It was moreover shown that safer and more reliable operations were obtained than in the case of corrective maintenance. It leads to an overall increase of aircraft availability and allows for standard maintenance procedures, thereby obtaining a consistent quality [11]. On the other hand,

access to the structure is required every time a scheduled inspection is performed. This can lead to accidental damage or unexpected failure due to human errors.

Predictive maintenance
Taking preventive maintenance one step further leads to a predictive maintenance or CBM strategy. Based on predictions about the (future) condition of the structure, maintenance decisions are made with the aim to further increase fleet availability and reduce costs by avoiding unnecessary inspection and unexpected ground times. An important assumption for the use of predictive maintenance is that failure does not happen instantaneously, but there should be a process of degradation during which a structure evolves from going from a undamaged healthy state to a damaged state and subsequent failure.

Contemporary aircraft maintenance
From the paragraphs above might be concluded that acquiring an optimal maintenance strategy involves finding the lowest number of required maintenance activities and adopting intervals that are also adjusted to the flight schedule in a cost-effective manner while also maintaining a safe operation. Currently, this is mostly achieved in the form of preventive maintenance.

The Maintenance Steering Group 3 (MSG-3) document helps OEMs to build a maintenance program which allows operators to achieve such a maintenance strategy. It is widely used to create scheduled maintenance programs which ensures airworthiness of the aircraft throughout its operational life in an economical manner. The document contains guidelines to develop a maintenance schedule that is reliability-centred and accepted by regulatory agencies. It identifies the intervals at which tasks can be performed in order to obtain an efficient operation during which unnecessary maintenance is avoided and the reliability is kept high.

The tasks and intervals are included in the MPD which an OEM delivers with a new aircraft. It contains all obligated maintenance tasks approved by the Maintenance Review Board (MRB), which consists out of a team of regulatory personnel. The MPD can be adjusted by the MRB as experience with an aircraft type increases, e.g. an interval might be increased if it shows to be very conservative.

The first MSG document, MSG-1 was published in 1968 to guide the development of scheduled maintenance for the Boeing 747. Over the years, as the view towards maintenance changed, the MSG document evolved from a bottom-up approach (MSG-2) to a top-down approach (MSG3). Based on the MSG-3 approach, the economic and safety consequences of failure of each structural item are analysed and the item is evaluated for its susceptibility to the following damage categories [12]:

- *Accidental Damage (AD):* This form of damage results from a random discrete event, such as impact damage resulting from ground operations, natural hazards or bird strikes.
- *Fatigue Damage (FD):* Damage initiation and propagation resulting from cyclic loading of the structure. It is related to the usage of the aircraft.
- *Environmental Damage (ED):* Damage characterised by structural deterioration as a result of a chemical interaction with the operational environment. Damage from corrosion, temperature variations etc.

The first MSG-3 document contained three types of structural inspections, to which the author has referred before as conventional inspection methods. They are numbered one to three below. Since the 2009 revision of MSG-3, SHM is also mentioned as an inspection technique [12].

- **First version of MSG-3**
  1. *General Visual Inspection (GVI):* Which is often a visual examination of a structure from within touching distance.
  2. *Detailed Inspection (DET):* A more intensive examination of the structure with the use of extra lighting and inspection aids like mirrors or magnifying lenses.
  3. *Special Detailed Inspection (SDI):* An intensive examination of the structure which often uses a specialised inspection technique like NDT to evaluate the structure.
- **Added to the 2009 revision of MSG-3**
  4. *SHM*: Performing SHM according to a fixed schedule. Note that this type of inspection may only be performed when demonstrated to be applicable and effective. Hence, certification is needed to approve an inspection by SHM.

When referring back to Figure 1.1, SHM might indeed be placed under two maintenance strategies. Using SHM primarily to diagnose the current state of a structure can be placed under IBM. However when this data is used in combination with data from the structure's historical and future operational environment, SHM could eventually also be used for a predictive maintenance strategy.

However, the author is from the opinion that the MSG-3 process still needs adaptations before SHM can really be incorporated. Challenges are foreseen in the fact that SHM looks at individual components rather than groups of components while the data must be used in a top-down approach. This can become complicated when multiple SHM systems are to be combined. Moreover, SHM introduces a new type of output in case operators are going to predict failure. This will introduce difficulties as a Structural Repair Manual (SRM) only includes the instructions for a failed component. During such an event it is furthermore unclear what an operator must report back to an OEM. Predictive maintenance therefore introduces a new type of structural components which have not been included into the MSG-3 process yet; besides healthy structures and structures which have failed according to the SRM, there will also be structures which are labelled as: '*Going to fail if kept in service*'.

This might be one of the reasons why SHM has been mentioned in the MSG-3 2009 revision, but is not commonly applied to commercial aircraft. The next subsection will cover this into more detail.

1.3.2. Lack of integration

From the previous section can be concluded that there is a vast amount of literature which presents a variety of potential benefits resulting from SHM implementation. However, the technology seems to be hardly ever applied in the commercial aviation industry. This lack of integration might be due to the fact that many of the benefits presented at the beginning of this chapter are hard to quantify [13]. Evaluating financial benefits is complicated because most conventional inspections fit well into the maintenance program. It was for example found that when a structural inspection should take place inside one of the wings, often inspections of the electrical wiring at that location are scheduled according to the same interval. Therefore disassembly of several parts in order to provide access only has to be performed once.

Figure 1.2 shows a roadmap of SHM presented by Airbus in 2006. When reviewing literature it could be concluded that the implementation of SHM is currently still somewhere between Generation 0 and 1 [13]. Up till now, only one operator has demonstrated the use of an SHM system onto seven of their aircraft. Delta airlines has applied a Comparative Vacuum Monitoring (CVM) system to the shear fittings on the front spar of the wingbox on several Boeing 737's [13].

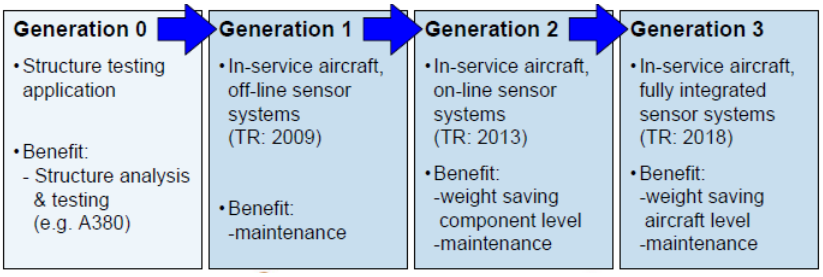

Figure 1.2: Roadmap of SHM presented by Airbus [5].

Besides being unable to quantify the benefits and consequently close the business cases for SHM, another important reason for the slow implementation of SHM systems is the fact that there is little validation data available, especially for composite structures [14]. This means that operators might have to generate and share (failure) data in order to train SHM algorithms. However, not all operators are willing to share data with other operators and or with regulatory agencies in order to certify a system. From the SHM application at Delta Airlines has been shown that the certification process requires a long-term reliability of the system under a harsh operational environment [13]. Therefore all kinds of tests must be performed which makes the certification not only complex much also very expensive. Nevertheless, SHM is already more often applied in military aviation. This is likely because costs are of less importance and the focus lies much more on life extension of structures using operational monitoring than on damage detection..

It was also found that when performing maintenance according to the current regulations, operators often have little interest in knowing about damage being present if this damage is below the critical damage size. This is due to the 'If you find something, you must fix it' rules [13]. This agrees with the author's own

experience and perspective of SHM at KLM E&M. When introducing the general methodology of SHM, many people were still unfamiliar with its principles and potential. While having no clear view on the possible changes in the regulations in the near future, many people felt like SHM systems will never be allowed without conventional inspections to validate the performance of the system. Moreover, next to the performance of the SHM system, another point of difficulty was found to be the reliability of the SHM system itself. False-positive an false-negative outcomes of a system were feared as they can jeopardise the high safety standards or result in unnecessary financial losses due to unnecessary ground times.

In addition to the obstacles mentioned above, MROs also face the fact that they do not have full access to the design information of structural components. This delimits the possible SHM systems than can be applied by the MRO itself as well as the obtainable accuracy and precision of the system in case OEMs are not involved into the implementation process.

In summary, the implementation of SHM systems still faces many physical as well as economic challenges. Besides, letting go of the IBM philosophy and make use of new technologies to perform inspections, it means that people have to gain trust in the systems as well. When designing a new SHM system it is therefore important to investigate how this technology might be best introduced to the commercial aviation industry and for this research in particular, how it is best introduced into the MRO industry. This is covered in the final part of this chapter.

1.3.3. Outlook for SHM at MROs

From the previous subsection could be concluded that there are two main requirements for a successful implementation of SHM. Firstly, when researching SHM, the benefit must be clear to the operator and secondly, the SHM system should create trust in the technology. This is why a case-by-case process is advised by for example Delta Airlines, Airbus and Boeing [5, 13, 15]. In this way confidence in SHM can be established while also generating more insight into its functioning and limitations.

A case-by-case process was also put forward by Boller and Kapoor [16, 17]. They found that under current circumstances, only little financial benefit is feasible. A minimal benefit was found after replacing all structural inspections of a D-check by an SHM system. It showed that a higher financial impact can be created, when applying SHM to drop-out items. Drop-out items are structural inspections that follow from unexpected damage situations, like impact or hard landings and result in additional inspections not matching the conventional maintenance programs.

Recently, *ARP 6461, Guidelines for Implementation of Structural Health Monitoring on Fixed Wing Aircraft by SAE International* was issued to provide a common framework for the implementation of SHM [4]. Its audience being not only operators, but also OEMs, regulatory guidances, students etc. The document has several purposes. It primarily provides the main definitions surrounding SHM and distinguishes the different types of operational monitoring and damage detection, e.g. scheduled versus automated monitoring. It also identifies the main functions of SHM and explains how SHM can be certified into current maintenance practices.

Although the document provides many details regarding an SHM system, it does not cover the process of selecting a structural component to apply the SHM system to. Neither does it provide guidance towards the selection of an SHM system. In the author's point of view, these are two subjects that operators and MROs still need additional guidance with. The involved parties really have to work together. While MROs might point out the suitable locations for SHM, OEMs are needed to provide the necessary design information, such as the material or loading types of safety critical structures. Moreover, MROs, will currently not have a full understanding of all available sensors systems.

Overall, the author agrees with the approach to introduce SHM using a case-by-case process. The first SHM solutions applied to aircraft should aim at showing potential and building confidence from which financial benefits can be shown in the long-term. The system should be applied to structures on which damage is expected, which could be from fatigue, but also from unanticipated events such as impact. This is sometimes also called hot spot monitoring. The inspections that follow from those occurrences will have a larger impact on the maintenance program than conventional inspections will have.

While a number of papers have compared the future of SHM to the working of a human nervous system fully operating on its own [5], it is questionable if SHM will be used to take over all structural inspections in future aircraft. In the author's opinion, it should be better seen as an addition to the conventional inspection techniques. When SHM is used for long-term monitoring, the author expects to see long-term benefits because maintenance can be adjusted to the individual aircraft. There is potential in the operational monitoring of aircraft when maintenance can be adjusted to the individual behaviour of components to increase

the reliability. Reducing inspection time is also very well possible for SHM systems as long as MROs are able to identify the impact on the total maintenance program. Analysing impact is assumed to be easier for SHM system used for rapid screening after unanticipated events or for additional inspections after for example a repair than it will be for conventional inspections fully integrated into the aircraft maintenance program.

The downside of this approach, however, is that SHM systems used for rapid screening after impact only show a return-of-investment in the case of an impact event.

For the reasons mentioned above, it was decided to focus on SHM systems for damage monitoring of drop-out items in the remainder of this thesis. It was decided to focus on damage monitoring instead of operational monitoring as the MRO is already more familiar with the latter due to Aircraft Health Management (AHM) already being applied to several systems. Damage monitoring can provide the MRO with more insight into composite behaviour and damage progression. It should be mentioned that this decision does not imply that operational monitoring for aircraft structures is of less importance to the implementation of SHM. In fact, operational monitoring will be required to provide operators the input data needed to determine the final RUL of a structure in order to let a IBM strategy evolve into a more CBM strategy.

2

SHM for Aircraft Composite Structures

From the previous chapter could be concluded that MROs are still fairly unfamiliar with the topic and potentials of SHM. It also became clear that from a business perspective familiarization with SHM would yield the best results through a case-by-case introduction, preferably using a drop-out item. For this research it was therefore decided to focus on an SHM system for a specific type of damage and material. After reviewing literature and having conversations with several structural & NDT engineers, the management of the NDT department and aircraft mechanics it was decided to focus on monitoring impact damage of composite structures.

In Section 2.1, the motivation behind SHM for composite structures and especially impact damage is further explained. Section 2.2 discusses impact damage of composites in general after which SHM techniques to monitor impact damage are presented in Section 2.3. The last section, Section 2.4, provides an introduction to guided waves, upon which the SHM system analysed in the next chapters is based.

2.1. Motivation for SHM of composites

Several motivations for SHM implementation were already presented in Section 1.2. This section further explains the motivation behind SHM for composite structures. To engineers, composites materials are the opportunity to design structures having unique properties. Composites are strong competitors to metallic structures due to their high specific strength and stiffness, high resistance to corrosion and temperature as well as their possibility to create complex shapes. This has resulted in a widespread introduction of composite structures in the aerospace industry with the aim to reduce fuel costs by increasing the structural effectiveness [18]. Using composite materials in aircraft structures can lead to potential weight reductions between 20%-50% [2].

An increase in the use of composites can be supported by reviewing the composite percentage by weight of aircraft over the last years. For example, the Boeing 777, first flown in 1994, consisted only of 12% composite by weight, while the Airbus A380, released in 2005 already showed about 22% composite by weight. Newer aircraft, like the Boeing 787 introduced in 2009 and A350 first flown in 2015 show a 50% and 52% composite by weight composition [19]. Despite of this significant increase, the question might still rise to what extend there is a need to monitor composite structures. In the author's opinion there are two main reasons for this.

Firstly, compared to metallic structures there is little knowledge about composite damage behaviour. This can be explained by the fact that there is little historical (damage) data to learn from. Environmental conditions and operational loads cause composite structures to suffer from fatigue which, similar to metallic structures, is a progressive phenomenon. While a lot of historic data already exists for metallic structures, the research community still relies on an assumed similitude between testing and operational conditions for composite structures. An SHM system which can monitor the growth of damage might provide more insight into composite damage behaviour [20]. This insight can also be used to complement and improve the physical models which are used to predict damage propagation. Eventually, a better understanding, allows for an improvement of future composite designs and to use composites to their full potential, while also improving maintenance activities.

Secondly, composite aircraft structures are vulnerable to random impact damage. Impact can cause extensive damage in the form of delaminations and intralaminar cracks beneath the surface of the structure

and can be hard to detect visually from the outside. This type of damage was previously introduced as BVID and requires NDT inspections to be detected. While a metallic and composite fuselage skin will look the same from the outside, impact damage to metallic structures will be visible, while damage to composite structures might be invisible from the outside. Operators and MROs fear that ground personnel overlooks BVID or forgets to report impact events so that additional inspections are not triggered in time. Hence, the operator will and cannot be aware of the internal damage possibly caused to the structure. The principles of BVID will be explained further in the next section, Section 2.2.

Impact damage is the most encountered in-service damage for composite aircraft. Research at Lufthansa Technik from 2006 concluded that three out of four structural damage events of aircraft composite structures are caused by mechanical impact for example by collisions during ground operations. It was found that narrow-body aircraft suffer structural damage nearly every 4600 flights, while wide-body aircraft suffer damage every 1000 flights. The need of SHM is extra supported when considering the fact nearly 80% of the performed inspections are visual inspections [21]. Moreover, research in Australia showed that out of the 398 impact occurrences reported in the years 1998 to 2008, only 25% of these events resulted in damage. However, additional inspections had been triggered after every event. This means that for 298 of these events the aircraft was unnecessary grounded and possibly delayed [22]. An SHM system could be used to prevent this in the future. Most impact occurrences were reported close the Door Surrounding Structures (DSS) resulting from ground operations. An overview of ground operations which can cause impact damage is shown in Figure 2.1.

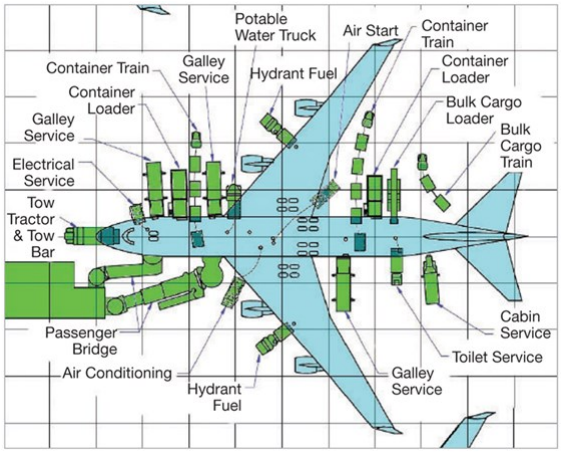

Figure 2.1: Typical ground handling operations of a commercial aircraft [23].

For most of the reported impact occurrences, inspections require multiple NDT techniques, making it a costly and time-consuming business in need of highly skilled mechanics [19]. This is due to the fact that composite damage can exists out of a combination of damage mechanisms, however no NDT technique is solely capable of detecting all the sorts of damage mechanisms existing in composite structures. Naturally, this poses challenges to MROs servicing composite aircraft like the Boeing 787 and Airbus A350 as BVID inspections must take place internally as well. This is especially difficult for stiffened panels in for example the wings or fuselage. These structures can carry high compressive loads and are therefore equipped with hat stiffeners. This does not allow for visual inspections of the 'internal' skin covered by the stiffeners and so lead to very expensive maintenance operations [24]. An SHM system capable of assessing internal BVID and especially its severity will increase the speed of diagnosis and therefore decrease ground time. This is also supported by a recent survey among MROs, operators, OEMs and regulators which stated that the commercial aircraft industry places composite materials on the top of the demand list for SHM technologies. The three main damage types to inspect being cracks, delaminations and disbonds [25].

To conclude, SHM for impact damage for an MRO offers a quicker and therefore cheaper damage diagnosis and lowers the fear of overseeing BVID. More benefits were seen by the KLM E&M in postponing repairs in the case an SHM system can be used to assess damage severity as well. This will allow operators to show OEMs and regulators that they are continuously in control of assessing damage severity and therefore its growth. Potentially, this leads to the extension of maintenance intervals and a decrease in additional inspections or immediate repairs when allowing the operator to repair during scheduled overhaul instead.

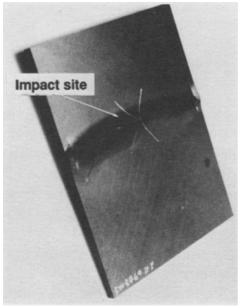

(a) Post-impact compressive failure.

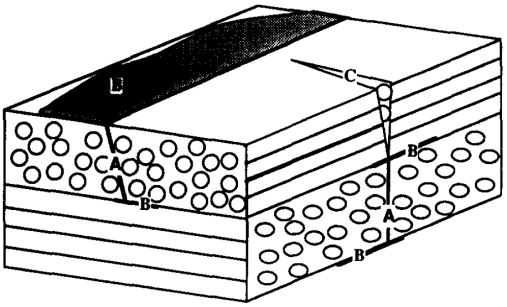

(b) Basic damage mechanisms in composites. A. Intralaminar cracking; B. Delamination; C. Fiber breakage.

Figure 2.2: Damage of composite structures [27].

2.2. BVID of composite structures

The beginning of the previous section states that composite materials exhibit superior behaviour over metals in several areas. However, they also show a number of limitations of which one of the most prominent and well-known problems is their susceptibility to BVID from LVI. BVID resulting was shortly introduced before and will be explained further in this section.

Typically, two types of composite structures are found in aircraft; monolithic composites and sandwich composite structures. The previous paragraphs showed that especially the fuselage is susceptible to LVI as a result of ground operations. The fuselage skin of a Boeing 787 is built up out of a quasi-isotropic monolithic CFRP. For this reason, the focus in this section lies on BVID of monolithic composite structures to which Boeing has referred as *"Small damages which may not be found during heavy maintenance general visual inspections using typical lighting conditions from a distance of five (5) feet*" [26].

Over the years, much research on composite behaviour after impact has been conducted. Studies have showed that low-velocity impact generally causes a severe strength degradation in compression which can results in sub-laminate buckling and post-buckling delamination growth. The risks of impact damage are also acknowledged by Boeing as the SRM of the Boeing 787 dictates that the effects of impact result in micro-cracks which can grow into interlaminar layers during loading and even result in catastrophic early failure of the part. This is because, when loaded in compression, delamination or interlaminar cracks can cause buckling which in its term cause a redistribution of loads inside the structure resulting in failure [26].

An example of compressive failure after impact is shown in Figure 2.2a. From a material point of view, impact damage has caused a change in the material composition, e.g. through fiber breakage. But changes to material or laminate composition also affect the overall structural properties of the component, e.g. its compressive strength. This behaviour is often quantified using the Compressive Strength After Impact (CSAI) [27].

According the SRM, composite structural components should be periodically inspected to assess deterioration. Besides, an inspection might also be triggered by a reported impact occurrence, a prescribed additional inspection as a result of an earlier damage event or be advised by an SB or AD. A flowchart describing the inspection process of a composite structure based on the B787 SRM is shown in Appendix A and shortly discussed below.

For all components first a close visual inspection is performed during which indications of impact, lightning, heat damage or moisture ingestion are evaluated. In case indications of impact are identified, an estimation of the damage type and size are made using a visual inspection. These are subsequently compared to the Allowable Damage Limits (ADL) from the SRM. If damage is in accordance with the ADL, no other flight restrictions are valid. If damage is found to be larger than the ADL or the size and type cannot be provided with enough certainty from the visual inspection alone, subsequent NDT inspections are performed. Following, the size and type are compared to the ADL once more and, in case the damage size does exceeds the ADL, compared to the Repair Damage Limits (RDL). In case damage is within RDL, either a category A: a permanent repair, a category B:permanent repair with additional inspections or category C: temporary repair, followed by a category A or B repair can be performed. When damage exceeds the RDL, a damage assessment is to be performed by the OEM which decides for a repair based on approval by the OEM or for a replacement of the damaged parts. Under current regulations an SHM system should therefore detect impact and identify the damage size and type before exceedance of the ADL, making it possible to optimize maintenance scheduling

for a repair or replacement.

But what damage mechanisms should the SHM system be expected to find? Literature concludes that the predominant damage mechanisms in BVID are intralaminar cracking, fiber cracking and delaminations as shown in Figure 2.2b. These are the building blocks of a subsequent network of damage mechanisms, which are difficult to identify or separate from each other because they interact [28]. How they interact depends on the lay-up, geometry and material. From experiments performed in the past could be concluded that delaminations in general do not occur between adjacent layers of the same ply orientation where interlaminar shear stress are low. It could also be seen that cracks are usually the starting point of delaminations and that the growth of delaminations depends on the location of cracks in thickness, proximity to free edges and regions of stress concentrations, like geometrical discontinuities such as bolt holes.

A general proposed model for BVID or impact damage can be seen in Figure 2.3a [29]. The model states that the opposite side of the impacted surface gets loaded in bending during impact. For high impact forces, matrix cracks and fiber breakages can occur on this side of the laminate. The impact energy spreads in a triangular shape through the laminate creating matrix cracks due to bending and interlaminar shear, which might turn into delaminations if the Delamination Threshold Load (DTL) is exceeded [30].

While the impact damage is not fully penetrating the panel, a conical zone can be identified at the impact location. Below the cone, fiber failure is visible away from the mid central line, and shear cracks are found away from the location of impact. This type of BVID was also made visible using X-ray testing in [28] and shows similar results which can be seen in Figure 2.3b.

The next section will present several SHM algorithms which can be used to monitor BVID.

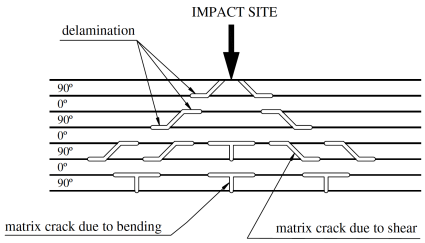

(a) Damage mechanisms after impact [29].

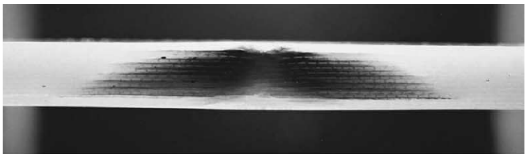

(b) X-ray of BVID [28].

Figure 2.3: BVID of composite structures.

2.3. SHM techniques for monitoring impact damage

In general, SHM systems used for damage monitoring can be divided into two categories; passive and active SHM systems. A passive SHM system uses continuous measurements from sensors and extracts damage characteristics from the measured data. Impact damage detection on composite structures using passive SHM is based on Acoustic Emission (AE) monitoring. AE waves are a type of transient elastic waves which follow from a sudden redistribution of stress in the material which might result from damage [31]. In case of active SHM, the structure is equipped with both sensors and actuators. For aerospace structures, this often means that an actuator excites guided waves which are detected by a sensor. By analysing the response of AE waves after an impact event, or by comparing guided waves signals from damage and undamaged states, researchers aim to fulfil the five SHM levels mentioned in Section 1.1. The principles of guided waves are further explained in Section 2.4. This section first presents two typical sensors used for SHM. Hereafter, several passive and active SHM systems are presented.

2.3.1. Typical SHM sensors

Most passive and active SHM systems discussed in literature use either PZT sensors or Fiber Bragg Gratings (FBGs). A drawing of a PZT sensor is shown in Figure 5.3a. PZT sensors make use of materials which feature the piezoelectric effect. This means that they are able to convert mechanical energy into electrical energy and vice versa. Hence, when a PZT sensor is strained, it excites a voltage. Using this principle, accelerations or vibrations following from an AE event or an excited ultrasonic wave can be captured [32]. The piezoelectric effect makes PZT sensors able to function both as actuators and as receivers. Other advantages of using PZT sensors are their low costs, their linear response and availability in a large frequency range. On the other hand, the sensitivity of PZT sensors is quickly affected by changes in temperature and easily influenced by

electromagnetic interference, resulting in noise. Lastly, the PZT's material degrades over time which can cause a frequency change or phase shift in their measurements. This means that in order for a SHM system using PZT sensors to be certified, long-term and thus costly tests have to be performed to prove the durability of the system.

FBGs are a type of optical fibers which can be used to detect AE waves as well as guided waves. When a beam of light travels through the FBG, the FBG functions as a filter. Most of the light passes through the fiber, however a portion of the light is reflected, this is shown in Figure 2.4b. During the manufacturing of the FBG, it is exposed to a pattern of ultraviolet light. This causes a local increase in the refractive index of the fiber. As a result some wavelengths are reflected so that strains caused by AE or guided waves can be measured. Compared to PZT sensors, FBGs are quite expensive and sensitive to the environment, breakages and show a directional sensitivity. This means that their response depends on the direction in which they are strained. However, they are immune to electromagnetic interference and their multiplexing capabilities enable the system to cover large inspection areas using only a limited number of fiber lines [30].

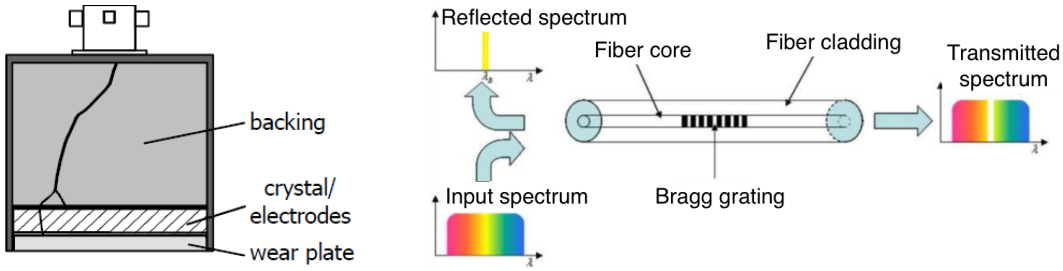

(a) Piezoelectric sensor [32]. (b) Fiber bragg grating [33].

Figure 2.4: Typical SHM sensors.

2.3.2. Passive SHM systems

Literature regarding passive SHM systems for BVID detection and localisation are mostly based on triangulation. Triangulation makes use of at least three sensors to capture AE waves resulting from impact in order to find its location. The impact location is found by comparing the Time of Arrival (ToA) of the different waves. For metallic structures this method works well because the wave velocity is the same in all directions due to the material's isotropic properties. This is more complex for composite structures because both AE waves and guided waves are influenced by the anisotropic properties of the individual plies, the different fiber orientations and the dispersive nature of the guided waves. As an example, AE waves will travel faster along plies for which the fiber orientation is the same as the direction of wave propagation. This is because ultrasonic waves travel faster through materials with a higher Young's modulus [34]. Hence, passive methods based on classical triangulation techniques are not favourable for composite structures when constant phase velocities must be assumed throughout the structure.

To overcome this problem, several articles have proposed an SHM system based on adjusted triangulation techniques which use optimisation schemes to solve for unknown variables, such as the phase velocity, ToA or the impact location on composite structures. Coverley and Staszewski have proposed to determine the wave velocity experimentally using the zero-crossing method by Draudvilienė and Mažeika [35, 36]. Hereafter, the impact location is found using a Genetic Algorithm, which is a search procedure based on natural genetics.

Ciampa and Meo estimated the ToA using the squared modulus of the continuous wavelet transform after which an iterative Newton method was used to solve a non-linear set of equations to find the phase velocity and location of impact [37]. This method was further improved and used for FBGs by Sai et al., who added an a Particle Swarm Optimisation algorithm to provide a better initial guess for the Newton method [38].

Lastly, FBGs were compared to PZT sensors by Kirkby et al. when determining the impact location based on triangulation by minimising an error function [39]. They also showed that PZT sensors led to more accurate results than FBGs, due to the directional sensitivity of FBGs.

Another way to cope with the anisotropy of composite materials is by using a database containing multiple reference signals. While comparing a normalized reference signal from a healthy structure to a current state response signal, Shrestha et al. proposed an impact localization technique based on an error outlier algorithm [40]. The idea behind this method is that when calculating the error between two signals, dissimilar signals will show larger error peak values than similar signals. This allows damage to be detected.

A reference database containing both signals from healthy and damaged structures was used by Lu et al. [41]. The database was used as an input for a Support Vector Machine algorithm to solve for different health states. These health states were formerly determined using a Principal Component Analysis.

Frieden et al. proposed a passive SHM system for impact localisation based on interpolation of a reference data set [42].

While the methods above show to have potential for accurate localization and also a severity estimation of BVID, a large disadvantage for an MRO would be the establishment of a database while having limited access to design information or spare parts. Moreover, a passive system does not allow for repeatable measurements, which is difficult when trust in the system still needs to be gained. Finally, the passive system must be able to record impact during operating conditions, or a noisy environment during ground operations. The environment for an inspection by an active system can be much better controlled.

2.3.3. Active SHM systems

When reviewing literature about the localisation of BVID using an active SHM system, a variety of articles proposed an image reconstruction technique. Using a conventional NDT technique based on ultrasonic waves, inspection results are often presented in the form of a C-scan. Reconstruction techniques aim to provide similar images. The first image reconstruction technique was proposed by Zhao et al. and is called RAPID, Reconstruction Algorithm for Probabilistic Inspection of Defects [43]. The outcome is supposed to be a probability distribution, showing the probability of damage at every point on the inspected area. The idea behind RAPID is that signals obtained from guided waves travelling through damage have different wave forms compared to signals obtained from the healthy structure. These healthy signals are called baseline signals and while comparing a particular current state signal to its baseline signal using a Damage Index (DI), damage such as cracks, corrosion and delaminations can be detected.

Using a probabilistic method, the damage locations have also been estimated. While Zhao et al. compare signals based on the correlation coefficient, Wang et al. have tried to improve RAPID using a DI based on Shannon entropy and De Fenza et al. based it on changes in signal amplitude [43–45]. Hettler et al. tried to remove the baseline signal from the image reconstruction techniques by arguing that damage affects signals with different amplitudes in different ways [46].

Damage severity or the damage size was also analysed by several researchers. Cross-correlation, or the maximum time-shift was used by Petculescu, Krishnaswamy and Achenbach to find a relationship between the maximum time-shift and damage severity [47] . Closely related to this research is the article by Trendafilova, Palazzetti and Zucchelli who made a comparison between a DI based on cross-correlation and Mutual Information (MI) to monitor damage growth [48]. While cross-correlation provides only a measure of linear similarity as a function of the displacement of one signal compared to the other, MI determines the total amount of mutual dependence or similar information between two signals. While both DIs could be used to detect damage, it was shown that MI was much better at capturing damage growth than using cross-correlation. Lastly, Polimeno and Meo based their damage detection method on non-linearities introduced by damage. It was for example shown that the resonance frequency of composite laminates shift for an increase in non-linear behaviour using single-mode non-linear resonance acoustic spectroscopy [49].

Overall, it was found that damage identification using active SHM through the excitation of guided waves features several advantages. Firstly, such a technique is able to cover large inspection areas with a low energy consumption. Secondly, there is no need to take away any coating or insulation and the material can be inspected through the entire thickness. The inspection can be repeated multiple times and performed according to a fixed schedule if necessary.

It was then decided to focus on investigating an image reconstruction algorithm using PZT sensors for the monitoring of impact. PZT sensors were chosen, because there were found to be better at locating damage on larger inspection areas. For an MRO this is an important requirement. It was also found that the output of FBG sensors is more difficult to process and most techniques made using of a reference database, which is undesirable for a retrofitted SHM solution. It also means that a lot of installation time is required.

From the perspective of an MRO, image reconstruction algorithms show a high potential because it allows for rapid screening of the structure with the possibility to quickly show the location of damage. they moreover show potential for growth monitoring. Besides, its output can be compared to a C-scan image which will appeal to the industry. Finally, the algorithm does not require the material properties to be known, so that it still offers the potential to give reasonably accurate results without the need of technical details from the OEM and a dense sensor network. Because an active SHM system based on image reconstruction makes use of guided waves, the remainder of this chapter focusses on introducing guided waves.

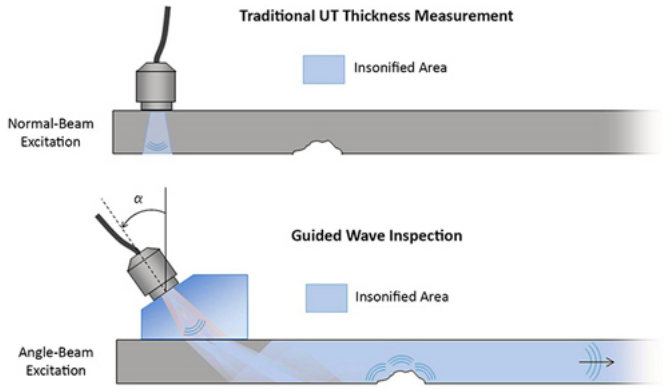

Figure 2.5: Difference between UT and GW testing [50].

2.4. Introduction to guided waves

Conventional Ultrasonic Testing (UT) is a common method of NDT, which has been widely applied in the aerospace industry for over many years. UT makes use of the controlled excitation of ultra-high frequency acoustic waves, which are inaudible to the human ear [2]. In a way, ultrasonic waves are comparable to light waves of which the interaction with a material changes with the material's properties. When the acoustic wave encounters a material with a deviating acoustic impedance, part of the signal is reflected. Therefore, while defects inside a structure will show a different impedance from its surroundings, damage can be detected inside a structure by analysing either the reflected or transmitted signal. In UT testing, pulse-echo configuration are use to analysed the former, while the latter is analysed in a pitch-and-catch configuration. The main advantages of UT are the penetrating powers of the waves, so that the structure can be inspected subsurface, and the ability to measure the location and geometry of the defect to a high accuracy.

This section presents an introduction to guided waves. The difference between conventional UT and guided wave testing is shown in Figure 2.5. Guided waves are ultrasonic waves which travel in plate-like structures such as panels or pipes. During guided wave testing, guided waves are excited to interrogate the structure in a controlled manner. These waves are widely using in NDT because of their ability to travel over large (curved) distances with little energy loss. This makes them especially suitable for aerospace structures and applicable to SHM because they enable monitoring of large areas using only a few sensors. This section will start discussing guided waves in general in subsection 2.4.1. Hereafter, the interaction between guided waves and impact damage is discussed in subsection 2.4.2.

2.4.1. Guided waves characteristics

Ultrasonic waves occur in different wave modes. These wave modes are depending on the vibrational behaviour of particles inside the structure and move together to form a mechanical wave. Inside a solid, these particles causes waves to propagate as longitudinal, shear or surface waves. These type of waves were first researched by Lord Rayleigh in 1885 [51], who investigated wave propagation at a solid's free surface. These waves were later on called surface or Rayleigh waves. They travel near the surface of a solid and include both longitudinal as well a transverse motions which decrease in amplitude as the distance from the surface increases. This is shown in Figure 2.6.

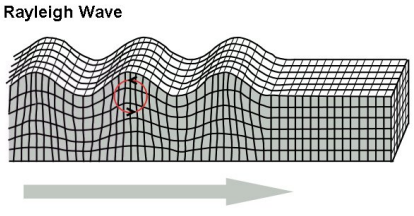

Figure 2.6: Schematic representation of a surface or Rayleigh wave [52].

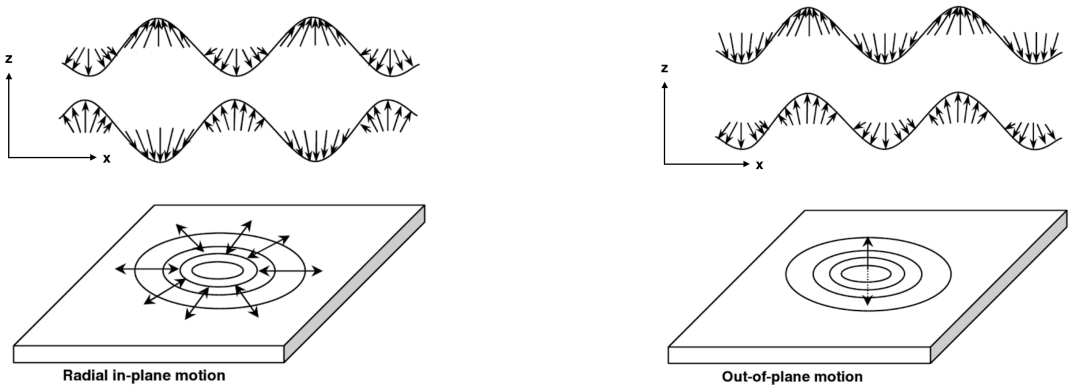

(a) Fundamental symmetric Lamb wave $S0$.

(b) Fundamental anti-symmetric Lamb wave $A0$.

Figure 2.7: Fundamental Lamb waves and the direction of plate motion due to both modes [53].

After the discovery of surface waves, Loves & Lamb analysed waves in plates. They found that waves in plates are bounded by the plate's surface causing the wavefront to travel parallel to the plate's thickness. These waves can be divided into two types; Shear-horizontal (SH) waves and guided waves. Guided waves, also called Lamb waves, propagate parallel to a plate's surface as though confined inside.

Lamb waves are characterized by a particle motion that is similar to Rayleigh waves. But contrary to these surface waves, Lamb waves are plate waves which penetrate through the full thickness of the plate. The two most common Lamb wave categories are; symmetric and anti-symmetric Lamb waves. For both types several modes may exists, $S0, S1, S2, ...Sm$ and $A0, A1, A2, ...An$ respectively. The fundamental symmetric $S0$ and fundamental anti-symmetric $A0$ define the first modes. In both types particles move in the x- and z-direction, i.e. the direction of wave propagation and the normal direction with respect to the plate. The $S0$ and $A0$ modes and their plane motion are shown in Figure 2.7. By definition Lamb waves do not show movement in the y-direction. Movement in the y-direction or in the horizontal plane is described by SH waves.

An important wave characteristic to take into account during guided wave testing is the dispersive behaviour of Lamb waves. For a given frequency-thickness product, $f \cdot d$, of certain structure, a variety of symmetric and anti-symmetric Lamb wave modes may exist. In theory, given a plate's finite thickness, an infinite number or symmetric and anti-symmetric modes can be found by solving the Rayleigh equations [53]. The velocity of each mode depends on the frequency-thickness product. This behaviour can be represented using a dispersion curve, of which an example is shown in Figure 2.8a.

The dispersion curves shown in this figure belong to a $1.6mm$ thick 6061 aluminium plate [54]. The y-axis shows the group velocity of the wave, which defines the speed at which the wave front travels and can be derived from the phase velocity, which is the speed at which individual frequency components of the wave travel. It can be seen from Figure 2.8a that for higher values of f_c more than one mode can exist simultaneously.

Figure 2.8b shows the response waveform, for the same panel, to an excited 4 cycle sine-wave toneburst centered at $f_c = 200kHz$. From Figure 2.8a can be seen that for this particular f_c, only the first two fundamental modes exist. These can also be seen in the response signal together with reflections from the plates boundaries. Table 2.1 shows the different modes and group velocities, together with the travelled distances before reaching the receiving sensor. Clarifying, the fundamental $S0$ modes travels at a group velocity of $5.35km/s$ according to Figure 2.8a. The distance between the sensors amounts to $30.48cm$ and the distance from the exciting sensor to the back edge amounts to $60.96cm$. Therefore, the $S0$ should be received by the sensor the first time after having travelled $30.48cm$ at a velocity of $5.35km/s$ around 57.0 seconds, which is clearly visible when looking at the response signal in Figure 2.8b. The same holds for $A0$. However, when taking a look at the reflected signal from the back edge, it can be seen that the $S0$ mode should be visible at $170.9s$ but $A0$ reflected from the back is not visible on this response signal. This also means that the first wave packet designated as boundary reflected consists either out of the reflected $S0$, $A0$ or a build up of the two modes reflected from the side edges of the panel. What should be taken away from this example is that identifying different modes, seems rather simple, but quickly becomes complicated on complex geometries as modes might overlap. Overlapping of modes is likely to increase when more wave modes occur. As a

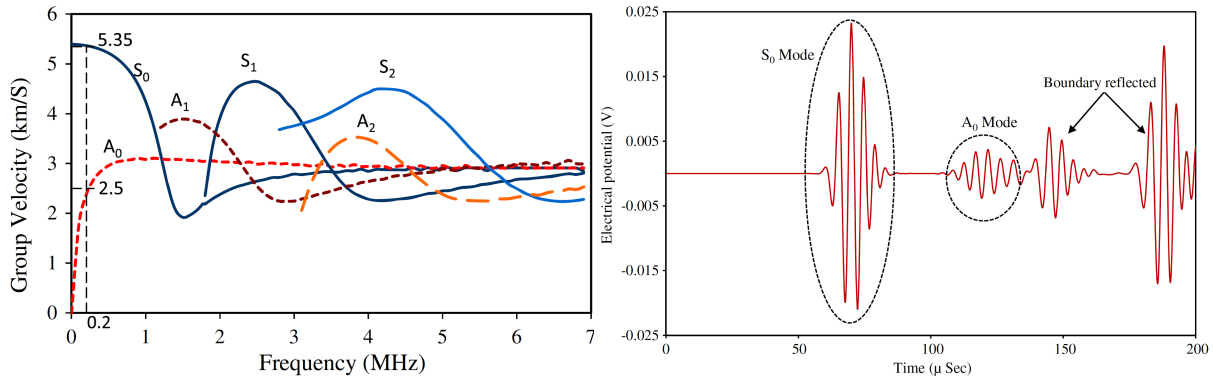

(a) Dispersion curve for the group velocity. (b) Response signal.

Figure 2.8: Simulated Lamb wave in a 1.6 mm 6061 aluminum plate [54].

Table 2.1: Signal information corresponding to Figure 2.8.

Mode	Group velocity [km/s]	Distance travelled [cm]	Time [μs]
S0	5.35	30.48	57.0
A0	2.5	30.48	121.9
S0 reflected from back edge	5.35	91.44	170.9
A0 reflected from back edge	2.5	91.44	365.8

consequence, guided wave testing is often performed in the lower frequency range, $f_c \leq 1MHz$. So that the fundamental modes are the only modes existing over the entire frequency range and allow to keep the signal analysis during the inspection simple.

From the previous paragraph became clear that separation of Lamb wave modes in a response signal is rather complicated. However, there are two more features increasing the complexity of Lamb waves; dispersion and attenuation. During a guided wave inspection, a wave packet needs to be generated. Using a frequency carrier wave, a transient tone burst can be generated. A common window function used for wave generation is the Hanning window [55]. The modulation generates a narrow frequency band with the central frequency being the chosen excitation frequency, f_c. However, in reality it consists out of a multitude of frequencies centered around f_c. From the dispersion curve could be seen, that for a given thickness, a change in frequency causes a change in wave velocity. Therefore, parts of the wave travel at different velocities. This is what causes wave dispersion and is shown in Figure 2.9b. It becomes more severe with increase in distance. Moreover, the steeper the dispersion curve, the more dispersive the wave mode will be. This is because the difference in velocity over a the range of frequencies will be greater.

Besides dispersion, guided waves also suffer from attenuation as the energy of guided waves will dissipate with distance. The effects of wave attenuation is shown in Figure 2.9a. It manifests itself as a gradual reduction of the wave magnitude. Besides an increase in distance, damage and geometric discontinuities will increase energy dissipation due to scattering and mode conversion. Of course it also increases with frequency, because as the wavelength decreases particles will interfere more with the material. It should be noted that attenuation differs from dispersion discussed in the previous paragraph as the latter refers to changes in the wave velocity while the former refers to wave magnitude.

2.4.2. Guided waves for SHM

SHM based on guided waves tries to define the health of a structure by extracting damage features from the signal or compare signals from the pristine state to its current condition. When reviewing SHM using Lamb waves, different arguments are provided when selecting modes for inspection. Most research has focussed on using the fundamental $S0$ mode. This has several reasons. Firstly, the $S0$ mode generally suffers from less attenuation than the $A0$ mode. This can be attributed to the dominant out-of-plane displacement of the particles in the anti-symmetric modes, which causes the wave to lose parts of the energy to its surroundings, while the particles of symmetric modes mostly show in-plane motions and therefore keep energy confined

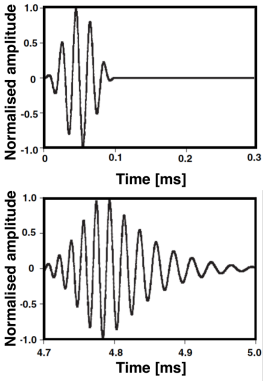

(a) Upper: excited signal, lower: dispersion of received signal.

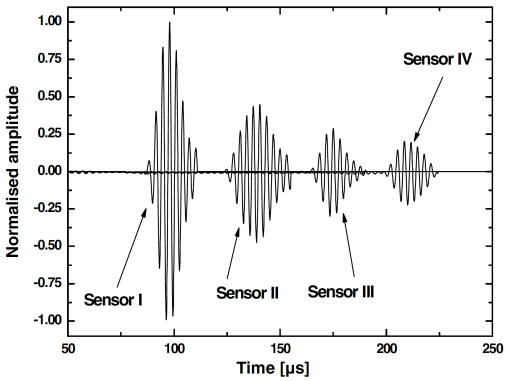

(b) Wave attenuation.

Figure 2.9: Lamb wave attenuation and dispersion over time [53].

inside the plate. Moreover, the $S0$ mode show less dispersion in the low frequency range and has a higher velocity, so that it is easier to avoid complex wave reflections from the structure's boundaries. On the other hand, choosing the $A0$ mode might give advantages in terms of an easier activation and has a smaller wavelength for the same excitation frequency, thereby decreasing detectable damage size. Finally, the $A0$ mode usually shows larger amplitudes when the two modes are excited simultaneously[53].

If a specific mode is to be excited, mode selection can be achieved by placing the exciting sensors in different positions and exciting them either in- or out-of-phase. When a wedge is used, mode selection can be realised by placing the wedge on one side of the plate only. However, when using disc sensors, a sensor is required on either side of the plate to select the prescribed mode [53]. From a practical point of view, it will not always be possible to attach sensors to both sides of a structure.

When Lamb waves interact with damage, their properties such as energy, amplitude or mode might be affected. This is the key assumption for damage detection using Lamb waves. Based on their change in behaviour, damage features can be extracted. As a result of impact, the main damage mechanisms found inside a structure are intralaminar cracks and interlaminar cracks or delaminations. These cause a local abrupt change in material properties and could therefore also be regarded as a discontinuity along the wave's propagation path. Once the wave interacts with the damage area, it tends to reflect and refract. This means that on one hand, the same mode can be reflected or scattered causing a decrease in the transmitted signal energy. It can also cause a mode conversion to take place, i.e. at low frequencies, $S0$ mode conversion to $A0$ mode might occur [56].

In general, it can be concluded that damage causes a decrease in signal energy due to scattering and mode conversion [53]. Mode conversion from $A0$ to $S0$ is less expected because of the higher velocity of the $S0$ mode. Due to the different behaviour of the modes, it also makes them sensitive to different types of damage. Taking a look at the particle motion inside Lamb waves also gives information about the interaction. The $S0$ shows dominant particle behaviour in the direction of wave propagation, therefore, through thickness cracks in the normal direction are expected to affect the $S0$ more than the $A0$ mode. Similarly due to the particle motion, delaminations will more likely be easier to detect by analysing the $A0$ mode. Moreover, when using a pulse-echo configuration, the $S0$ is favoured because it shows more reflection that the $A0$ mode. [2] [57].

Overall, it was concluded from literature that no straight forward scenario exists for guided wave interaction with damage. While damage types, location and size will have an influence on the interaction, it also relies heavily on the wave's mode, shape, number of cycles, and central frequency as this determines the other modes that might travel through the structure. It is because of these reasons that most active SHM strategies using guided waves focus on a comparison between baseline and damaged state signals.

3

Image Reconstruction Algorithm: Methodology

The purpose of this research is to investigate an algorithm which is able to capture and monitor impact damage on composite plates in a similar manner as a C-scan inspection. The focus lies on constructing an image reconstruction algorithm which is able to detect, locate and quantify damage. In order to make this SHM system applicable to the MRO industry it was decided to create an algorithm which does not require the material specifications for its damage diagnosis. This chapter presents the methodology behind the Image Reconstruction Algorithm (IMRA). IMRA compares damaged state signals to baseline signals and reconstructs an image showing the location(s) on the inspected area which have the highest probability of damage. In other words, the reconstructed image shows the location(s) on the inspected area with the highest probability to have caused the measured change between a damaged and undamaged structure.

This chapter starts by providing a general overview of the algorithm in Section 3.1. The second section describes which part of the signal has been used for damage feature extraction. Section 3.3, describes the usage of a DI which is used to quantify the change between signals resulting from damaged and undamaged states. Hereafter, the functioning of the Pixel Influence Weight (PIW) is explained in Section 3.4. Following, the image reconstruction process using Data Fusion (DF) is explained in Section 3.5. Finally, a definition of damage is provided in Section 3.6, so that four possible methods for the application of a threshold can be presented in Section 3.7.

3.1. General image reconstruction algorithm

Section 2.4 briefly introduced active SHM methods using guided waves. Two active SHM configurations were mentioned; a pulse-echo configuration and a pitch-and-catch configuration. The algorithm presented in this chapter is based on a pitch-and-catch configuration. It requires a diagnostic Lamb wave signal, excited by an actuator, to travel through the area to be inspected and to be captured by a receiving sensor.

To reconstruct an image, a network of sensors is attached to the structure creating a number of sensing paths between the actuator and receivers. It is assumed that Lamb waves travelling through a damaged structure will be different from the corresponding response signals of an undamaged structure. A DI is calculated which evaluates the difference between a signal before and after the presence of damage. This DI or change in signals is then used to describe a physical change to the structure. Depending on the number of sensors more than one DI is calculated. These values can be combined to reconstruct an image.

The algorithm has been programmed in *Python*. A basic flow chart of the algorithm is shown in Figure 3.1 and a more extensive flow chart of the code's structure is shown in Appendix B. The algorithm's basis lies with RAPID, which was used for damage detection on an aluminium wing specimen [43]. An advantage of this algorithm is that it uses the information of multiple actuator-receiver paths combined which increases the reliability of the system with respect to a single path.

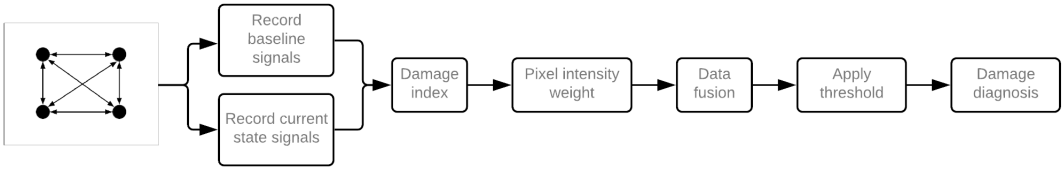

Figure 3.1: Flowchart for the image reconstruction algorithm.

1. For each sensing path, i.e. actuator-receiver combination, the baseline and damaged or current state signals are to be recorded. Each PZT sensor takes turn in functioning as an actuator, while all other sensors act as a receiver.
2. Damage features are to be extracted from the Lamb wave signals using a DI to evaluate the difference between the baseline and damaged signals.
3. The inspection area is divided into a grid of pixels. Hereafter, a PIW is defined for every pixel on the grid. The PIW describes the assumed relation between damage at the location of that pixel and the effect it has had on the DI of a particular sensing path. This is repeated for all paths.
4. The next step involves combining the information taken from different sensing paths in order to create one image that shows what parts of the inspected area have caused the changes between the signals and could therefore be identified as damage.
5. The last step is the identification of a suitable threshold for damage detection, localisation and severity estimation.

The algorithm relies on a number of assumptions which are needed to detect as well as locate and estimate the size of the damage. They are stated below:

- Differences between signals following from damaged and undamaged structures can be fully attributed to damage. Hence, measurements are not influenced by operational or environmental conditions such as changes in temperature.
- Damage will cause the most significant signal change when positioned in the direct wave path. Therefore, the influence of damage to a specific sensing path decreases with an increase in distance.
- Damage growth leads to a larger difference between signals, thus leading to higher values of the DI.

3.2. Direct wave propagation: Initial signal processing

The first step of the image reconstruction algorithm is the calculation of the DI. However, it has been mentioned several times in literature that only the direct propagation path between two sensors should be taken into account when calculating the DI. This means that only the wave propagating on a straight line between two sensors should be taken into account and so reflections from geometric boundaries or possibly from damage should be excluded from the response signal [46, 58, 59]. A commonly applied method to achieve this is to window the response signal around the first arriving wave packages of one or both of the fundamental modes. This section proposes a method to isolate the first arriving wave package which is based on the method proposed by Hettler et al. [46].

Assuming the entire signal x, contains n_s samples and the excited signal contains n_c cycles, the estimated number of samples required to isolate the first arriving wave package is given by

$$n_r = \mid ToA \cdot f_s \mid + \frac{n_c}{2} \cdot \frac{f_s}{f_c} \quad [-], \tag{3.1}$$

where f_s is the sampling frequency, f_c the excited waveform frequency and ToA the time of arrival. In [46] the ToA was calculated using the following equation

$$ToA = \frac{s}{c_p(\theta)} \quad [s], \tag{3.2}$$

where $c_p(\theta)$ is the phase velocity of the selected wave mode that is being analysed in the direction of angle θ° and s being the distance between the two sensors. However, an MRO does not always have access to the dispersion curve of the laminate, neither do they have access to the lay-up so that it can be established

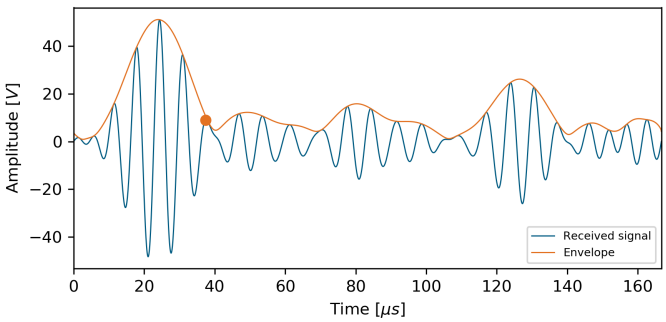

(a) Received signal and its envelope.

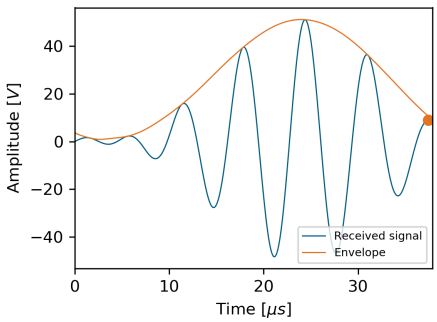

(b) Direct signal using Equation 3.1.

Figure 3.2: Response signal taken from [14].

theoretically. Another solution would be to determine the phase velocity experimentally, but this is costly and time-consuming. Therefore, the author proposes a different method using the signal envelope. The envelope is determined using the Hilbert Transform a defined by

$$x_A(t) = x(t) + 1x_H(t) \quad [V] \tag{3.3a}$$

$$x_H(t) = \frac{1}{\pi} \cdot \int_{-\infty}^{+\infty} x(\tau) \cdot \frac{1}{t-\tau} d\tau \quad [V] \tag{3.3b}$$

$$x_{env}(t) = \sqrt{x^2(t) + x_H^2(t)} \quad [V], \tag{3.3c}$$

here $x_A(t)$ is the analytical signal in the time domain, which consists out of $x(t)$ the real signal and its complex part, the Hilbert transform $x_H(t)$. Using the analytical signal, makes it possible to write the signal based on its amplitude and phase or frequency. Taking the absolute of the analytical signal, gives the envelope $env(t)$. The ToA is then defined as the arrival time of the first peak of the envelope. To illustrate the outcome of this approach, a response signal taken from the database discussed in the next chapter is shown in Figure 3.2a. An excitation signal with $f_c = 150kHz$, $n_c = 5$ and a sampling frequency of $f_s = 12$MHz was applied to the actuator. The envelope of the signal was calculated using the method above and the peak amplitude of the envelope was found to be $37.4V$ corresponding to a ToA of $24s$. This caused the signal to be cut after $n_r = 449$ samples or $t = 37.4s$ as shown in Figure 3.2b.

3.3. Damage Index: Extraction of damage features

The DI evaluates the change between two signals which is assumed to be caused by a physical change of the structure which is located somewhere in a predefined area between two sensors. Consider the eight-sensor network shown in Figure 3.3. A total of 32 sensing paths can be created when evaluating the wave propagating from left to right and vice versa. For each path a DI is determined which means that sensors take turns being the actuator while all others function as a receiver.

From Section 2.4 became clear that most active SHM systems based on Lamb waves make use of a baseline signal. The same holds for a DI, attributing damage to a structure using a DI is not meaningful without comparing it to a healthy structure. Moreover, the author assumes that without making a comparison, the extend of damage cannot be identified using active SHM. For this reason, the captured Lamb wave signals following from the current state structure should be evaluated against a healthy counterpart signal, which captures the pristine state of the structure. In literature, this signal is often described as a reference or baseline signal. Therefore, from here onwards, signals following from pristine state will be referred to as the baseline signal, while the signals following from a state to be inspected are referred to as damaged signals.

Furthermore, as mentioned at the beginning of this chapter, it is assumed that the presence of damage is the exclusive reason leading to the change in DI. That is, the signals are not influenced by the operational environment, such as changes in temperature or loads.

When comparing signals, differences in their characteristics or wave features can be analysed. Features that describe the behaviour of Lamb waves include for example, the signal amplitude, frequencies, phase and ToA. For this research, signals are first analysed in the time-domain as this was identified to be the starting

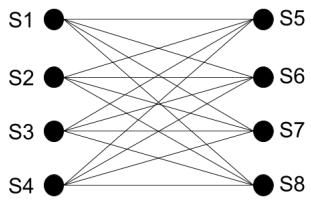

Figure 3.3: Example of an eight-sensor network with 32 sensing paths.

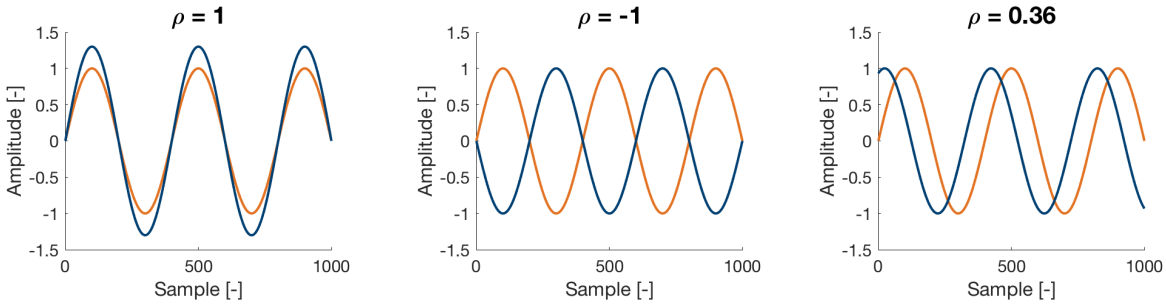

(a) Positive correlation. (b) Negative correlation. (c) Low positive correlation.

Figure 3.4: Illustration of PCC.

point of most image reconstruction algorithms encountered in literature [43, 46, 60]. According to Su et al., there are four general categories that can be used to define a DI in the time-domain [53]; DI's based on the ToA, signal amplitude, energy and signal correlation.

From the start of this research it was attempted to avoid the use of the ToA as a DI. This had two reasons. Firstly, defining the precise ToA for a particular Lamb wave mode is complicated due to scatter and reflections. Moreover, from the author's perspective, using the ToA as DI or for triangulation methods is not favourable for composite structures. This is explained by the fact that this often requires the group velocity to be known which is affected by the structure's fiber orientation and direction of wave propagation due to the structure's anisotropy. Moreover, while the group velocity could be theoretically determined if one knows the lay-up and material properties, many operators and MROs do not have access to this information as it is the intellectual property of an OEM. While it could be argued, that the group velocities can be measured on the structure, this was also considered unfavourable with respect to the required aircraft's downtime.

For this study, it was then decided to build the algorithm based on two different DI's. The first DI being based on Pearson's Correlation Coefficient (PCC) which quantifies the linear relationship between two signals and the second DI based on the differences in signal energy. It was decided to use the PCC, because firstly, early research on image reconstruction makes use of PCC and could function as a comparison to the other DI. It was moreover concluded in Section 2.4.2 that impact damage will cause energy scattering and therefore should lead to changes in the response signal's energy.

3.3.1. Pearson's Correlation Coefficient

The PCC named after its developer Karl Pearson, measures the linearity between two signals and adopts a value between -1 and 1. A positive coefficient indicates that a positive correlation between the two signals exists which means that the movement or behaviour of the two signals are related. A PCC of 1 means that signals a perfectly linear related as is illustrated by the example in Figure 3.4a. When one signal shows an increase, the other signal shows a similar movement. The opposite relation holds for negative correlated signals which is shown in Figure 3.4b. Lastly, a correlation coefficient close to 0 indicates there is no correlation between the signals at all. An example of a low positive correlation is shown in Figure 3.4c.

The PCC is not to be confused with calculating the cross-correlation between two signals which measures the time-shift only. The formula for the PCC is given by

$$\rho = \frac{C_{BD}}{\sigma_B \sigma_D} \quad [-], \tag{3.4}$$

where subscripts B and D indicate the baseline and damaged state signals of the same sensing path[43, 45]. C_{BD} indicates the covariance between two signals and is defined as

$$C_{BD} = \sum_{l=1}^{L} (X_B(l) - \mu_B)^2 \cdot (X_D(l) - \mu_D)^2 \quad [-], \tag{3.5}$$

here, μ_B and μ_D represent the mean of both signals, whereas L defines the length or number of samples the signal contains. σ_B and σ_D represent the standard deviations using the following relations:

$$\sigma_D = \sqrt{\sum_{l=1}^{L} (X_D(l) - \mu_D)^2} \quad [-] \tag{3.6a}$$

$$\sigma_B = \sqrt{\sum_{l=1}^{L} (X_D(l) - \mu_B)^2} \quad [-]. \tag{3.6b}$$

The PCC is then used to deduce a DI ranging between 0 and 1, where 0 indicates no damage and 1 the highest possible distortion of the damaged state signal. For every sensor path, the DI_{a-r} is defined using

$$DI_{pearson} = 1 - |\rho| \quad [-], \tag{3.7}$$

where a and r stand for the corresponding actuator and receiver.

3.3.2. Signal energy

Wave propagation through a structure could also be defined as the transportation of energy contained inside its wave packets. When a wave encounters damage, part of the wave is reflected, scattered or transmitted. This causes a change in the current state signal energy with respect to the baseline signal. The signal energy for a discrete signal is calculated using

$$E_D = \sum_{n=1}^{n=L} (X_D(n)^2) \quad [V^2 \cdot s] \tag{3.8a}$$

$$E_B = \sum_{n=1}^{n=L} (X_B(n)^2) \quad [V^2 \cdot s], \tag{3.8b}$$

here $X(n)$ is sample n of signal X and L is the length of the signal. The DI based on signal energy for a specific pair of sensors, DI_{a-r}, is defined as

$$DI_{energy} = \frac{E_B - E_D}{E_B} \quad [-] \tag{3.9}$$

Mathematically speaking, the calculated DI based on signal energy should now have a higher sensitivity to changes in the signal than when comparing the signal amplitudes. Thereby making the differences between sensor paths more distinct which should lead to an improvement of the algorithm's localization output. The higher sensitivity is caused by the X^2 factor in Equation 3.8.

In this section, the purpose and formulation of two DIs have been explained. The next step of IMRA is to connect the DI to the inspection area. By this the author means to determine to what extend a particular part of the inspection area has had an influence on the disturbance of the response signal. To do so a PIW is used which will be of help during the damage localization process.

3.4. Pixel Intensity Weight

At the beginning of this chapter the assumption was made that damage causes the most severe signal change to paths which are the closest to damage. This means that when considering a particular sensing path, the degree of correlation or similarity between signals measured prior to and after damage is expected to decrease if the sensing path is closer to damage. Using the PIW, this assumption is modelled into the image reconstruction algorithm.

For this reason, the distribution resulting from the PIWs should show a decreasing probability with an increase in distance from the sensor path. There are several ways in which a PIW can be established. For

example, Memmolo et al. have proposed a linear decreasing probability reconstruction, modified linear reconstruction and the probability ellipse. However, most reconstruction algorithms were found to use the probability ellipse and it was therefore chosen as the starting point for the creation of a PIW distribution during this research [43, 45, 46, 61, 62].

The inspection area is first divided into a grid with coordinates ranging over x and y, as illustrated in Figure 3.5a. The probability ellipse then forms an ellipse with the two sensors functioning as the focal points. Outside the ellipse, the influence of damage to the sensing path is assumed to be zero. To do so, a limit to the size of the ellipse is set using a shape factor, β, so that on a straight line between the sensors, the PIW has the value of 1 and linearly decreases to 0 on the ellipse's boundaries.

The probability ellipse is calculated according to

$$R(x,y) = \frac{\sqrt{(X_A - x)^2 + (Y_A - y)^2} + \sqrt{(X_R - x)^2 + (Y_R - y)^2}}{\sqrt{(X_R - X_A)^2 + (Y_R - Y_A)^2}} \quad [-] \tag{3.10a}$$

$$\text{if} \quad \beta > R(x,y) \quad \text{then} \quad S(x,y) = \frac{\beta - R(x,y)}{\beta - 1} \quad [-] \tag{3.10b}$$

$$\text{and if} \quad \beta \leq R(x,y) \quad \text{then} \quad S(x,y) = 0 \quad [-]. \tag{3.10c}$$

For every pixel (x,y) on the grid, first the R value is created. R indicates the ratio of the length of the major axis, a, over the distance between the two focal points, $|\,AR\,|$. (X_A, Y_A) and (X_R, Y_R) are the coordinates of the actuator and sensor, while (x, y) indicates the location of the pixel and $S(x, y)$ represents the value of the PIW.

The shape factor β determines the dimensions of the ellipse as in

$$\text{Major axis:} \quad a = \beta * |\,AR\,| \quad [m] \tag{3.11a}$$

$$\text{Minor axis:} \quad b = |\,AR\,| \cdot \sqrt{\beta^2 - 1} \quad [m]. \tag{3.11b}$$

In most studies, the value of beta is set to 1.05, but lower values in the range of 1.02 and higher values, 1.5 have also been mentioned [45, 62].

An example of a grid containing actuator A and receiver R is shown in Figure 3.5a. For every (x, y) combination the PIW has been defined, which adds up to the probability ellipse as shown in Figure 3.5b and 3.5c. It can be seen that the direct path between the actuator and receiver indeed has the value of 1 while on the ellipse's boundaries the values reduce to 0. The dimensions of the grid are by way of illustration, as the graphs are shown to demonstrate the different PIWs that correspond to every pixel.

The final step in the image reconstruction is the data fusion during which the DIs have to be added to the PIW distributions to form one reconstructed image.

3.5. Data Fusion

For each PIW distribution or S_{a-r}, a probability distribution is created by multiplying the PIW distribution with the corresponding DI. Hereafter, the images are superimposed to create a final reconstructed image which shows the pixels with the highest probability of damage. This is illustrated in Figure 3.6.

For every path, the DI_{a-r} and corresponding $S(x,y)_{a-r}$ are multiplied for all pixels, (x, y). The pixel intensity is then determined by taking the sum over all paths as shown in

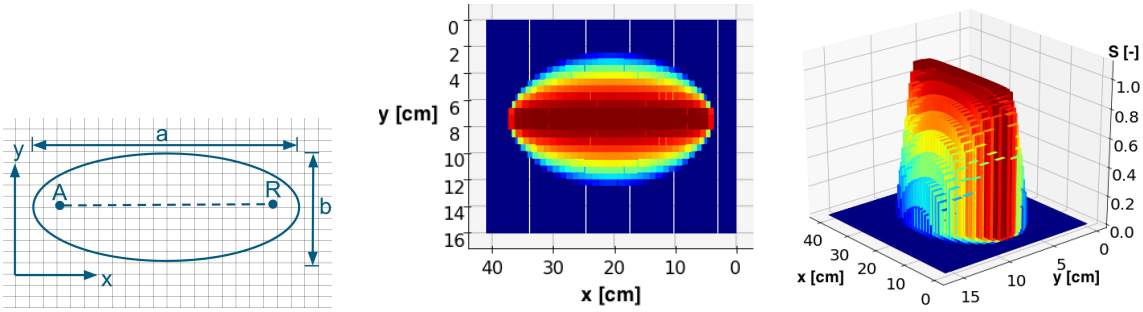

(a) Example of an inspection grid. (b) PIW distribution in 2D. (c) PIW distribution in 3D.

Figure 3.5: Illustration of the PIW.

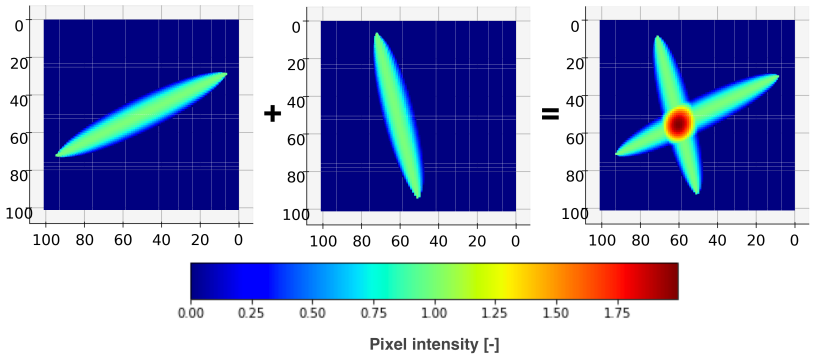

Figure 3.6: Principle of data fusion for IMRA.

$$P_{int}(x,y) = \sum_{a=1}^{m} \sum_{r=1}^{n} S_{a-r}(x,y) \cdot DI_{a-r} \quad [-], \tag{3.12}$$

where m&n stand for the actuator and receiver numbers. The reconstructed image the shows a probability distribution of damage over the inspected area. Although most studies define this final outcome of each pixel as a probability of damage, for this research, the author proposes to give it the name; pixel intensity. In the author's opinion, pixel intensity is more appropriate as the value resulting for data fusion is not representing a real probability, but a likelihood of damage in comparison to the other pixels. Only after setting an appropriate threshold to this probability distribution or to the individual pixels, the final location and size of damage might be estimated. This is due to the usage of the probability ellipse which will always causes some pixels to show higher pixel intensities than others. However, in order to select a suitable threshold, first the term 'damage' should be defined and quantified with respect to the MRO industry so that the user knows what should (not) be considered damage.

3.6. Definition of damage

In 'The Fundamental Axioms of Structural Health Monitoring', Worden identified damage as: *"A change to the material and/or geometric properties of a system, including the material and/or geometric properties of the system including changes to the boundary conditions and system connectivity, which adversely affect the current or future performance of the system" [6].*

In hierarchical order, Worden puts the definition of *defects* before *damage* and states that every structure inherently contains defects even when it is considered to operate on its optimum. The term *fault* is used to describe the state of a structure when it is unable to perform its intended function. This definition of damage therefore implies that it is a relative concept and so damage cannot be defined or detected without making a comparison. which also became clear while choosing a damage index in Section 3.3.

In the author's opinion, something should be added to this definition before it can be used in combination with SHM and the MRO industry in particular. In order to perform a structural inspection boundaries should be applied to the definition of damage. By this, the authors means that it should be decided what changes in material or geometric properties should be considered a defect, damage or a fault.

In terms of aircraft maintenance, the author now proposes to use the following boundaries to the definition of damage. A structure is considered to be damaged when the changes to the structure are exceeding the ADL as provided by the SRM. In this case changes to the structure could be caused by the damage mechanisms described in Section 2.2. For a fuselage skin structure containing impact damage, the ADL for a delamination is a delamination length of $50.8mm$ [26]. Besides the length of impact damage, the SRM also included limits on the depth of the delamination and the sizes of intralaminar cracks. However, these are considered outside the scope of this project.

3.7. Threshold selection

The image reconstruction algorithms presented in literature such as RAPID do not cover the selection process of thresholds. However, in order to detect and monitor damage growth a threshold has to be selected and added to the algorithm. Some articles have proposed to set a relative threshold to the pixel intensity in

case an algorithm is to be used for growth monitoring, but not investigated the use of a threshold into detail. For this reason four threshold methods have been analysed using a dataset obtained from the NASA prognostics Data Repository. These four threshold methods are stated below. The outcome of the analysis will be discussed Section 4.5.

Method 1: Setting a relative threshold to the pixel intensity
A common threshold method that was proposed in literature was to set a relative threshold to the final output, the pixel intensity. The following procedure was proposed [43, 63, 64]:

$$\begin{aligned} &if \quad P_{int}(x,y) \geq V_{thres} * max(P_{int}) \\ &\quad then \quad P_{int}(x,y) = 1 \\ &\quad else \quad P_{int}(x,y) = 0 \end{aligned} \tag{3.13}$$

Method 2: Setting a value threshold to the pixel intensity
Another method that was considered was to set a limit to the pixel intensity itself. Pixels are considered damage when [46]:

$$\begin{aligned} &if \quad P_{int}(x,y) \geq P_{thres} \\ &\quad then \quad P_{int}(x,y) = 1 \\ &\quad else \quad P_{int}(x,y) = 0 \end{aligned} \tag{3.14}$$

Method 3: Setting a threshold to the DI and pixel intensity
Other SHM systems which do use a DI, but do not make use of image reconstruction, propose to set a threshold to the DI. This is why it is also proposed to put a threshold to the DI for IMRA. In this way, only sensing paths that cross the DI threshold will contribute to the image reconstruction. Hereafter a threshold to the pixel intensity using either of the two methods discussed above can be used for the final evaluation:

$$\begin{aligned} &P_{int}(x,y) = 0 \\ &\quad for \quad a = 1...m \\ &\quad\quad for \quad r = 1...n \end{aligned} \tag{3.15}$$

$$\begin{aligned} &if \quad DI_{a-r} \geq DI_{thres} \\ &\quad then \quad P_{int}(x,y) = P_{int}(x,y) + PDW_{a-r}(x,y) \cdot DI_{a-r} \end{aligned} \tag{3.16}$$

Method 4: Setting a threshold to the change in pixel intensity
When high values for the DI are found for a majority of the sensing paths, the image reconstruction tends to accumulate damage at the middle of the panel. This is due to the bias introduced by the probability ellipse in combination with the density of the sensor array, which will also be shown in Section 4.5. In order to lower the influence of the bias on the algorithm and still monitor the growth, the author proposes to set a threshold to the change in pixel intensity before and after damage instead. This allows the use of all information that results from the sensing paths. The methods considers each pixel individually which means that the pixel intensity calculated using the PIW values only is compared to the pixel intensity resulting from the PIW and DI values combined.

A small adjustment is made to calculate the PIW in order to avoid a division by zero. Equation 3.10 is changed to

$$
\begin{aligned}
&R(x,y) = \frac{\sqrt{(X_A - x)^2 + (Y_A - y)^2} + \sqrt{(X_R - x)^2 + (Y_R - y)^2}}{\sqrt{(X_R - X_A)^2 + (Y_R - Y_A)^2}} \quad [-] \\
&\text{if} \quad \beta > R(x,y) \\
&\quad \textit{then} \quad S(x,y) = \frac{\beta - R(x,y)}{\beta - 1} + 1 \quad [-] \\
&\textit{else} \quad S(x,y) = 1 \quad [-].
\end{aligned} \tag{3.17}
$$

Next, 1 was added to the DI values, so that $DI_{pearson} = 2 - \mid PCC \mid$ and $DI_{energy} = \frac{\Delta E}{E_B} + 1$. The pixel intensity change is then defined as

$$
P_{change}(x,y) = \frac{\sum_{a=1}^{m} \sum_{r=1}^{n} PDW_{a-r}(x,y) \cdot DI_{a-r}}{\sum_{a=1}^{m} \sum_{r=1}^{n} PDW_{a-r}(x,y)} \quad [-]. \tag{3.18}
$$

It is expected that this will allow the user to see how damage severity progresses inside the inspected structure.

4

Algorithm Verification and Analysis

During the initial set up, verification and analysis of IMRA presented in Chapter 3 a dataset from the NASA Prognostics Data Repository has been used [14]. This dataset has been created and used by NASA to research estimating the RUL of structures and materials using prognostic algorithms. Data capturing damage growth which is required to train those prognostic algorithms is rarely available from industry. Therefore, NASA performed several experiments to create a dataset including Lamb wave signals through CFRP specimen subjected to run-to-failure tension-tension fatigue tests in order to simulate accelerated ageing. Damage progression in the specimen was measured by pausing the fatigue tests several times during which response data was collected.

The difference between this research and the research by NASA is that this research aims at creating a model that is capable of defining the current state of a structure and monitor its progress, while the research presented by NASA aims to predict damage progression when the current health state is confirmed by a conventional inspection technique. From the MRO perspective, at this moment in time, a higher priority lies with monitoring the health of a structure instead of predicting its RUL as it is believed that this will sooner lead to financial benefits.

Although this research focusses on the monitoring of impact instead of fatigue damage, this NASA dataset can be used as a primary step towards the verification and validation process of the algorithm. Moreover, by analysing the response of the algorithm's output to the NASA dataset, decisions for the subsequent research steps can be made. This chapter starts with introducing the NASA test specimen in Section 4.1. The next section examines some of the obtained baseline signals. Hereafter, a decision is made between using the windowed signals and the full signals in Section 4.3. The DI values found based on the calculations shown in Section 3.3 are discussed in Section 4.4. The initial results of the image reconstruction algorithm for the dataset presented in this chapter are shown in Section 4.5. Finally, Section 4.6, reflects upon the performed analysis and results found.

4.1. Test specimen

One of the test specimen is shown in Figure 4.1a. All specimen were manufactured out of Torayca T700G unidirectional carbon-prepreg, with dimensions $15.24cm$ by $25.4cm$, having a dog-bone geometry. A notch was created onto the specimen to induce stress concentrations and initiate delamination during testing. NASA made use of PZT disc sensors to periodically interrogate the specimen. The sensor configuration, also shown in Figure 4.1a, was the same for all specimen. The sensors on the right-hand side $(1-6)$ functioned as actuators while the sensor on the left-hand side $(7-12)$ functioned as receivers. Thus creating 36 actuator-receiver paths or sensing paths in total.

The specimen was fatigue tested on a MTS tensile testing machine and paused several times during which measurements were taken, i.e. Lamb wave signals were recorded. The measurements were taken for seven different excitation frequencies, $f_c = 150, 200, 250, 300, 350, 400$ & $450kHz$, and amplified using a gain of 20dB. The excitation signal used by NASA was a five -cycle sine wave multiplied by a Hanning window at 50 Volts as shown for $f_c = 200kHz$ in Figure 4.1b. Besides, recording Lamb wave signals, X-ray images were taken from the majority of the specimen which could be used for validation.

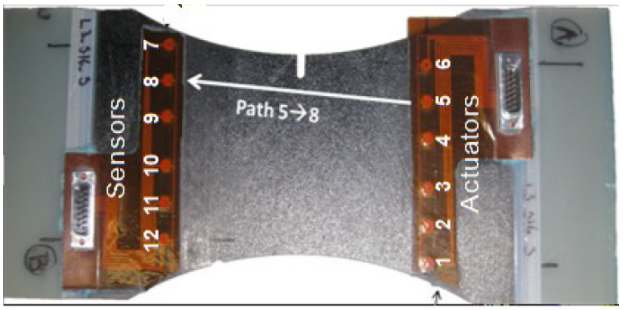

(a) One of the NASA CFRP test specimen [14].

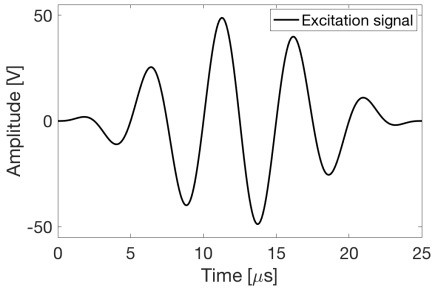

(b) Five-cycle Hanning window at $f_c = 200kHz$.

Figure 4.1: NASA test specimen and one of the excitation signals.

Three different lay-ups were used to manufacture the specimen:

- lay-up 1: $[0_2/90_4]_s$
- lay-up 2: $[0/90_2/45/-45/90]_s$
- lay-up 3: $[90_2/45/-45]_{2s}$.

The analysis and results presented in the remainder of this chapter are all based on database *L1S19* containing Lamb signals for specimen having lay-up 1. It was decided to demonstrate this dataset because compared to lay-ups 2 & 3, it showed a more gradual growth of the delaminated area on the X-ray images. This allowed the dataset to be used for an analysis of the algorithm's response to damage growth.

Initially, lay-up 2 was favoured as this lay-up best approaches a quasi-isotropic lay-up, therefore representing a fuselage skin the best [65]. However, the data showed a lack of correspondence between the signals and the X-rays or for other measurements the delamination on the X-ray image was rather large, making it difficult for the algorithm to distinguish paths that encounter damage and paths that should not.

Lay-up 3 was excluded from the analysis as well, because from the X-ray images could be seen that very little delamination occurred, but that almost the entire specimen was covered with vertical intralaminar cracks, so that most paths would experience similar forms of damage.

Eventually it was found that dataset *L1S19* with lay-up 1 showed the best compromise between data availability and damage growth. However, it should be noted that a disadvantage of this panel is its relative high fiber content in the 90°-direction, resulting in many transverse intralaminar cracks during tension-tension fatigue testing.

For code verification and analysis, all actuator-receiver combinations or sensing paths, have been numbered. The path numbering belonging to each actuator-receiver combination as in Figure 4.1a is shown in Table 4.1.

Table 4.1: Path numbers corresponding to the sensor configuration in Figure 4.1a.

Path	**Actuator**	**Receiver**	**Path**	**Actuator**	**Receiver**	**Path**	**Actuator**	**Receiver**
0	1	7	**12**	3	7	**24**	5	7
1	1	8	**13**	3	8	**25**	5	8
2	1	9	**14**	3	9	**26**	5	9
3	1	10	**15**	3	10	**27**	5	10
4	1	11	**16**	3	11	**28**	5	11
5	1	12	**17**	3	12	**29**	5	12
6	2	7	**18**	4	7	**30**	6	7
7	2	8	**19**	4	8	**31**	6	8
8	2	9	**20**	4	9	**32**	6	9
9	2	10	**21**	4	10	**33**	6	10
10	2	11	**22**	4	11	**34**	6	11
11	2	12	**23**	4	12	**35**	6	12

4.2. Baseline signals

The dataset was obtained in a *Matlab* format. Because KLM E&M normally uses *Python* for their algorithms, it was decided to work in *Python*. The first step in the code verification was then to convert the dataset from a *Matlab* to a *Python* file and extract the information from the dataset that is shown below. The signals were subsequently compared in *Matlab* & *Python* after which the conversion was found successful.

The following information was extracted from the datasets:

- Excitation frequency
- Sampling frequency
- Excited signals for each path number
- Received signals for each path number
- Number of fatigue cycles

The baseline signals provided by NASA are the recorded signals corresponding to zero fatigue cycles. Two baseline signals with a difference in the excitation frequency, 150 & 250kHz are shown in Figure 4.2 for path 16, actuator 3 & receiver 11. There are some initial comments which can be made about the baseline signals. Firstly, it could be seen that for $f_c = 150kHz$ a clear separation between the fundamental modes $S0$ and $A0$ is visible, where the first wave package is the $S0$ mode and the second wave package the $A0$ mode. However, in Figure 4.2b can be seen that starting from $\approx 45\mu s$ different modes start to overlap creating a much higher amplitude. This is a result from the increased excitation frequency. The change in frequency leads to a change in the wave mode velocity which causes reflections to overlap with the direct $A0$ wave package. The $A0$ mode can therefore no longer be separated from reflections caused by the geometric boundaries of the specimen. The $S0$ mode does remain separable.

Furthermore, from other paths such as path 12, actuator 3 & receiver 7, could also be seen that for an increased distance between the sensors the difference in ToA of the modes increases as well, which is shown in Figure 4.2c. This is as expected since the distance between the sensors increases which causes a larger difference between the arrival times. It can also be seen that the $A0$ mode suffers from attenuation more than the $S0$ mode does over this distance. This can be attributed to the difference in particle motion.

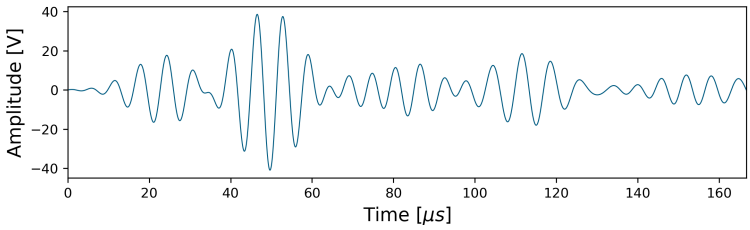

(a) Baseline signal for path 16, actuator 3 - receiver 7 at $f_c = 150kHz$.

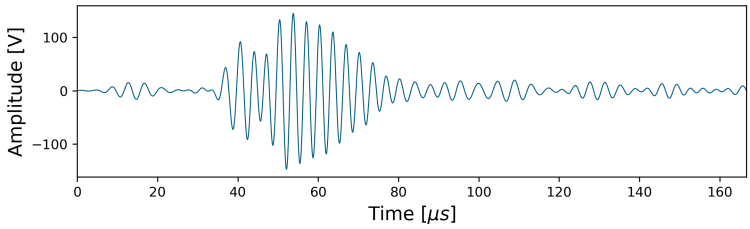

(b) Baseline signal for path 16 actuator 3 - receiver 7 at $f_c = 250kHz$.

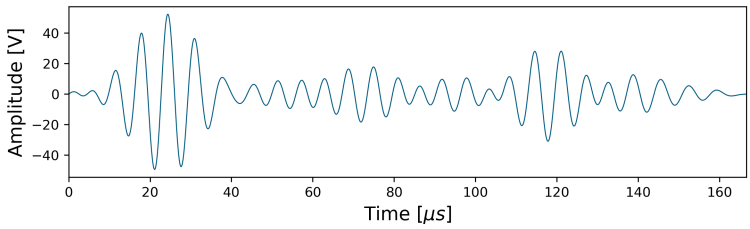

(c) Baseline signal for path 12, actuator 3 - receiver 7 at $f_c = 150kHz$.

Figure 4.2: Baseline signals for 2 different excitation frequencies.

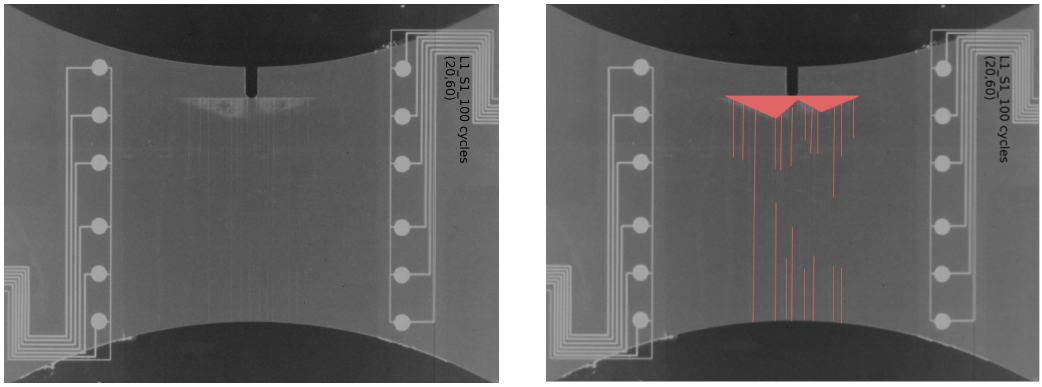

(a) Original X-ray image.

(b) X-ray image with the damage highlighted.

Figure 4.3: X-rays taken from dataset L1S19 after 100 fatigue cycles.

4.3. Direct wave propagation

The X-ray image taken from dataset L1S19 at 100 fatigue cycles is shown in Figure 4.3a. The image shows that the specimen contains interlaminar cracks close to the notch. The image also shows several intralaminar cracks in the 90° direction which likely initiated in the matrix of the 90° oriented plies. Figure 4.3b shows the same image but with the delamination and clearest matrix cracks highlighted.

A decision was made to either use the direct signals as described in Section 3.2 or the entire signals with a constant duration as provided by the dataset. When these direct signals, the full or entire signals, and also their corresponding DIs for 100 fatigue cycles were analysed in combination with Figure 4.3 it was found that there are several disadvantages to windowing the signals which will be shown by means of Figure 4.4. This figure shows the received signals for path 25, actuator 5 & receiver 8 for which the direct waves travel through the delaminated area of the specimen.

The first noticeable point is that the $A0$ mode indeed seems to be more affected by damage in Figure 4.3 than the $S0$ mode for which a clear change in signal amplitude can be seen with an increase in the number of fatigue cycles. Using the windowing method, damage growth cannot be represented as this behaviour of the $A0$ mode is not captured by the DI. Moreover, from Figure 4.4b can seen that if modes are overlapping or the difference in arrival time is limited, the boundaries of the window have an influence on the DI. When the window in 4.4b would be smaller by for example cutting the signal between 25&30μs, the change between the signals becomes smaller as well. It was observed that using this method might then lead to very high DI values compared to other paths encountering similar damage mechanisms. Assuming that the DI increases for an increase in damage, windowing a signal should not be a very big problem when considering an SHM technique using a single path. However, for this image reconstruction technique the DI is not only used to detect damage, but the DI relative to other sensing paths is important as well as it is used to determine the damage location. In the author's opinion, windowing the signals removes the ability to compare the paths relatively and thus to use this information to say something about the damage location and its severity.

It was stated before that the $A0$ mode seems to be more affected by the damage in Figure 4.3. Using this information, one might argue that windowing around the $A0$ mode would be a better idea. However, when referring back to Figure 4.2b in the previous section, it can be seen that the $A0$ mode is difficult to separate as it might show overlap with other modes and reflections from boundaries. For the reasons above it was thus decided to use the full signals when calculating the DI. Moreover, the overlap and uncertain window strategy also illustrates why the author was not in favour of using the ToA as a way to define the DI as was previously mentioned in Section 3.3.

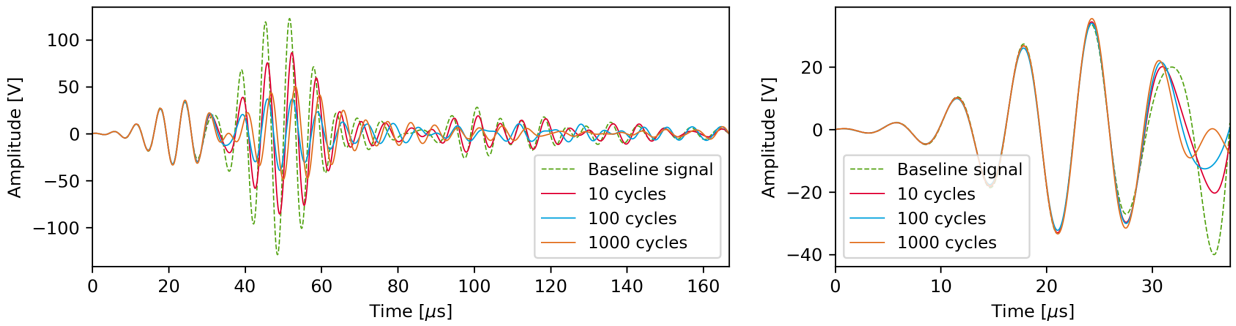

(a) Full response signals.

(b) Direct propagated signals.

Figure 4.4: Received signals for path 25, measured after 10, 100 & 1000 cycles for $f_c = 150kHz$.

4.4. Damage Index

In this section the calculated damage indices for the NASA dataset are analysed. The DIs found for L1S19 after 100 fatigue cycles are used as an example. It was decided to analyse the DIs after 100 cycles, because the length of the delamination is about $55mm$. In the previous chapter was found that the allowable damage limit of a delamination according to the Boeing SRM is set $50.8mm$ for the fuselage skin [26]. Therefore, the DIs found for these measurements after 100 cycles should indicate damage. The first two subsections analyse the DI based on the PCC, $DI_{pearson}$ and signal energy, DI_{energy}. The third subsection offers a comparison between the two.

4.4.1. Pearson's Correlation Coefficient: Analysis

Figure 4.5 shows the calculated DIs for all path numbers based on the PCC for measurements taken at $200kHz$ & $400kHz$. A first observation is that for $200kHz$ there is an actual difference between the DIs related to paths propagating through the delamination and to paths further away. For example path 24, actuator 5 & receiver 7, shows a DI of 0.810 while path 10, actuator 2 & receiver 11, only shows a DI of 0.048, which indicates almost no damage at all.

A second observation is the increase in DI for an increase in the central excitation frequency when comparing the DI for $200kHz$ to $400kHz$. This is expected for parts of the waves that propagate through damage. These waves have a smaller wavelength and will therefore interact more with damage. It also means that damage might be detected which could not be detected in the lower frequency ranges. Consider path 10, actuator 2 & receiver 11, which shows a small DI for $200kHz$. The wave clearly propagates through the cracks in the area below the delamination. At $400kHz$ the DI is significantly higher than at $200kHz$, 0.048 versus 0.928. The transverse intralaminar cracks will thus have an effect on the paths, while at $200kHz$ the waves pass over the cracks. An general increase in the DI for several other central excitation frequencies is also shown in Appendix C measured after 100 fatigue cycles.

Generally, by increasing the central excitation frequency, the waves will be more affected by discontinuities inside the structure. This might allow one to argue that this will increase the resolution or accuracy of the DI. While the author agrees with the DI becoming more sensitive to damage when using higher frequencies, it becomes apparent from Figure 4.5b that the differences between paths becomes less distinct. Therefore, the author expects that successfully locating the delamination and separating it from matrix cracks becomes more difficult. Moreover, from Figure 4.5 can be seen that at $200kHz$ path 25 and 31 are showing higher DIs compared to $400kHz$. This shows that for certain cases a higher excitation frequency does not lead to higher DI values. A possible explanation for this will be discussed in Subsection 4.4.3.

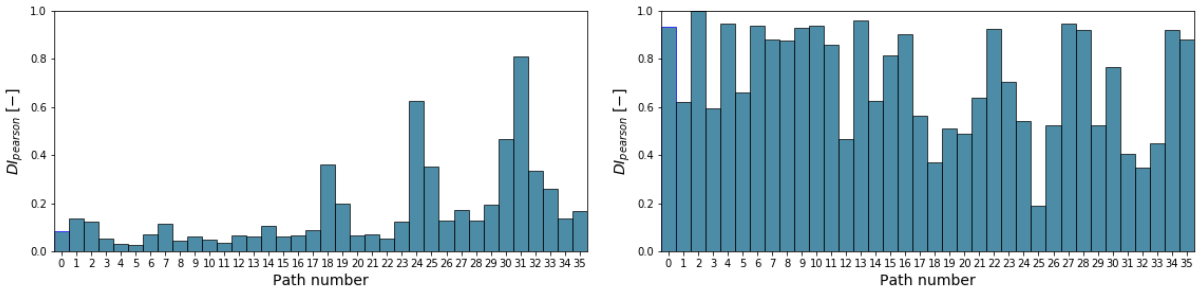

(a) Pearson damage index at $f_c = 200kHz$.

(b) Pearson damage index at $f_c = 400kHz$.

Figure 4.5: Pearson damage indices L1S19 after 100 fatigue cycles.

4.4.2. Signal energy: Analysis

Figure 4.6 shows the DI calculated using the signal energy for the same specimen and data as in the previous section. From the figures can be seen that the differences between paths close to the delamination, paths $24-35$, are less distinct for $200kHz$ than for the DI based on PCC in Figure 4.5a. Similarly as for the PCC, overall the DI increases for an increase in frequency. What can seen more clearly from Figure 4.6b than from 4.5b is that for paths crossing the middle of the plate the DI remains low where according to the X-ray in 4.3 are almost no cracks. This also holds for the higher frequencies, e.g. paths 16, 17 & 34.

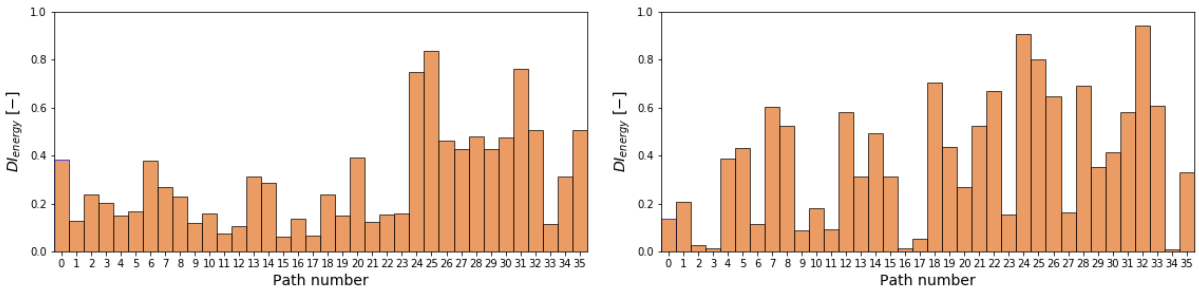

(a) Energy damage index at $f_c = 200kHz$.

(b) Energy damage index at $f_c = 400kHz$.

Figure 4.6: Energy damage indices L1S19 after 100 cycles.

It was stated in Section 3.1 that an increase in DI value is assumed for an increase in damage. To illustrate that the DI value indeed increases for both $DI_{pearson}$ and DI_{energy}, the DI values are plotted against the number of fatigue cycles for paths between actuator 5 and receivers 7-12 in Figure 4.7.

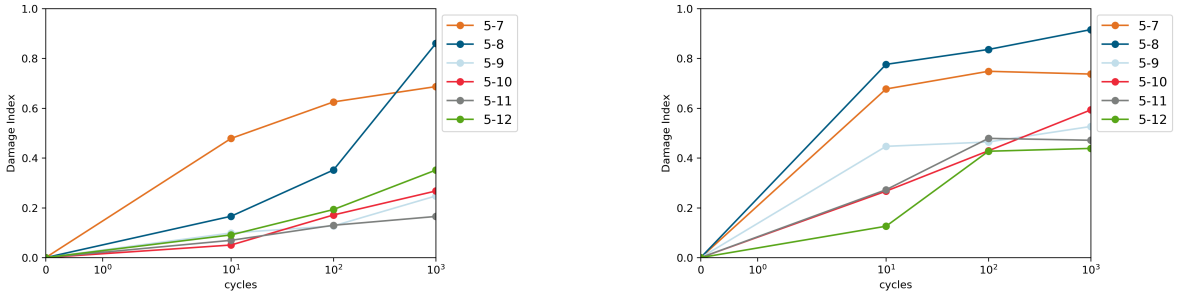

(a) $DI_{pearson}$ increase.

(b) DI_{energy} increase.

Figure 4.7: Damage index increases for actuator 5 and receivers 7-12 at $f_c = 200kHz$ for an increase in damage.

4.4.3. Comparing PCC and signal energy

In this subsection the DIs based on the PCC and signal energy are compared. Figure 4.8a shows the DI based on signal energy and the PCC measured at $200kHz$ after 100 cycles. The figure shows a higher DI based on

signal energy for almost all sensing paths with the exception of the paths crossing the delamination directly, e.g. paths 18, 19 & 31. Using $f_c = 200kHz$, this trend was also visible for a different numbers of fatigue cycles which can be seen in Appendix C. The graph seems to indicate that the PCC is making a higher distinction between paths directly propagating through the delamination and paths which do not compared to the DI based on signal energy.

The second figure, Figure 4.8b shows the comparison for $400kHz$ after 100 fatigue cycles. In this case the DIs based on PCC are overall much higher. What also becomes clear is that there are very large differences between $DI_{pearson}$ & DI_{energy} for a number of paths. Consider for example path 34, here the $DI_{energy} = 0.019$, while $DI_{pearson} = 0.918$. The opposite can be concluded when considering path 25 for which $DI_{energy} = 0.802$ while for $DI_{pearson} = 0.188$ was found.

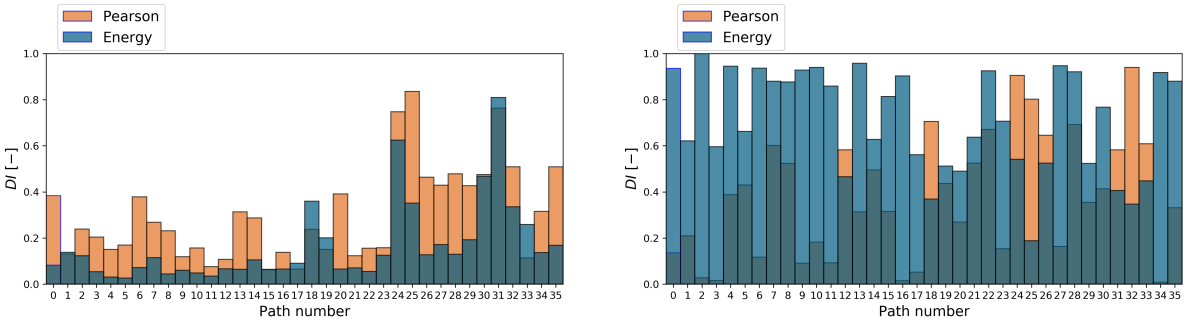

(a) DI comparison at $f_c = 200kHz$.

(b) DI comparison at $f_c = 400kHz$.

Figure 4.8: DI comparison between PCC and signal energy after 100 fatigue cycles.

The baseline and response signals of path 34 and 25 are shown in Figure 4.9. From these figures a first important conclusion might be drawn. The magnitude of the DI for this specimen depends both on the central excitation frequency and the type of signal processing or the formulation of the DI. When referring back to Figure 4.3, it can be seen that path 34 is not propagating through the delamination directly, but some of the reflections reaching the receiver do travel through the delaminated area. It can also be seen that most of the signal disturbance manifests itself in the reflections and therefore show at a later moment in time. The direct waves of path 25 do propagate through the delaminated area, but mainly show attenuation which is shown in Figure 4.9b. A time-shift of the $A0$ mode is visible, but the wave's shape is still quite similar.

What is important to take away from these two images is that by looking at these images, one would for both cases clearly argue that there is a change in the structure which causes a distortion of the response signals compared to the baseline. This distortion could be identified as damage. However, when calculating the DI this distortion does not become clear for path 34 using DI_{energy} and for 25 using $DI_{pearson}$. In conclusion, it means that the DIs are not always capable of capturing damage. This is similar to one particular NDT technique not being capable of detecting all types of damage mechanisms. This should be taken into consideration when designing an SHM system. A possible solution to overcome this problem could be to design a system which calculates the DIs in different manners or to use more than one sensing path for the decision-making.

Although it was mentioned in Section 2.4.2 that is it not possible to define the interaction between Lamb

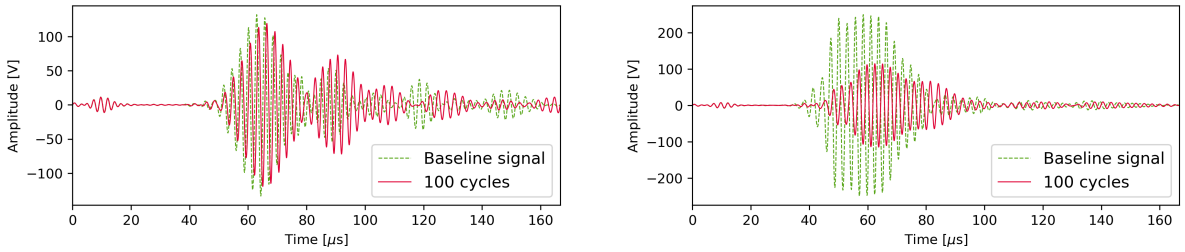

(a) Path 34, actuator 6-receiver 11 at $f_c = 400kHz$.

(b) Path 25, actuator 5-receiver 8 at $f_c = 400kHz$.

Figure 4.9: Response signals at $f_c = 400kHz$ and 100 fatigue cycles showing a different response to damage.

waves and damage completely, several theories might be used to explain the behaviour of the signals in Figure 4.9 and the values found for the DIs in Figures 4.8.

From Figure 4.8a and Appendix C could be concluded that mainly at the lower frequencies, the $DI_{pearson}$ makes a high distinction between paths crossing and not crossing the delaminated area of the specimen. Figure 4.10 shows the received signals of three paths.

- The first signal in Figure 4.10a shows the received signal for path 13 between actuator 3 & receiver 8. Comparing the response to the X-ray in Figure 4.3 it can be seen that this path mainly encounters transverse matrix cracks.
- In a similar manner, Figure 4.10b shows the response for path 18, actuator 4 & receiver 7, which crosses the delaminated area directly.
- Lastly, Figure 4.10c presents the Lamb waves received for path 21, actuator 4 & receiver 10, which according to Figure 4.3 should barely face damage on its direct propagation path.

These three figures give rise to the idea that damage mechanisms have different ways of interfering with Lamb waves. They show that for this particular panel and $f_c = 200kHz$, a delamination affects the wave's shape by adjusting the velocity of wave packages and by introducing additional wave packages which are either due to reflections or due to mode conversion. Moreover, it also seems that transverse cracks encountered by for example path 13 in Figure 4.10a mainly cause attenuation and not so much a change in the wave's shape.

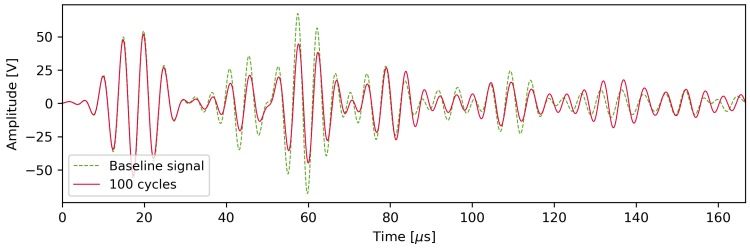

(a) Path 13 , actuator 3-receiver 8, measured at $f_c = 200kHz$.

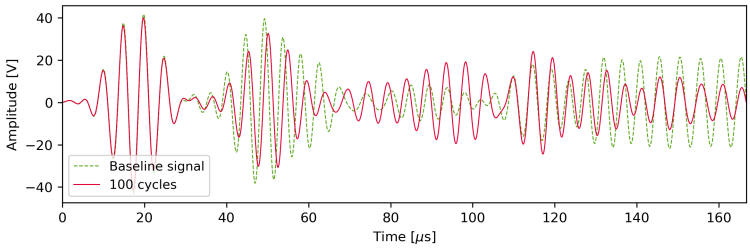

(b) Path 18, actuator 4-receiver 7, measured at $f_c = 200kHz$.

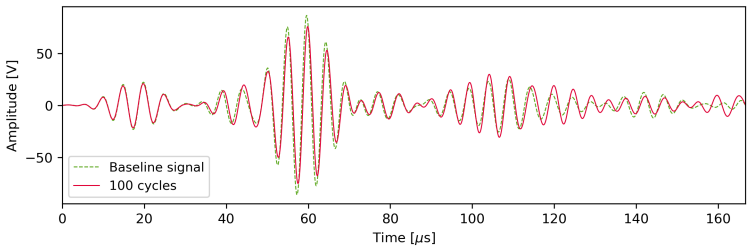

(c) Path 21, actuator 4-receiver 10 , measured at $f_c = 200kHz$.

Figure 4.10: Response signals at $f_c = 200kHz$ and 100 fatigue cycles showing a different behaviour to damage

Several other researchers have mentioned a change in a signal's waveform caused by a delamination [31, 66–68]. This behaviour is explained for an layered plate with isotropic plies by *Ricci et al.* using a five-layered laminate as shown in Figure 4.11 [68]. This plate can be divided into three zones where the thickness of the layers is $t1 << t2$;

It was concluded earlier that the $A0$ mode shows a larger sensitivity to the damage than the $S0$ mode. Therefore, assume that a Lamb wave containing only the anti-symmetric $A0$ is excited by the PZT sensor in

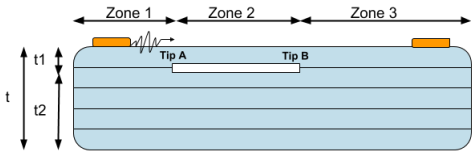

Figure 4.11: Lamb wave interaction with delamination

Zone 1. In this zone, Lamb waves are generated at the surface. The waves propagate towards Zone 2 which contains a delamination. When the wave encounters Tip A, part of the wave is reflected back into Zone 1 and part of the wave is transmitted into Zone 2. Because the layer above the delamination has a smaller thickness than the layer below the delamination, the acoustic impedance of the layer above the delamination is lower. As a result, the largest portion of the wave that is transmitted into Zone 2 will propagate through the upper part of the panel. The smaller thickness will cause the part of the wave which travels through upper part to change from velocity. In this case when measuring in the lower frequency regime for isotropic layers, it causes the wave to slow down and thus show a delay in the response signals. When the wave reaches Tip B, part of the wave is again either transmitted into Zone 3 or reflected back into Zone 2 which compared to Zone 3 will have lower impedances. This causes part of the wave to be captured between Tip A and Tip B, thereby decreasing the energy of the response signal [68].

For the $S0$ mode, the author assumes the described behaviour to be less severe. This is due to the difference in particle motion but it will also be affected by the dispersion curve. Depending on the 'location' on the dispersion curve or $f \cdot d$, the change in $S0$ velocity can be absent or small. In the very low frequency regime it can even cause the $S0$ mode to increase speed over the delamination due to its dispersive behaviour as was shown by Takeda et al. [69].

The principles above will also occur for anisotropic laminates as discussed by [66]. Inside an anisotropic laminate the Lamb waves will propagate towards the delamination with the same velocity through the thickness of the laminate. The delamination will cause the wave to be separated and allow the waves to propagate above and below the delamination with a different velocity. Behind the delamination the packages merge and continue to propagate with the same velocity. Thus, similar to the model by [68], the response signals can feature signal shifts.

A difference with an anisotropic material will be that the change in velocity is less predictable. It will depend very much on the lay-up, the direction of wave propagation and the location of the delamination through the thickness of the plate. For an isotropic material it becomes clear that the upper layer in Figure 4.11 will have a lower impedance, but for a composite showing anisotropic behaviour this does not always have to be the case. If the change in velocity is to be quantified exactly, the dispersion curves should be known.

Several other researchers have more specifically investigated the behaviour of Lamb waves in delaminated cross-ply laminates similar to the *L1S19* specimen [31] [67]. It was found that under tensile loading, transverse matrix cracks initiate in the 90° oriented layers. At the interface of $0° - 90°$ plies these matrix cracks can grow into delaminations. Having the 0° layers located on the outer plies of the laminate, this causes the outer plies to be isolated. This outer layer, due to its relatively higher 0° content, will have a higher stiffness than the undamaged laminate so that the waves will propagate faster through this outer layer. This can also result in a temporarily increase the energy of the transmitted signal.

Overall, this theory can be used to firstly explain why the $A0$ mode seems more sensitive to damage than the $S0$ mode. Because of the particle motion of the $A0$ mode the author assumes that this mode will be more affected by the wave separation that is forced by a delamination. Secondly, it explains why the $DI_{pearson}$ is more sensitive to delaminations than is seems to be to intralaminar cracks. The delamination will mainly cause a shift in the signal while it is expected that the intralaminar cracks will mainly cause reflections, thus attenuation.

Previously, it was stated that for an increase in frequency the wave should be more sensitive to damage due to a decreased wavelength. The theory above also helps to explain the difference in DI for path 25 in Figure 4.5a & 4.5b at the beginning of this section. The DI at $200kHz$ was significantly higher compared to the DI at $400kHz$. In this case, the author suspects that in this region on the dispersion curve, for an increase in frequency, the $A0$ mode is less dispersive so that velocity change due to the delamination will be less severe. Besides, because of the specimen's shape, the signal from path 25, actuator 5 & receiver 8, hardly contains reflections. This means that the signal is also not affected by reflections travelling through or around the

damage. This overall leads to a lower DI value while still propagating through the damage directly.

On a final note, there are a few things that should be taken into account when using this theory to explain signal behaviour. The behaviour of waves according to this theory is only valid up to a certain extend of the damage and is very much depending on the laminate's lay-up. It was also seen that when the damage becomes severe or the frequency increases, the PCC cannot differentiate the delamination from intralaminar crack as the signal shift and mode conversions will also be caused by the multiple intralaminar cracks and other damage mechanisms that might occur. An increase in damage severity or the occurrence of other damage mechanisms such as fiber breakages, might also reduce the effects due to a decrease in stiffness.

4.5. Image reconstruction

This section analyses the output of IMRA for three different damage states corresponding to 10, 100 & 1000 fatigue cycles. The X-ray images for specimen L1S19 with highlighted damage are shown in Figure 4.12. The original X-rays are shown in Appendix D. The results presented in this section follow from the measurements taken at $f_c = 200kHz$. This dataset with a central excitation frequency of $200kHz$ showed the best compromise between the lower and higher sensitivities to damage in combination with the chosen DIs.

The first subsection presents the results based on the initial algorithm as presented in Chapter 3. It can be used to determine the location with the highest probability of damage. However, in order to determine if damage is really present as well as to monitor its growth, the algorithm requires the user to determine what should be considered a damaged structure and subsequently apply several thresholds. This is discussed in the next subsections.

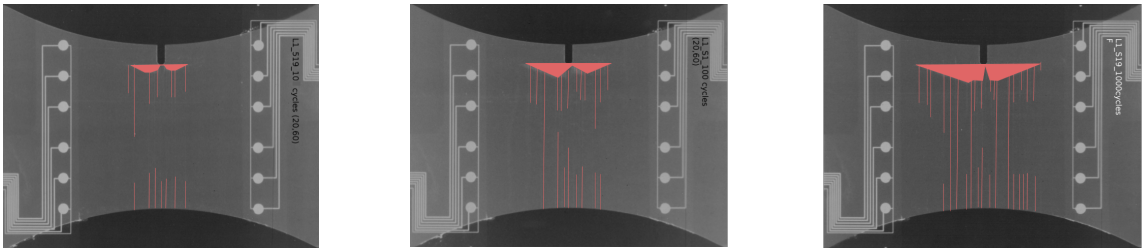

(a) After 10 cycles. (b) After 100 cycles. (c) After 1000 cycles.

Figure 4.12: images taken from L1S19.

4.5.1. IMRA: Initial results

For the results shown in this subsection, all the available data obtained from one measurement was used, i.e. signals from all 36 paths have been used for the reconstruction. Moreover, based on the observations made in Section 3.2, the full signal was used to calculate the DI. Lastly the shape factor, β, which affects the size of the probability ellipse was set to 1.05. This value followed from literature, but can be adjusted if necessary [43] [61]. The algorithm settings were as follows:

- Excitation frequency: $200kHz$.
- Number of paths: all 36 sensor paths.
- Signal: the entire signal has been used, i.e. including reflections.
- Shape factor: $\beta = 1.05$.

Figure 4.13 show the results of the image reconstruction algorithm as presented by [43] using $DI_{pearson}$. Figure 4.14 show the results for the same panels but instead using the signal energy, DI_{energy}. The images show the outlines of the dogbone specimen with the notch located at the upper edge. The colours indicate the magnitude of the pixel intensity, where red indicates a high and blue a low pixel intensity value. According to the algorithm, the higher the pixel intensity the higher the probability that this pixel contains damage relative to the other pixels.

From Figure 4.13 can be concluded that the algorithm is able to locate the delaminated area quite accurately. It can moreover be seen that while both the delamination and intralaminar cracks in the 90° direction become more severe for an increase in the number of fatigue cycles, the maximum value for the pixel intensity increases as well.

It can furthermore be seen from Figure 4.14 that using DI_{energy} indeed causes damage to be more concentrated towards the middle of the specimen as DI_{energy} is more sensitive to matrix cracks in this area and

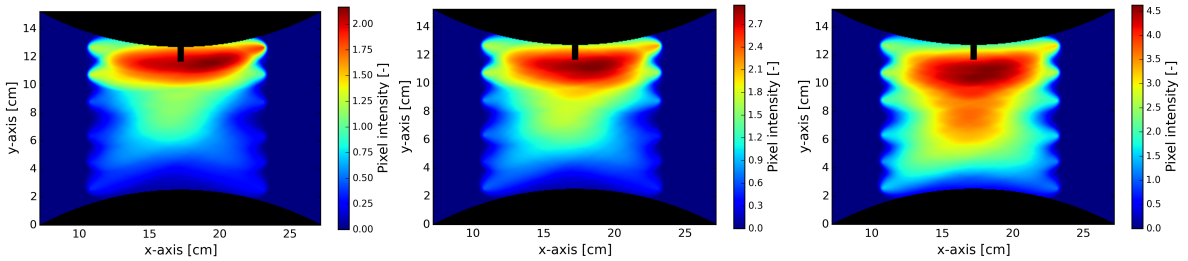

(a) Measured after 10 cycles. (b) Measured after 100 cycles. (c) Measured after 1000 cycles.

Figure 4.13: Reconstructed images using $DI_{pearson}$ and $f_c = 200kHz$.

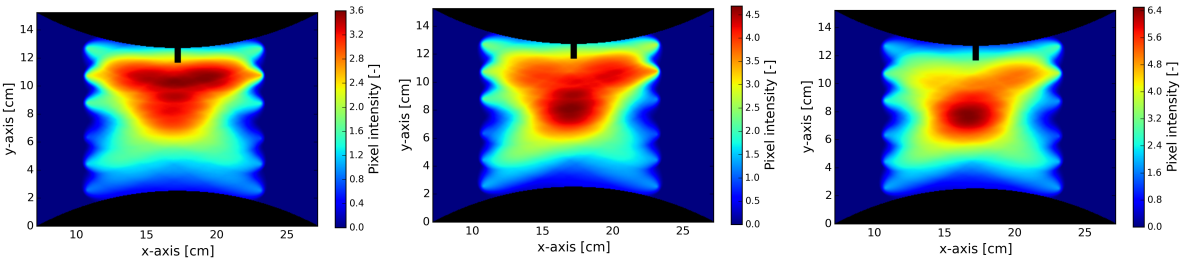

(a) Measured after 10 cycles. (b) Measured after 100 cycles. (c) Measured at 1000 cycles.

Figure 4.14: Reconstructed images using DI_{energy} and $f_c = 200kHz$.

therefore higher compared to $DI_{pearson}$ for these particular paths. This then results in higher pixel intensities for these areas as well.

In order to visualize the growth of damage, the images in Figures 4.13 & 4.14 should be made comparable. The first attempt was to fix the pixel intensity scale as shown in Figures 4.15 & 4.16. From these images becomes clear that the DI values and thus the pixel intensities indeed increase. However, at this moment the images still only show a probability distribution of pixels being damaged compared to the other pixels. Although a change of the one image to another could indicate damage growth, it is still difficult from these images alone to state if damage is really present. Moreover, if an MRO is to use the algorithm, damage that is below the ADL was described in Section 3.6 should not be considered. Therefore an appropriate threshold should be selected which will be evaluated in the next subsection.

4.5.2. IMRA: Threshold selection for NASA dataset

Damage detection, localisation and quantification can only be performed by setting a threshold to IMRA. A straightforward method of applying a threshold for damage detection could be to apply a threshold to the DI values. However, the author believes that the strength of this algorithm lies in combining the output of different sensor paths. Therefore, damage detection based on a single DI value was not favoured. Besides, also the damage severity estimation plays an important role in this research. Therefore, it was decided to look

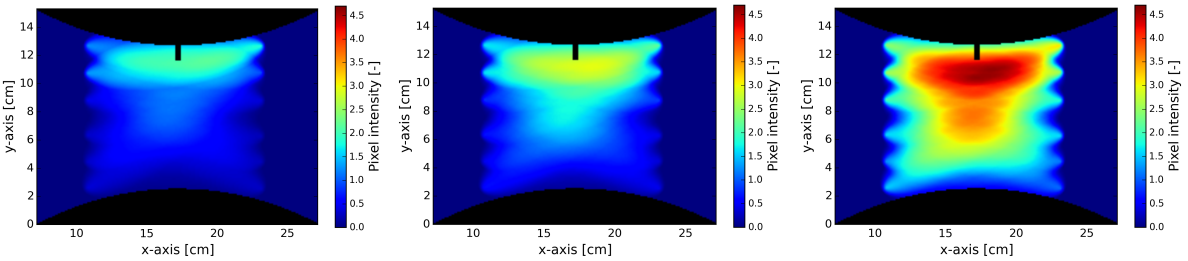

(a) Measured after 10 cycles. (b) Measured after 100 cycles. (c) Measured after 1000 cycles.

Figure 4.15: Reconstructed images using $DI_{pearson}$ and $f_c = 200kHz$ on a fixed colorscale.

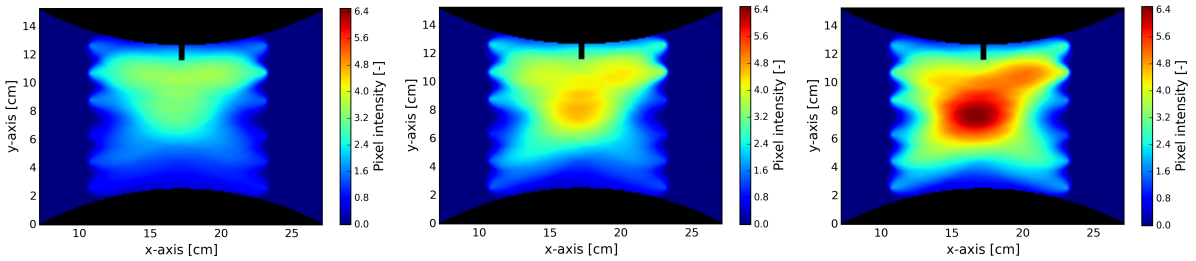

(a) Measured after 10 cycles. (b) Measured after 100 cycles. (c) Measured after 1000 cycles.

Figure 4.16: Reconstructed images using DI_{energy} and $f_c = 200kHz$ using a fixed colorscale.

into a threshold procedure which allows for the quantification of damage after which the damage size can be compared to the SRM. In this subsection the analysis of the threshold procedures shown in Section 3.7 are discussed.

Method 1: Setting a relative threshold to the pixel intensity.
Figure 4.17 shows the reconstructed images with a relative threshold applied to the pixel intensity values. V_{thres} was set to 0.92. This means that all pixel values $\geq 0.92 \cdot P_{max}$ were regarded to be damaged. To find the right value for V_{thres}, the length of the delamination estimated by the algorithm was compared to the delamination length determined from the X-ray images. V_{thres} was then adjusted to fit the damage size for a 100 fatigue cycles as the damage for this state was closest to the ADL prescribed by the SRM.

A disadvantage of this method is that it only takes the highest values of the pixel intensities into account. This means that images or damage states will be difficult to compare. Moreover, in order to monitor growth, pixels that were regarded damaged in a previous state should be regarded as damaged in subsequent states as well. From Figure 4.17 can be seen that this is not the case. While the delamination is located and sized after 10 cycles, it is not for 100 & 1000 cycles.

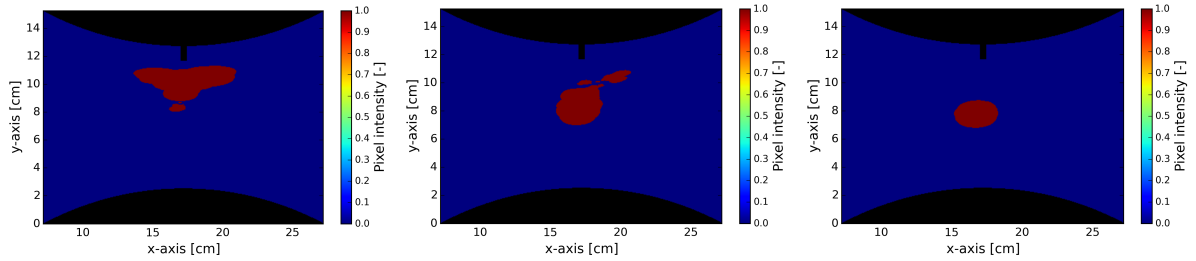

(a) Measured after 10 cycles. (b) Measured after 100 cycles. (c) Measured after 1000 cycles.

Figure 4.17: Applying a relative threshold to the pixel intensity values in Figure 4.14 using DI_{energy}, $f_c = 200kHz$ and $V_{thres} = 0.92$.

Method 2: Setting a value threshold to the pixel intensity.
The results from the second method using $DI_{pearson}$ are shown in Figure 4.18. As for the previous paragraph, the threshold value was selected based on 100 fatigue cycles and was set to $P_{thres} = 2.8$. The first thing that can be seen from Figure 4.18a, is that using this threshold, the structure is found to be healthy. Hence, this method allows for detection, localisation and size. However, the threshold must be chosen carefully and might even change per damage state and or frequency.

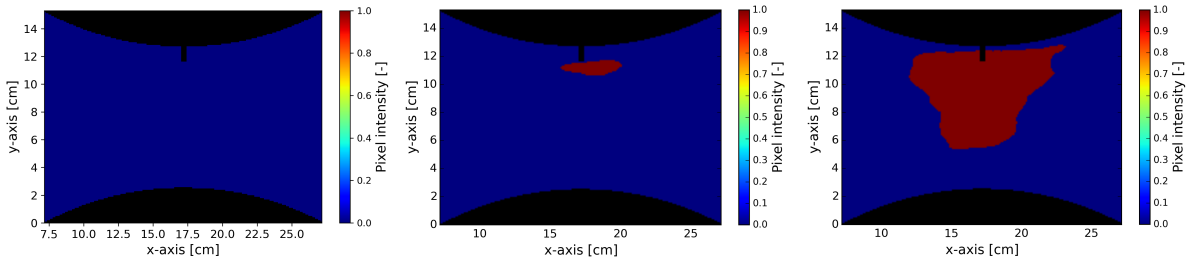

(a) Measured after 10 cycles. (b) Measured after 100 cycles. (c) Measured after 1000 cycles.

Figure 4.18: Applying a threshold to the pixel intensity values in Figure 4.13 using $DI_{pearson}$, $f_c = 200kHz$ and $P_{thres} = 2.8$.

There are several more objections towards this method. It was found that mainly for an increase in frequency, the reconstructed image tends to accumulate damage at the centre of the specimen. This can also be seen in Appendix D. Firstly, for an increase in frequency, waves are more sensitive to the intralaminar cracks so that for paths crossing the cracked areas higher DIs are found. Secondly, at the center of the plate more sensor paths overlap. This can be seen in Figure 4.19, which shows the reconstructed image excluding the DI values, so that it only shows a summation of the probability ellipses or PIW distributions.

With the data fusion process as described by Section 3.5, relatively speaking, damage at locations where more paths overlap will sooner cause a higher pixel intensity. As a result, the middle of the plate can show higher pixel intensity values compared to pixel location at the upper and lower edge of the specimen, while the damage severity is actually more severe at those locations.

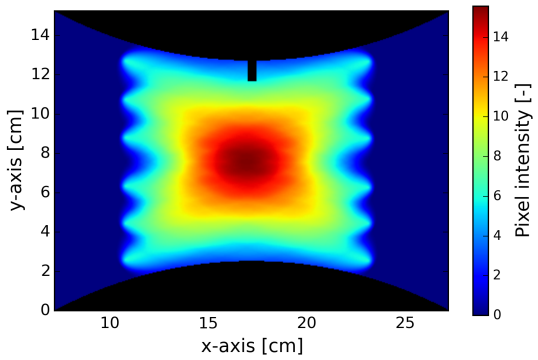

Figure 4.19: Summation of the PIW distributions.

Method 3: Setting a threshold to the DI and pixel intensity.
The first solution to overcome this bias was to put a threshold to the DI. A sensing path was only included in the image reconstruction if the DI exceeded a threshold. The threshold was selected by analysing the DIs of sensing paths directly propagating through the delamination in Figure 4.12b. Using this method all paths sensitive to cracks could be excluded which yielded better results regarding the delamination for DI_{energy}. It could also be seen that the localisation capability of the algorithm improved, because the influence of the ellipse's bias was decreased. This is shown in Figure 4.20.

However, by decreasing the number of paths that are used for the reconstruction, the algorithm also looses part of its accuracy because damage information is discarded. It can be seen in Figure 4.20b that the damage then tends to obtain the shape of an ellipse. This means that one will also need to define a minimum number of paths that is required to provide an output with sufficient accuracy. Moreover, using this threshold method, the number of paths that contribute to IMRA will be dependent on the central excitation frequency and damage state. As damage increases more paths might cross the threshold which makes it harder to monitor damage growth because the data used to reconstruct one damage state differs from the data used to create the next. This means that the images cannot easily be compared to each other. This is why the author proposes to use a threshold based on the change in pixel intensity.

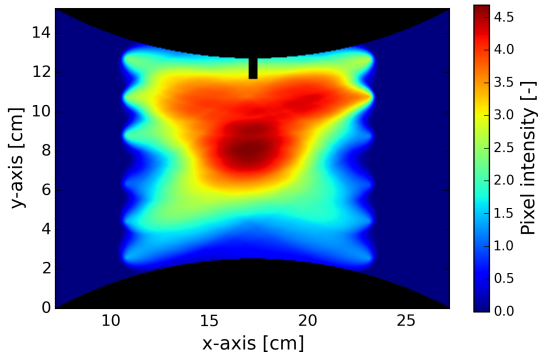

(a) Image reconstruction using all paths.

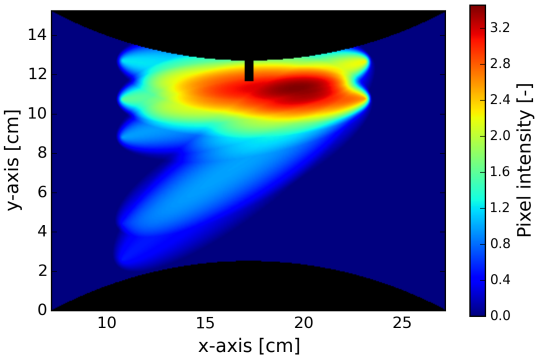

(b) Using the 10 paths for which $DI_{energy} \geq 0.4$.

Figure 4.20: Image reconstruction by setting a threshold to the DI for DI_{energy} after 100 cycles and $f_c = 200kHz$.

Method 4: Setting a threshold to the change in pixel intensity.
The thresholding method based on the change in the pixel intensity was described in Section 3.7. The outcome of this method is shown in Figures 4.21 & 4.22.

It becomes clear, especially for Figure 4.22 that using the change in pixel intensity has decreased the bias resulting from the overlapping paths at the center of the panel. Compare for example, the reconstructed image for 100 cycles in Figure 4.14b to Figure 4.22b. The pixel with the highest probability shifted upwards towards the delamination when constructed using the change in pixel intensity. Because of the difference in scaling it also becomes much easier to compare the different damage states.

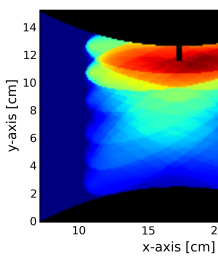

(a) Measured after 10 cycles.

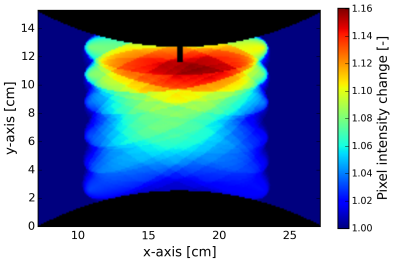

(b) Measured after 100 cycles.

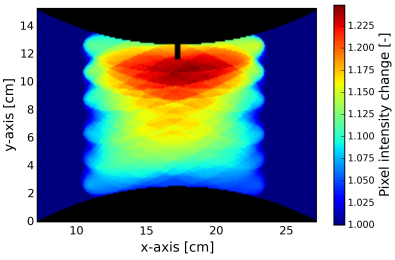

(c) Measured after 1000 cycles.

Figure 4.21: Reconstructed images based on the change in pixel intensity using $DI_{pearson}$ and $f_c = 200kHz$.

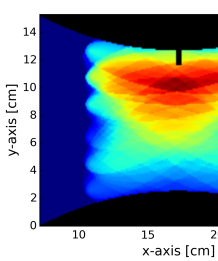

(a) Measured after 10 cycles.

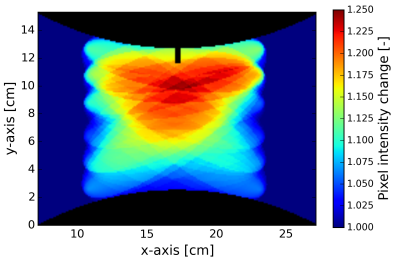

(b) Measured after 100 cycles.

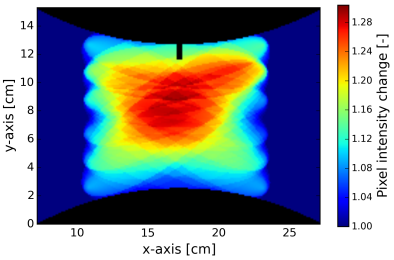

(c) Measured after 1000 cycles.

Figure 4.22: Reconstructed images based on the change in pixel intensity using DI_{energy} and $f_c = 200kHz$.

Similar to the images shown in Figures 4.13 & 4.14, a value threshold to the pixel change (instead of the pixel intensity) can be applied. Figure 4.23 & 4.24 show the images with an applied threshold $P_{thres} = 1.15$, for the pixel change based on PCC and $P_{thres} = 1.23$ for the pixel change based on signal energy.

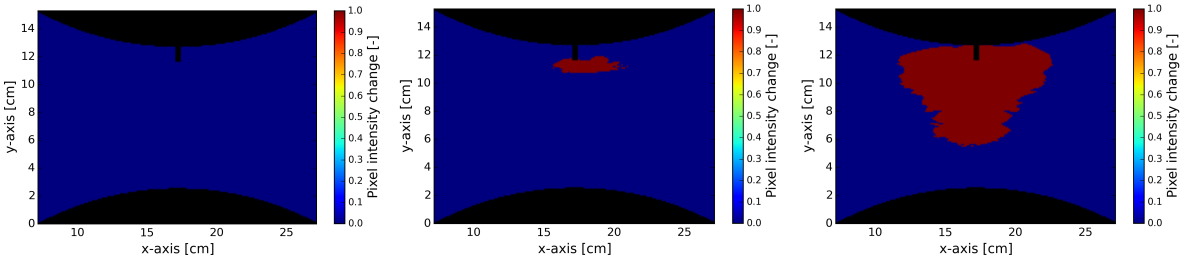

(a) Measured after 10 cycles. (b) Measured after 100 cycles. (c) Measured after 1000 cycles.

Figure 4.23: Reconstructed images based on pixel intensity change and a threshold using $DI_{pearson}$ and $f_c = 200kHz$.

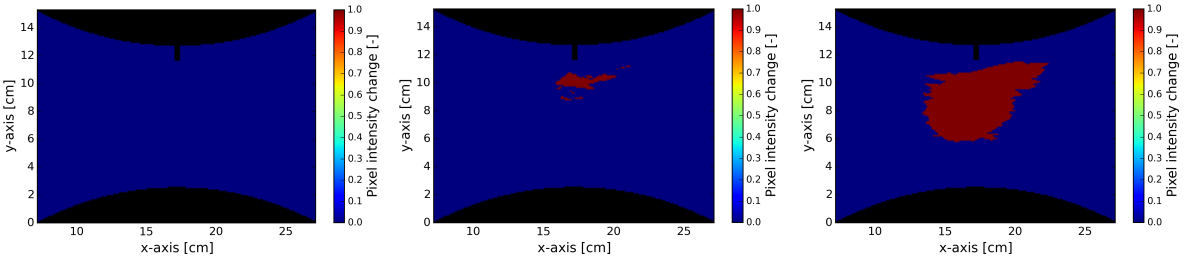

(a) Measured after 10 cycles. (b) Measured after 100 cycles. (c) Measured after 1000 cycles.

Figure 4.24: Reconstructed images based on the pixel intensity change and a threshold using DI_{energy} and $f_c = 200kHz$.

4.6. Conclusion

The aim of this chapter has been to analyse and evaluate the functioning of the image reconstruction algorithm presented in Chapter 3. For this purpose, a dataset from the NASA prognostics Data Repository was used. This dataset was originally used in other research to assess the estimation of delamination progression in CFRP panels. For this research, dataset L1S19 has been used to evaluate the behaviour of the algorithm by analysing the response of the DIs and data fusion process to different excitation frequencies, DI formulations and damage growth. This part of the dataset was found to offer the best possibilities to evaluate the algorithm for impact like damage and growth monitoring.

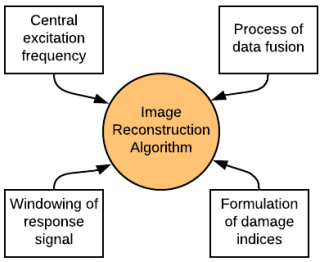

Figure 4.25: Factors that influence IMRA.

Four factors have been found to be of major influence to IMRA, which are shown in Figure 4.25. Firstly, it was concluded that windowing of signals as proposed in other research is not favoured by the author in combination with this algorithm. The boundaries of the window used to isolate one of the wave modes will greatly affect the DI. It makes a comparison between paths difficult and can cause paths to be considered more damaged than others while this should not be the case.

Secondly, overall the DIs showed that an increase in the central excitation frequency will lead to a more sensitive DI. In general, for sensing paths directly propagating through damage higher DIs were found for an increase in frequency. This can be explained by the fact that waves are easier affected by damage due to a

decrease in wavelength. The drawback of increasing the excitation frequency seems to be that paths which are more severely damaged than others, become less distinguishable. This then causes the algorithm's output to be less outspoken in its damage location as well.

Next to the excitation frequency, Section 4.4 also revealed that the formulation of the DI itself greatly affects the values found. Interestingly, it was found that $DI_{pearson}$ is more sensitive to delamination than it is to intralaminar cracks in the lower frequency range, while DI_{energy} did respond to these cracks. Two important conclusions could be drawn from these findings. Firstly, different types of damage interfere differently with Lamb wave signals. The danger in this lies with the fact that some types of damage might not be found using a particular DI as was shown by the signals in Figures 4.9a & 4.9b. Secondly, it was found that a delamination is able to cause a velocity change or mode conversion of Lamb waves when separating them at the beginning of a delamination and merging them at the end. The velocity change or mode conversion can be captured using the PCC as it results in a shift of one or more of the wave packages compared to the baseline signal.

Finally, it could be concluded from the previous section that the data fusion of the individual paths has an effect of the reconstructed image. A limitation to the algorithm or an SHM system in general is that the user must select a threshold, so that the output of the system exceeding the threshold will be an indication of a damage. It was found that by applying a relative threshold to the pixel intensity as commonly suggested in literature will not be suitable for the monitoring of damage growth because it only captures pixels with the highest pixel intensities and makes it unable to take previous damage states into account. It was also found that the algorithm tends to accumulate the probability of damage at locations where multiple sensing paths overlap. For this sensor network this happened at the center of the specimen. This means that a disturbance to the specimen at the center would be sooner identified as damage than a similar disturbance away from the center. To overcome this limitation or bias, the author suggested to slightly change the data fusion process by reviewing the change in pixel intensity instead. This showed that damage growth between the different damage states or fatigue cycles was better captured and easier compared. It also caused the delamination to be considered more severe compared to matrix cracks when using the DI_{energy} to construct the image.

5

Case Study: Boeing 787 skin panel

In Section 2.1 was concluded that the most encountered in-service damage for composite aircraft structures results from impact. Especially fuselage structures surrounding the door areas are prone to impact damage from ground operations. In addition, it was mentioned that there is little knowledge about the behaviour of composite structures exposed to impact and fatigue damage. With the 787 fleet of KLM growing it becomes imperative to develop accurate and fast monitoring systems for these structures.

The fuselage of a Boeing 787 consists of a carbon fiber composite structure with co-cured composite hat stiffeners and titanium ribs as presented in Figure 5.1. The manufacturing of the Boeing 787 comprises a relatively new method of construction which is called Automated Tape Laying (ATL). Using ATL a lower overall weight of the fuselage can be obtained by combining multiple one-piece sections. The disadvantage of this method comes with performing repairs as parts cannot be easily replaced. Moreover, inspections of the fuselage skin hidden inside the hat stiffeners are impossible using conventional NDT techniques. Thus, an SHM system capable of monitoring impact damage to the fuselage has the potential of improving maintenance of composite structures at KLM E&M.

This chapter therefore presents a case study for an SHM system using IMRA applied to a panel similar to the Boeing 787 fuselage skin. The purpose of this case study is twofold. Firstly, it aims to advance the understanding and functioning of IMRA in a more realistic context that it has been in the previous chapter and in literature in general. This is achieved by using larger test panels with a lay-up similar to parts of the 787 fuselage. It was attempted to create realistic impact damage instead of using Teflon inserts or drilling of holes to simulate damage. Secondly, the case study offered the possibility to obtain a better understanding of the practical challenges that accompany the application of SHM.

Two test campaigns have been performed during which Quasi-Static Indentation (QSI) tests have been used to create BVID. The first campaign functioned as a blind test. A panel was subjected to a QSI test with a predefined displacement of $5mm$. The algorithm was then used to evaluate the health state of the panel which was also validated using a C-scan and X-ray inspection. The second test campaign subjected another panel to a series of QSI tests until failure. The presence and increase in damage was validated using AE monitoring. The blind test was used to answer the question if damage can be detected without validation by a conventional NDT inspection. The second campaign allowed for an analysis of the damage growth.

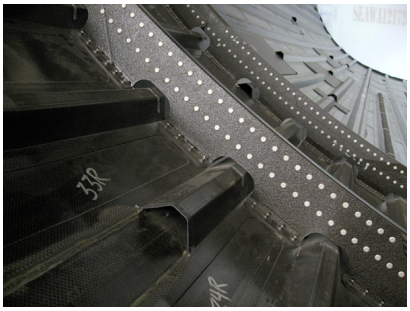

Figure 5.1: Cross-sections of the787 composite fuselage [70].

Although the output of IMRA might differ from other research, this chapter could be used as a guideline for other researchers to investigate the performance of their designed algorithms and SHM systems as it will not only cover IMRA, but also the practical considerations of an active SHM system in general.

The first section discusses the design and manufacturing of several test panels. Section 5.2 is devoted to the selection of PZT sensors. Hereafter the experimental set-up for sensor interrogation and QSI testing are presented in Section 5.3 and Section 5.4. In Section 5.5, the results from the image reconstruction are discussed. The chapter is concluded in Section 5.6.

5.1. Test panels: Design and manufacturing

As aforementioned, the panels used for this case study are based on the fuselage skin design of the Boeing 787. The design of the fuselage skin varies over its length and width to withstand different loading conditions. The thickness, especially at near cut-outs such as windows or doors is larger to provide higher load bearing capabilities and a higher resistance to impact [26]. For this case study it was, however decided to validate the algorithm using an unstiffened panel with a constant thickness and without any curvature. This simplified skin panel design was chosen to minimise the complexity of signal interpretation and damage that would occur after impact.

Four panels with dimensions, $500mmx500mm$ were manufactured using hand lay-up as it was not possible to use ATL. The manufacturing itself is presented in Appendix E. The panel specifications were deduced from an earlier study performed at KLM E&M by J. Tang Tian Le [65]. Together with composite experts, J. Tang Tian Le used parts of the SRM *"Fuselage-Section 43- Skin Identification"* to obtain the materials and ply orientation for the outer seven plies and identified the orientation of the remaining plies by creating a tapered edge on a real damaged fuselage panel [26]. This was necessary as the SRM provided by Boeing only provides the first seven layers which are also shown in Appendix E.

Table 5.1 presents the lay-up and materials used for manufacturing. It should be noted that in reality the first ply P1 is made out of a carbon pre-preg surfacer film which ensures the smooth aerodynamic surface of the aircraft. However this material is co-cured to the structure by the manufacturer and unavailable to KLM E&M. It was therefore decided to ignore this layer during manufacturing. It was furthermore decided to use the same plain weave (PW) material based on the innermost ply for both the inner- and outermost plies. Normally, the outermost plain weave also contains as copper mesh to offer better resistance against lightning. The inner plies are made of a unidirectional (UD) pre-preg.

Using the proposed quasi-isotropic lay-up a total thickness of $\approx 2mm$ was obtained. This is similar to the skin thickness of the lower half of fuselage susceptible to impact. Here the thickness ranges between $1.85-2.67mm$ [26].

Table 5.1: Test panel specifications based on the 787 fuselage skin.

Configuration Fuselage Panel			
Ply	**Orientation** [°]	**Fiber Type**	**Material**
P1	0/90	PW	N0004775 | Carbon fiber reinforced epoxy sheet as given in BMS 8-276 TYPE 40 CLASS 2A STYLE 6k-70PW-PB4 FORM 1 COMPOSITION LEVEL 2
P2	45	UD	N0004771 | Carbon fiber reinforced epoxy sheet as given in BMS 8-276 TYPE 35 CLASS 10- GRADE 190 FORM 3 COMPOSITION LEVEL 2
P3	90	UD	
P4	−45	UD	
P5	0	UD	
P6	0	UD	
P7	−45	UD	
P8	90	UD	
P9	45	UD	
P10	0/90	PW	N0004775 | Carbon fiber reinforced epoxy sheet as given in BMS 8-276 TYPE 40 CLASS 2A STYLE 6k-70PW-PB4 FORM 1 COMPOSITION LEVEL 2

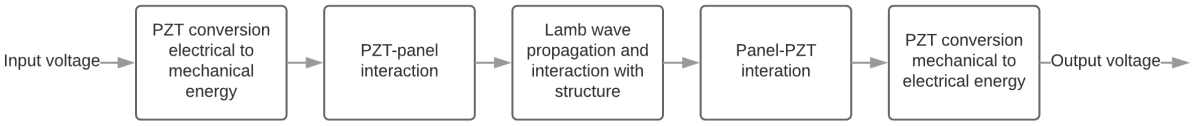

Figure 5.2: PZT- panel interaction.

5.2. Selection of PZT sensors

PZT sensors are available in a variety of sizes, shapes, and resonance frequencies. For this case study, it was decided to use circular PZT disc sensors to be able to excite omnidirectional guided waves. The performance of the PZT sensor is dependent on its resonance frequency and linearity, but also the PZT material, the geometry of the sensor and the structure's surface it is attached to. Also the quality of the bond or adhesive layer affects the interaction [71]. Together these properties determine how well a sensor transmits its mechanical energy to the structure during actuation and vice versa when functioning as a receiver. This principle is shown in Figure 5.2. For the working principle of the PZT the reader is referred back to Section 2.3.1.

Much research has been performed on the interaction between the PZT sensors and the structure [2, 71, 72]. The selection of the optimal PZT sensor is complicated due to the parameters mentioned above and was therefore assumed to be beyond the scope of this project. However, to the MRO industry availability of equipment and costs are key. Sensor selection was therefore performed based on availability, costs and industry best practice. Based on literature, discussions with researchers at the university, and availability at the manufacturer it was decided to use the following sensors: *PI Ceramic 000053020 with silver wrap-around electrodes*, of which a sample is shown in Figure 5.3a. Wrap-around electrodes are desirable so that the plus and minus electrodes can be reached from one side of the PZT sensor which simplifies the bonding procedure. The sensors were glued to the test panels as in Figure 5.3b using the procedure shown in Appendix F.

The sensors have the following specifications:

- PZT material: $PIC255$.
- PZT diameter: $6.5mm$.
- PZT thickness: $0.25mm$
- PZT resonance frequency (radial): $f_r = 308kHz$.

PI Ceramic's 255 is a soft PZT material well suited for sensing applications having a high curie temperature and high coupling factor for radial oscillation $k_p = 0.62$. Meaning that the PZT sensor is effective in the mechanical to electrical conversion and vice versa. The material is comparable to American Piezo Ceramics 850 used by [43, 73]. The diameter in combination with the PZT material determines the radial resonance frequency. When choosing a larger diameter bonding and soldering of the PZT sensors become easier, but the resonance frequency of the sensor decreases. This leaves a smaller frequency bandwidth for which the sensor shows linear behaviour.

On the other hand, the smaller the diameter of the sensor, the less efficient it will be at transmitting an ultrasonic wave and the less sensitive it will be to detection. When analysing the usage of PZT sensors in literature, no clear relationship was found between the central frequency used for Lamb wave excitation, the distance between sensors, and the thickness of the structure. This shows that other researchers either choose PZT sensors specifically selected for their experiment or commonly applied sensors as well.

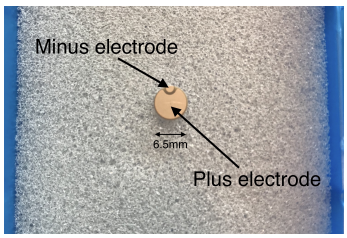

(a) PZT sensor as received from PI Ceramic.

(b) Bonded PZT sensor.

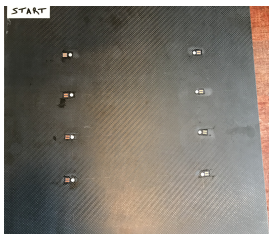

(c) Sensor network.

Figure 5.3: PZT sensor sample and sensor network.

5.3. Experimental set-up: Sensor interrogation

In this section the experimental set-up is discussed. The dataset is primarily obtained to function as an input to IMRA. However, it also allowed for the identification of possible hassles during an SHM inspection on an aircraft like structure. An Agilent 33500B series waveform generator was used to generate the excitation signals. The excitation signal used during the experiment was a Hanning-windowed sinusoidal tone burst. The signals were created in *Matlab* using a sampling frequency of $250MHz$ and a $10V$ peak-to-peak amplitude. Waves were generated for eight different central frequencies ranging from 100 to $450kHz$ in steps of $50kHz$. Figure 5.4. presents three of these signals. It can be seen that the duration of the input signal is depending on the number of cycles and central frequency. The excitation signals were stored as a $csv.$ file and uploaded to the waveform generator after which it was made sure that the waveform generator was set to the same sampling frequency as defined in *Matlab*. For every measurement, multiple bursts were sent through the panel. The signals were later on averaged to decrease the influence of random noise.

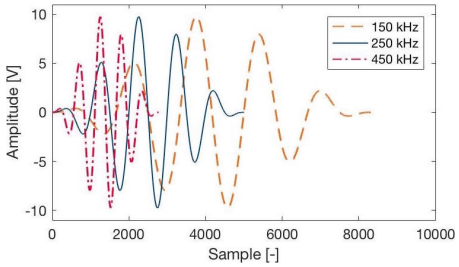

Figure 5.4: Sinusoidal tone burst generated in Matlab for $f_c = 150, 250$ & $450kHz$.

Sensor interrogation during for both test campaigns has taken place at the Delft Aerospace Structures & Materials Laboratory (DASML). The sensor layout used for each test panel is shown in Figure 5.5a. A rectangular eight sensor network was chosen because DASML disposes of an eight channel AE system which was used for signal recording. A rectangular network was chosen for several reasons. Firstly, when applying a similar SHM system to a real aircraft structure, several sensor networks might be put side by side. Regarding the installation and wiring of the sensors, this was believed to be more practical than for a circular network. Moreover, the algorithm was verified in the previous chapter using a rectangular sensor network. Using a similar layout during this case study allowed for a comparison. Finally, the clamping system used during damage creation had a rectangular cut-out. When wanting to keep the sensors located inside the cut-out to avoid damage to the sensors, a rectangular network achieved the largest inspection area. Finally for an MRO tests should preferably be performed on the largest inspection area as possible to motivate SHM for aircraft. Thus for practical reasons the rectangular network was preferred. However, it should be noted that a circular network might be better at distinguishing the shape and orientation of a defect due to the larger differences between the orientation of the sensing paths.

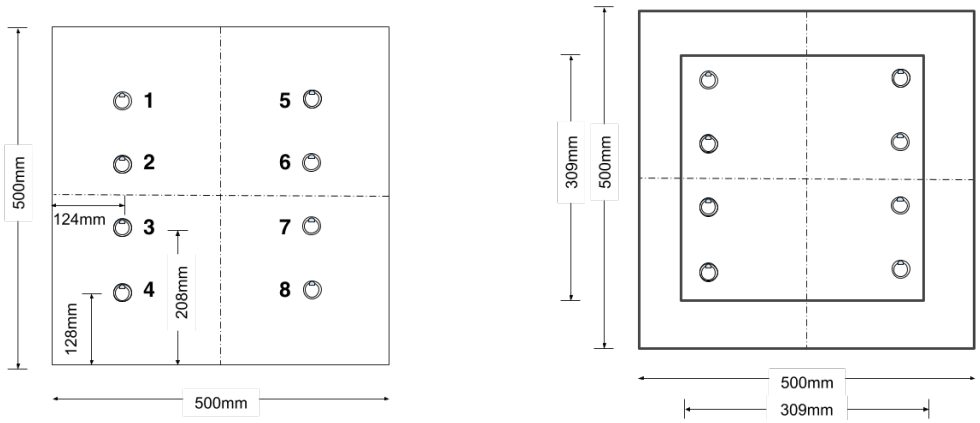

(a) Sensor array and sensor numbering.

(b) Dimension clamping system.

Figure 5.5: Dimensions of test panel.

A schematic overview of the equipment used to obtain the baseline as well as the damaged signals is shown in Figure 5.6. While one sensor was used as the actuator and connected to the wave generator, the other seven sensors were connected to the Vallen AEP4 pre-amplifiers and the Vallen AMSY-6 acoustic signal processor. The pre-amplifiers amplified the received signals using a gain of $34dB$. Amplification was performed to increase the signal-to-noise ratio while the signal attenuates due to cabling and disturbed by noise from the testing environment and equipment. For this reason it was made sure that the same cables were used for each measurement, i.e. for each sensor the same cable was used to connect the PZT sensor to the pre-amplifier and the same cable connected the amplifier to the signal processor. In order to avoid mistakes, the sensors, cables, and pre-amplifiers were labelled.

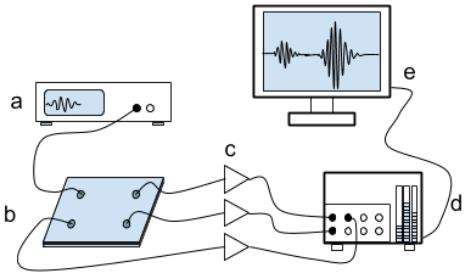

(a) Schematic set-up.

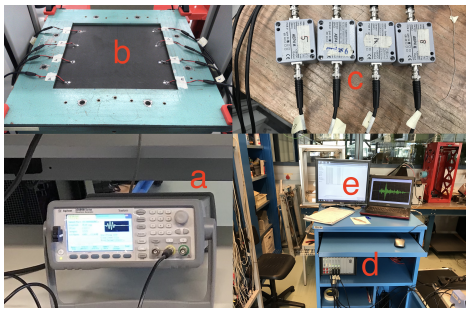

(b) Real time set-up.

Figure 5.6: Experimental set-up: *(a)* Agilent 33500B Series waveform generator, *(b)* panel with attached sensors, *(c)* pre-mplifiers with a gain of 34dB each, *(d)* Vallen AMSY-6 acoustic signal processor & *(e)* Laptop with Vallen Acquisition and Vallen Visual ^{TM} software.

5.3.1. Data acquisition

The Vallen AMSY-6 acoustic signal processor is normally used for AE monitoring. Therefore, the signal processor required the setting of a threshold to store the received signals after every excitation. This threshold causes the processor to save a signal when its amplitude exceeds a prescribed threshold. The moment a signal exceeds the threshold is called an event and the signal is saved with a predefined length. The number of pre-trigger samples is defined as the number of samples the signal processor stores prior to crossing the threshold.

The following settings were applied to the AMSY-6 processor:

- Threshold value: 40dB
- 400 pre-trigger samples
- Sampling rate or processor $10MHz$
- Transient recording (TR-recording) with a sampling rate $2MHz$ and 2048 samples per set or signal.

Because the system stores data after a threshold is crossed, it stores data in an order that is based on the ToA. This means that one has to make sure that the order of data storage, preferably in combination with the receiving channels, is saved by the acquisition system to connect the received signal for each channel to the correct sensor for signal processing. Sometimes the system can save erroneous signals because a disturbance from the testing environment causes the threshold to be exceeded. An additional threshold was applied during signal processing to overcome this problem. A flow chart of the applied signal processing is shown in Appendix G. A separate data file was created for every measurement. This means that the data was stored in a file containing the signals from seven receivers excited by one actuator at one of the chosen excitation frequencies, e.g. *'damA_X_F_250.tradb'*. Here *A* is the actuator, X indicates the damage state and F the excitation frequency. The signals were stored using a sampling frequency of $2MHz$.

5.4. Experimental set-up: Quasi-static indentation testing

In this section the experimental method for the QSI tests is presented. Various researchers have reported a similarity between damage resulting from QSI and LVI tests [74–76]. This similarity is explained further in the first subsection. The second subjection discusses the set-up used for the blind test. A second panel was subjected to a series of QSI tests until failure which is explained in the final subjection.

5.4.1. Creating BVID using QSI

Understanding the progression of impact damage is of interest to many researchers so that the impact resistance of composites can be improved. As a result, much research has focussed on composite behaviour under QSI because it allows for a step-by-step investigation of the damage progression [75].

In general several phases of damage can be defined for a panel undergoing QSI. These phases are argued to be similar for a panel subjected to LVI. Damage initiates in the from of intralaminar matrix cracks in Mode I. By increasing the displacement further the DTL can be reached after which delaminations spring from the tip of the intralaminar matrix cracks where high stress concentrations occur. The delaminations cause a reduction in the stiffness of the panel which is why often a sudden load drop can be seen in the force-displacement history [76, 77]. It was found that for many laminates the DTL is similar for indentation and impact. The delaminations can continue to grow until a load is reached for which the delamination growth becomes stable. Ultimately, the fibers will be unable to carry the remaining loads which causes them to break.

Lee and Aoki demonstrated that the typical pine tree damage shape as previously shown in 2.3a was also found after indentation tests [74, 75]. The bending and in-plane stresses cause tensile strains on the backside of the indented laminate which is why the majority of the cracks are found on the opposite side of the indenter after impact as well as indentation.

However, one should keep in mind that damage after indentation and impact is not exactly the same when considering the full picture. Although research as demonstrated that the damage mechanisms can be compared, it was shown for example by Spronk et al. that for a carbon-epoxy composite, the DTL can also be underestimated using a QSI test [78]. It was shown that the delaminated area using a QSI test are overestimated and causes little damage close to the impacted surface compared to LVI. It also presented a reduction in the number matrix cracks. While this should be kept in mind during the analysis, the advantage of QSI remains that damage can be created in a controlled manner using several loading steps.

5.4.2. QSI test campaign 1: A blind test

The first experiment consisted out of a blind test, by which the author means that damage initiation and damage growth were not measured during the QSI test itself but were evaluated afterwards. The experimental set-up for this QSI test can be seen in Figure 5.7a.

During the indentation test, the panel was clamped inside a clamping system which was shown in Figure 5.5b. Normally, such a fixture requires pins to tighten the panel inside. However, this requires holes to be drilled through the panel, which was firstly not favoured for signal processing and secondly, would also create areas of high stress concentrations and therefore areas prone to damage initiation outside of the inspection area.

The indentation force was applied to the panel using a semi-spherical indenter of $37mm$ in diameter, under a displacement control rate of $2mm/min$ using a tensile/compression *Zwick 20kN LF7M10* machine shown in 5.7a . The applied load and vertical displacement of the working platform were continuously recorded during all tests by the machine itself until a displacement of $5mm$ was reached. Prior the this test, it was unknown if damage would be initiated. The location of the indenter is shown in Figure 5.8a. This was also the area of interest in terms of the expected damage location.

The first attempt to identify damage after the QSI test was by performing an A-scan inspection of the area of interest. Therefore, an A-scan was also performed prior to the test. Photographs were taken during the A-scan and are shown in Appendix H. An A-scan displays the amplitude of the received echo or reflected signals of an ultrasonic wave along the thickness of the inspected material. The probe functions both as actuator and as the receiver in a pulse-echo configuration.

Prior to the QSI test, the baseline signals were recorded. The panel was placed onto four small blocks of foam and interrogated as was described in the previous section. The force-displacement curve of this test is shown in Figure 5.7b. An image of the second A-scan is shown in Appendix H as well. For the healthy panel, three intensity peaks were visible. The first peak follows from the ultrasonic wave travelling into the structure which causes part of the wave to be reflected due to the difference in acoustic impedance. The third peak

(a) QSI set-up during blind test.

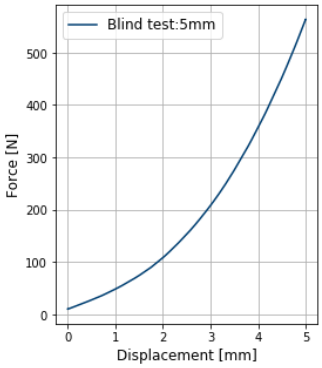

(b) Force-displacement curve for blind QSI test.

Figure 5.7

around the $2mm$ presents the wave reflected from the material's back edge. From the A-scan after the blind test can be seen that the peak representing the back edge has disappeared. This could be an indication of a delamination. On the other hand, when a delamination is present an additional peak should appear along the thickness as part of the wave is reflected by the interface of the delamination. This was not shown on the A-scan.

In both scans, the second peak should also not be present in case of a perfect laminate. The second peak indicates either a delamination present in both the healthy and damaged structure or it can be a sign of bad coupling between the probe and the surface of the inspected panel. For these reasons, the author believes that making use of the A-scan to confirm the presence of damage after the blind test is debatable and should not be the preferred method of validation for this experiment.

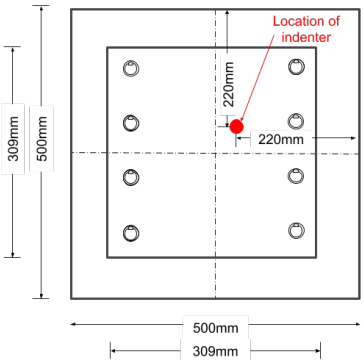

(a) Test campaign 1

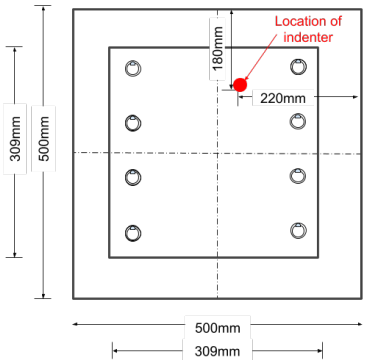

(b) Test campaign 2

Figure 5.8: Location of the indenter.

5.4.3. QSI test campaign 2: A series of tests using AE monitoring

From the blind test described in the previous subsection was seen that an A-scan cannot always provide clear validation for damage creation inside a panel with unknown material properties. Therefore, during the second test campaign another panel was subjected to a series of QSI tests where damage initiation and damage growth were validated using the force-displacement curve and the use of AE monitoring. The principles of AE have already been shortly explained in Section 2.3.2. Damage initiation and damage propagation cause a release of energy in the form of elastic transient wave which can be captured by an AE sensor. Through an analysis of the measured signals damage might be detection, located, and identified.

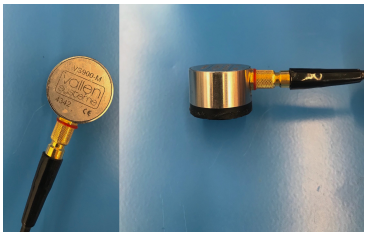

(a) Vallen system V900-M sensor.

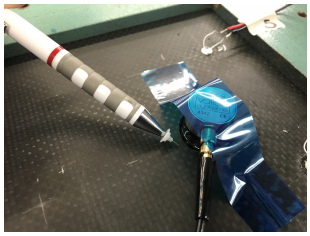

(b) Pencil lead break.

Figure 5.9: AE equipment.

During the QSI test two broadband Vallen Systeme VS900-M AE sensors were attached to the panel using Sonotech Ultrasonic Couplant and kept in place using Airtech pressure tape. One of the sensors is shown in Figure 5.9a. The gain of the Vallen preamplifiers was 34dB and the threshold for receiving signals was set to 40dB. The sampling rate of the AE processor was set to $10MHz$. Adequate coupling of the sensors to the panel's surface was ensured by performing several pencil lead breaks as shown in Figure 5.9b. A signal peak amplitude of 95dB for a lead break close to the sensor was assumed sufficient.

In total a series of six indentation tests were performed. The *Zwick 10kN LF7M10* machine was set to end the test at a predefined displacement (note that for this test the Zwick 10kN instead of the 20kN tensile test machine has been used, but this should not cause any differences). An overview of the AE set-up during the QSI is shown in Figure 5.10.

The test panel was first placed inside the clamping system and the location of the indenter is shown in Figure 5.8b. In contrary to the blind test it was decided to leave the test panel inside the clamping system during sensor interrogation in order to take consistent measurements without the need to dis- and reconnect the sensors to the rest of the cabling. This also meant that the panel was to be put inside during the acquisition of the baseline signals to avoid differences in reflections or wave behaviour. Clamping of the system adds extra geometric discontinuities to the tested panel which results in additional reflections. It might also affect the stiffness of the panel, thereby changing the wave velocity.

A step-by-step loading process was used to perform the QSI tests. The loading spectrum thus followed a saw tooth shape as in Figure 5.11. The displacement was increased until either a load drop in the force-displacement curve or a substantial increase in the number of AE events was observed. Hereafter, the panel was unloaded and the damage signals were recorded for that particular damage state, which have been denoted scenario 1 to 6. The maximum displacement and measured load are shown in Table 5.4.3.

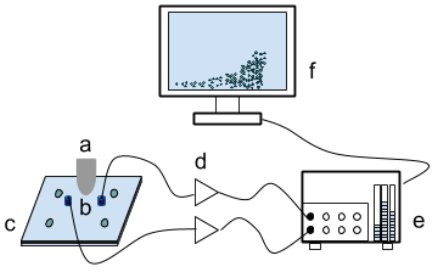

(a) Schematic set-up.

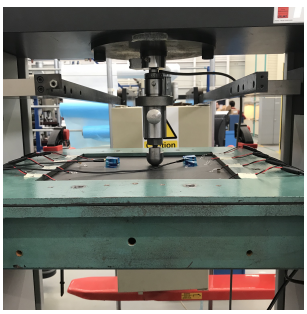

(b) Real time set-up.

Figure 5.10: Experimental set-up: *(a)* Agilent 33500B Series waveform generator, *(b)* Vallen Systeme V900-M sensors *(c)* panel with attached sensors, *(d)* Vallen pre-mplifiers with a gain of 34dB each, *(e)* Vallen AMSY-6 acoustic signal processor & *(f)* Laptop with Vallen Acquisition and Vallen Visual ^{TM} software.

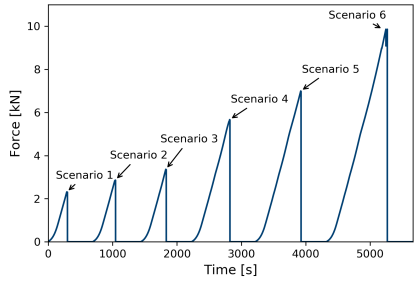

Figure 5.11: Loading spectrum.

Table 5.2: Maximum displacement and load.

Damage scenario	**Displacement** $[mm]$	**Force** $[kN$
Scenario 1	8.4	2.31
Scenario 2	9.1	2.86
Scenario 3	9.7	3.36
Scenario 4	12.3	5.67
Scenario 5	13.4	6.99
Scenario 6	15.5	9.86

In Figure 5.12a the force-displacement curves for damage scenarios 2 and 3 are presented. From the figure can be seen that a load drop occurred during the indentation test of scenario 2. During the third indentation test, the decision to quit the test was not supported by a load drop but by a substantial increase in the number of AE activities as can be seen in Figure 5.12b. In this figure the AE activity inside the specimen as a result of damage progression is illustrated. The number of AE events and their peak amplitudes are shown against the displacement of the working platform. The vertical line shows the maximum displacement reached during the previous indentation test. Figure 5.12b shows the number of events drastically increases after the vertical line. In literature this is explained by the fact that damage progress mainly after the previous maximum endured force is exceeded. However, in Figure 5.12b also shows AE activity before the $2.86kN$ was reached. This might indicate that damage is already quite severe, causing damage to grow at lower force levels as well. The force-displacement curves and AE activity of the other damage scenarios are shown in Appendix I.

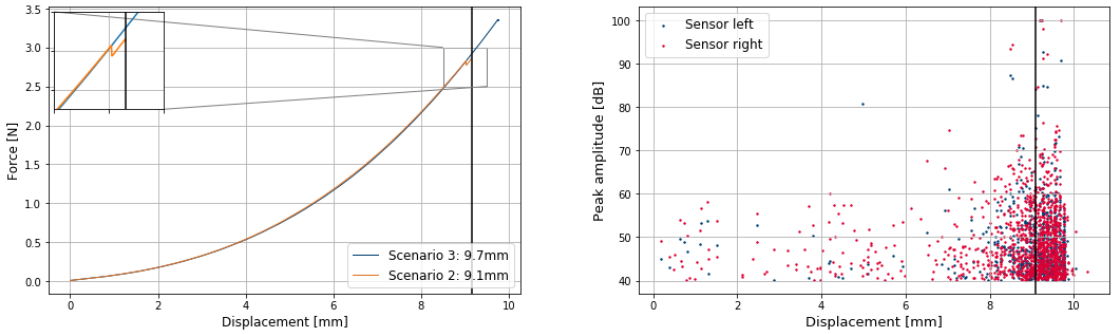

(a) Scenario 2 & 3: Force-displacement curves

(b) Scenario 3: Acoustic emission activity

Figure 5.12: Force-displacement curves for scenario 2 & 3 and AE activity for scenario 3.

5.5. Results

In this section, the results of IMRA using the data acquired from both test campaigns are presented. Prior to discussing the results, the sensor network and corresponding path numbers are shortly stated. The sensing paths corresponding to each of the actuator-receiver combination assigned for the image reconstruction are given in Table 5.3.

In contrast to the NASA dataset analysed in the previous chapter, it was decided to record signals propagating in both directions, e.g. signals were recorded from actuator 3 to receiver 7 and the vice versa. In theory, the reciprocity principle holds for Lamb waves travelling between sensors 3 & 7. By the reciprocity principle is meant that a reversal symmetry of the wave field exists between the two sensors. However, the author expects that damage might introduce non-linearities in the material which causes this principle to become invalid. This is also supported by the research of Huang, Zeng and Lin, who investigated the usage of a DI relying on a difference in response signals only [79]. Using signals propagating in both directions, the author expects that the algorithm will be better at distinguishing damaged from undamaged pixels. The downside of recording signals in both ways is an increase in the required data storage and computational effort during signal processing. However, for this relatively small experimental set-up, this was not a problem.

The first subsection, Subsection 5.5.1 covers the result following from the image reconstruction after the blind QSI test. Subsection 5.5.2 presents the results following from the second panel subjected to a series of QSI tests until failure. The final subsection discusses the last performed QSI test for damage scenario 6 after which one of the sensors was broken. This allowed for an analysis of the algorithms performance in combination with sensor failure.

Table 5.3: Path numbers corresponding to the sensor configuration in Figure 5.5a.

Path	Actuator	Receiver	Path	Actuator	Receiver	Path	Actuator	Receiver
0	1	5	**12**	4	5	**24**	7	1
1	1	6	**13**	4	6	**25**	7	2
2	1	7	**14**	4	7	**26**	7	3
3	1	8	**15**	4	8	**27**	7	4
4	2	5	**16**	5	1	**28**	8	1
5	2	6	**17**	5	2	**29**	8	2
6	2	7	**18**	5	3	**30**	8	3
7	2	8	**19**	5	4	**31**	8	4
8	3	5	**20**	6	1			
9	3	6	**21**	6	2			
10	3	7	**22**	6	3			
11	3	8	**23**	6	4			

5.5.1. Results for test campaign 1: A blind test

In a similar manner to the method described in Chapter 3 and analysed in Chapter 4, image reconstruction was performed for the panel subjected to the blind indentation test discussed in Section 5.4.2.

Figure 5.13 shows the reconstructed image based on $DI_{pearson}$ and DI_{energy} using an excitation frequency of $f_c = 150kHz$, where the black circle indicates the location of the indenter during the QSI test at $x = 28cm$ & $y = 28cm$. From these figures can be seen that the algorithm shows its highest pixel intensity quite close to the location of the indenter. The absolute distance between the indenter and the highest pixel intensity for $DI_{pearson}$ in Figure 5.13a is $3.12cm$ and for DI_{energy} in Figure 5.13b is $4.24cm$.

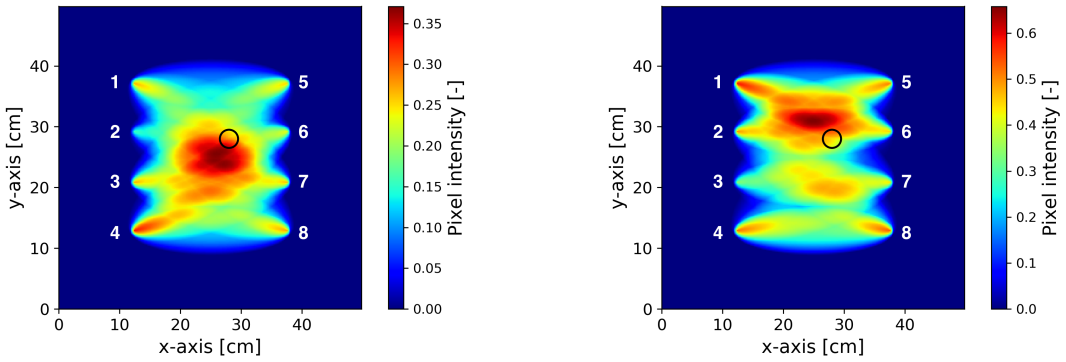

(a) Reconstruction using $DI_{pearson}$.

(b) Reconstruction using DI_{energy}.

Figure 5.13: Image reconstruction for the performed blind test for at $f_c = 150kHz$.

The calculated values for the DIs used to construct the images above are shown in Figure 5.14. For both figures can be concluded that the values are quite low, but still show a distinction between the different paths. Especially the DI_{energy} seems to make a distinction between paths close to the indenter and the remaining paths. As was seen for the NASA specimen analysed in the previous chapter, the values for the DIs are dependent on the central frequency of the excitation signal. The influence of f_c on the results of this case study is further analysed in the next subsection. For the blind test, the algorithm showed the best results in terms of damage localization for $f_c = 150kHz$.

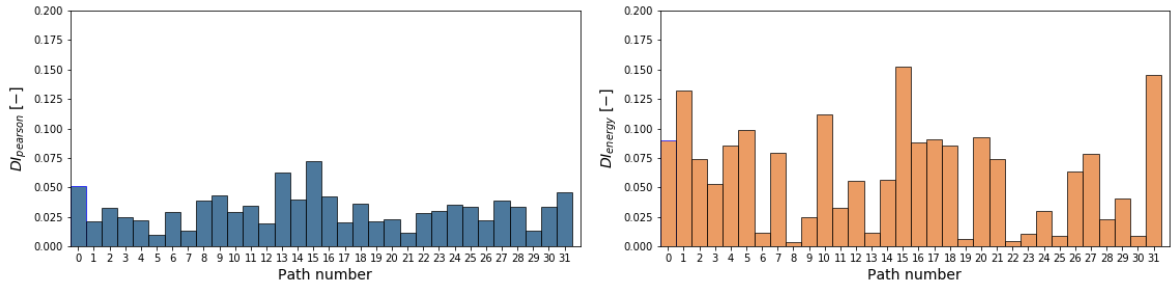

(a) Pearson DI.

(b) Energy DI.

Figure 5.14: DIs per path for $f_c = 150kHz$ for the blind test.

In case damage is induced to the panel during the QSI test, damage is expected surrounding the location of the indenter due to the presence of bending and shear stresses during indentation. Paths close to this area should thus show the first indications of damage. Examples of two paths for which a higher DI should be seen are path 18 actuator 5 & receiver 3, and path 21, actuator 6 & receiver 2. The received signals of these paths, measured at $f_c = 150kHz$ are therefore shown in Figure 5.15. The figure shows that the direct wave packages of paths 18 and 21 are not affected by damage. Figure 5.15a does show a disturbance for the wave packages around $170\mu s$ which are likely to be waves reflected from the edge of the panel and propagate through the area of the indenter. The disturbance for the received signal in Figure 5.15b seems less severe. However, the DI_{energy} for the paths are still quite similar, 0.086 versus 0.074 for paths 18 and 21. The $DI_{pearson}$ shows a larger difference, 0.036 versus 0.012 respectively.

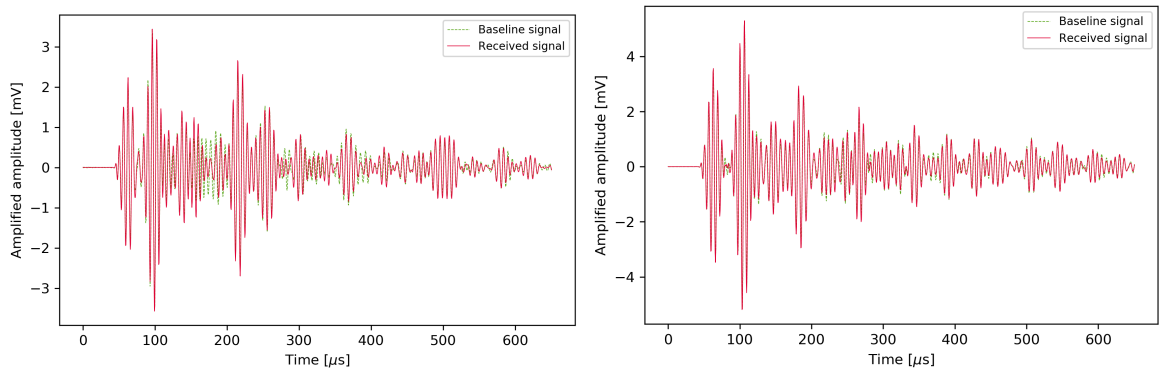

(a) Path 18, actuator 5 & receiver 2 for $f_c = 150kHz$.

(b) Path 21, actuator 6 & receiver 3 for $f_c = 150kHz$.

Figure 5.15: Response signals for paths 18 and 21 after blind indentation test.

Taking another look at Figure 5.14b shows the highest DI_{energy} for paths 15 & 31, between sensors 4 & 8. This unexpected since these paths do not directly propagate through the location of the indenter. The corresponding signals are shown in Figure 5.16 of which can be seen that the higher DI values are cause by reflections as well. From these signals can also be seen that indeed the signals show reciprocity but only up to a certain extend as the values for the DIs do slightly differ, DI_{energy} for path 15 and path 31 equal 0.152 & 0.145 and for $DI_{pearson}$, 0.073 & 0.046. While the highest values for the DI are found for sensors 4 & 8, which are located at the lower half of the panel, the algorithm still succeeded at locating the highest probability of damage very close to the indenter. This then shows the advantages of combining the output of multiple sensor paths and the power of the algorithm to locate damage through data fusion.

It can moreover be seen that the disturbance is caused more by an decrease in amplitude than by a signal shift. From a material point of view, it can be concluded from Section 5.4.1 that damage from indentation starts with intralaminar matrix cracks. Moreover, based on the observations in Section 4.4.3, it could be argued that intralaminar matrix cracks cause attenuation while a delamination would cause a signal shift. Thus when damage is indeed initiated during this test, amplitude changes are initially more expected due to cracks than signals shifts are due to a delamination. These findings might be used to explain why the overall values found for the $DI_{pearson}$ in Figure 5.14a are lower than for the DI_{energy}.

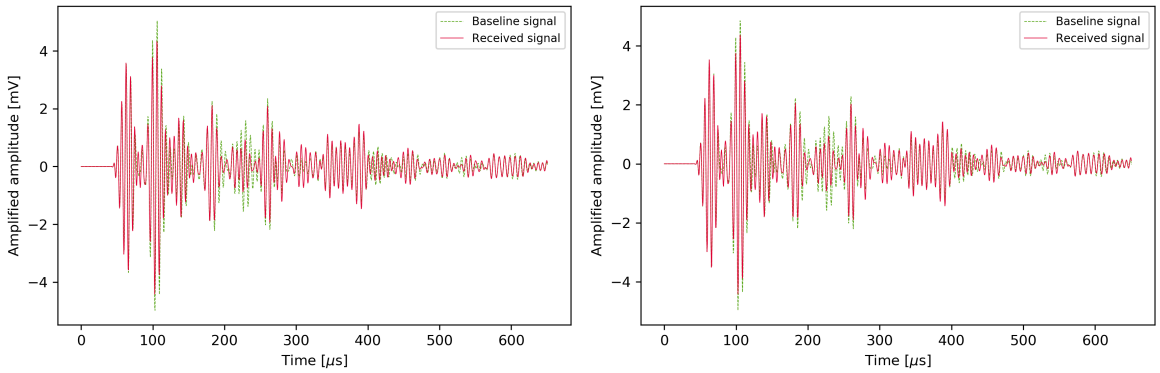

(a) Path 15, actuator 4 & receiver 8 for $f_c = 150kHz$.

(b) Path 31, actuator 8 & receiver 4 for $f_c = 150kHz$.

Figure 5.16: Response signals for paths 15 and 31 after blind indentation test.

Lastly, while the highest values for the DI are found for sensors 4 & 8, which are located at the lower half of the panel, the algorithm still succeeded at locating the highest probability of damage very close to the indenter. This then shows the advantages of combining the output of multiple sensor paths and the power of the algorithm to locate damage through data fusion.

From these figures alone, it is however, still not possible to state if damage is present as it is not known what magnitude of the DI could be considered to have been caused by damage and what values could also be resulting from noise or changes to the testing environment. For example, after the baseline signals were recorded, cabling was removed, The panel was placed inside the clamping system and the QSI test was performed. After the test, all cables were re-soldered to the sensors and reconnected to the equipment for the interrogation of the damaged state signals. In hindsight, this might have caused changes to the response signals. For this reason, the cabling was not disconnected during the QSI tests validated with acoustic emission discussed in the next section.

To determine the real damage state of the panel and validate the algorithm's output it was decided to subject the panel to two other NDT inspections. Firstly, an X-ray image was taken at KLM E&M of which a picture is shown in Appendix H. From the X-ray image no indications of damage could be seen. This means that damage might either not be present or the X-ray equipment is not capable of detecting the type of damage induced to the panel. In the end, it could not be stated if damage was present after reviewing the X-ray.

Because X-ray inspection turned out to be inconclusive an additional C-scan inspection was also performed. The set-up of the C-scan and its results are shown in Appendix H. To evaluate the panels after manufacturing, a C-scan was also performed prior to the blind test. However, also the C-scan inspections did not show any difference between the healthy and supposedly damaged panel.

Overall this leads to the following conclusions with respect to the blind test. Without making a comparison between the output of the algorithm and another NDT technique it could not be stated if BVID is present inside the panel. The disturbances found by the algorithm were very small and so it might be argued that these are not caused by damage but rather by noise or changes in the experimental environment, e.g. differences in cabling. On the other hand, it was also found that damage from indentation is likely to start from intralaminar matrix cracks which are difficult to detect using a C-scan or X-ray inspection. Thus, it is possible that the algorithm was capable of detecting damage at an earlier stage which would proof the benefit of earlier damage detection using an SHM system.

5.5.2. Results for test campaign 2: A series of tests using AE monitoring

In this subsection the results for the series of QSI tests are presented. As for the panel discussed in the previous subsection, a C-scan inspection was performed prior to the recording of the baseline signals. Both a C-scan and X-ray inspection were also performed after the last QSI test corresponding to scenario 6. The results are shown in Appendix J.

Unfortunately one of the sensors, sensor 3, failed before the response signals of the last QSI test, scenario 6, were recorded. For this reason, the results of scenarios 1-5 are presented in this subsection after which scenario 6 and the influence of this sensor failing will be discussed in the next subsection. Because of the incomplete dataset for scenario 6 no real comparison could be made between the result of the C-scan and the output of the algorithm.

However, from the C-scan could be seen that there was only one area containing damage. This was at the location of indentation, $x = 28cm$ & $y = 32cm$ so that the outcome could be evaluated for localization. Moreover, the damage after scenario 6 was found to have an elliptical shape with length $2.5cm$ and width $2cm$. Therefore, the results in this subsection will be analysed and a threshold will be applied based on the location and size of this damage. In order to evaluate if the algorithm was able to capture damage growth the pixel intensity at this area should increase for every QSI test as it was shown by the AE measurements that damage progressed.

In contrary to the C-scan no damage was found for scenario 6 using the X-ray inspection. This was interesting as cracks could even be detected visually at the location of the indenter on the bottom side of the panel. An image of the cracks is shown in Appendix J as well.

The reconstructed images for scenarios 1 to 5 are shown for an excitation frequency of $150kHz$ in Figure 5.17 and Figure 5.18. The absolute errors between the location of the indenter and the highest pixel intensity are shown in Tables 5.4 & 5.5. The table shows that especially for DI_{energy}, the algorithm can be used to locate damage well from Scenario 2 onwards. The areas very close to the sensors, i.e. close to the focal points of the ellipse were not considered when determining the maximum distance. As can be seen from Figure 5.18d high pixel intensities are sometimes found close to the sensors due the high number of paths overlapping at these locations. This effect can be reduced by considering the change in pixel intensity as was shown in the previous chapter. The reconstructed images based on the change in pixel intensity are shown in Appendix K.

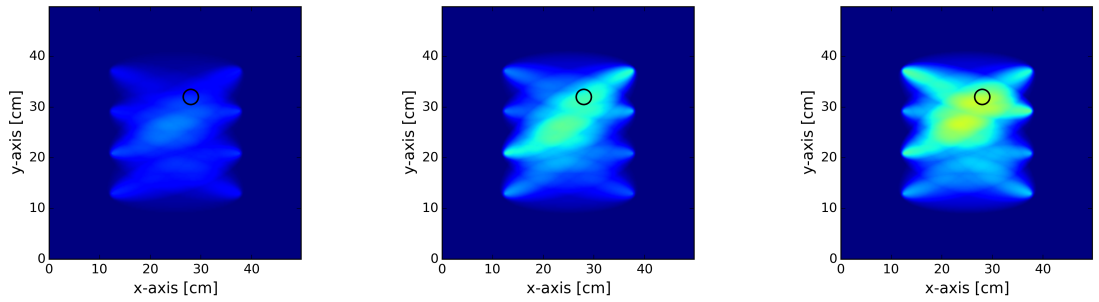

(a) Scenario 1: Displacement 8.4mm. (b) Scenario 2: Displacement 9.1mm. (c) Scenario 3: Displacement 9.7mm.

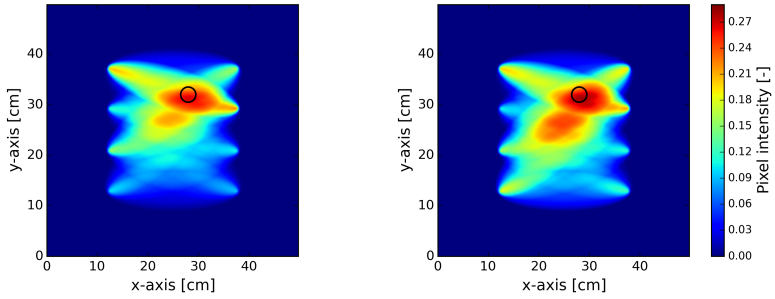

(d) Scenario 4: Displacement 12.3mm. (e) Scenario 5: Displacement 13.4mm.

Figure 5.17: Image reconstruction: Scenario 1-5 for $f_c = 150kHz$ and $DI_{pearson}$.

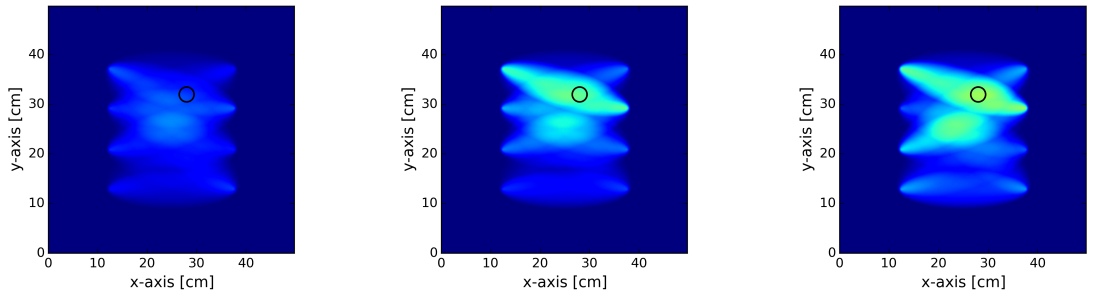

(a) Scenario 1: Displacement 8.4mm. (b) Scenario 2: Displacement 9.1mm. (c) Scenario 3: Displacement 9.7mm.

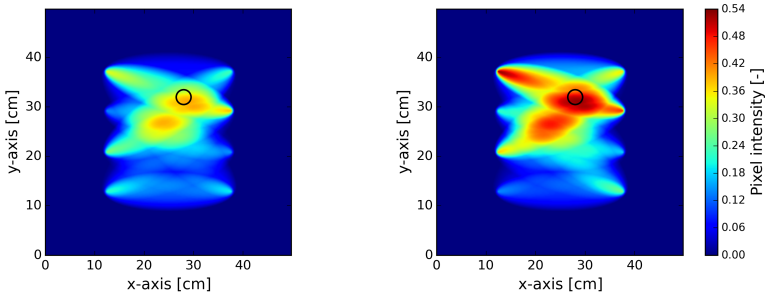

(d) Scenario 4: Displacement 12.3mm. (e) Scenario 5: Displacement 13.4mm.

Figure 5.18: Image reconstruction: Scenario 1-5 for $f_c = 150kHz$ and DI_{energy}.

Table 5.4: Absolute error using $DI_{pearson}$ at $f_c = 150kHz$.

Scenario	x [cm]	y [cm]	error [cm]
Scenario 1	23.8	26.4	7.00
Scenario 2	23.4	26.2	7.40
Scenario 3	23.6	26.6	6.97
Scenario 4	28.2	31.2	0.82
Scenario 5	28.6	31.2	1.00

Table 5.5: Absolute error using DI_{energy} at $f_c = 150kHz$.

Scenario	x [cm]	y [cm]	error [cm]
Scenario 1	24.2	26.4	6.77
Scenario 2	26.6	31.8	1.41
Scenario 3	28.4	31.8	0.45
Scenario 4	29	31	1.41
Scenario 5	28.4	31.2	0.89

Influence of excitation frequency

The results shown in Figures 5.17 & 5.18 are based on the response signals using an excitation frequency of 150kHz. As was seen for the NASA dataset, the output of both the DIs and the subsequent image reconstructions are very much depending on the excitation frequency. To illustrate the effect of frequency, the reconstructed images for damage scenario 4 are shown for f_c = 250, 350 & $450kHz$ in Figure 5.19 & 5.20. From the images could be concluded that the algorithm still functions reasonably well for $f_c = 250kHz$. However, for higher frequencies the localization error increases as damages is centred towards to middle of the sensor array.

This behaviour was also seen for the dataset analysed in Section 4.5.2. The same reasons were found to be true for this case study. It was seen that in general an increase of the excitation frequency causes a decrease in the wavelength of the signal. This causes the wave to become more sensitive to smaller damage types such as intralaminar matrix cracks and subsequently leads to higher values of the DIs. Moreover, due to the bias induced by the algorithm during data fusion, an increase in DI leads sooner to higher pixel intensities at the center of the sensor network where most paths overlap.

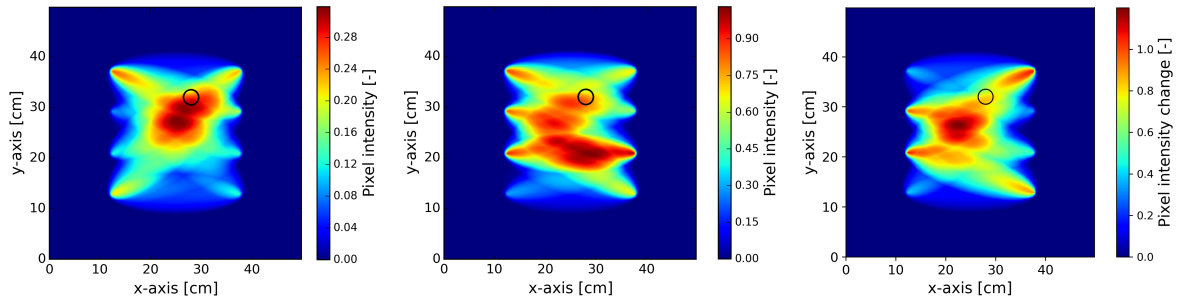

(a) $f_c = 250kHz$ (b) $f_c = 350kHz$ (c) $f_c = 450kHz$

Figure 5.19: Increases in frequency for scenario 4 using $DI_{pearson}$

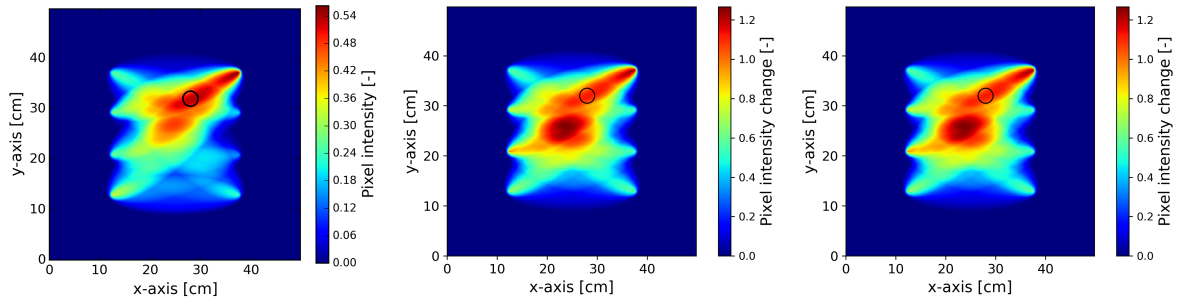

(a) $f_c = 250kHz$ (b) $f_c = 350kHz$ (c) $f_c = 450kHz$

Figure 5.20: Increases in frequency for scenario 4 using DI_{energy}

Differences in damage index

When taking a more detailed look at the values for the DI for this specific case study another conclusion could be drawn. The DIs are shown for $150kHz$ and $350kHz$ in Figures 5.21 and 5.22. The first two images show the difference in DI_{energy}, which show similar behaviour to the DI_{energy} in the previous chapter. An increase in f_c leads to higher DI values. However, when considering $DI_{pearson}$ very different behaviour was observed. Some paths showed a very large increase in the DI value, but when looking at the corresponding signals no signal shift or mode conversion of the wave packages was visible. This would also occur for paths further away from the damage location validated by the C-scan.

In order to clarify this behaviour, the response signal of path 26, actuator 7 & receiver 3 is shown in Figure 5.23. At first sight no disturbances of the signal are expected with respect to the known damage location. Moreover, the figure shows that the wave packages are nicely aligned. However upon closer inspection it was found that the high values for $DI_{pearson}$ are likely to be caused by the relatively low sampling rate of the recorded signals.

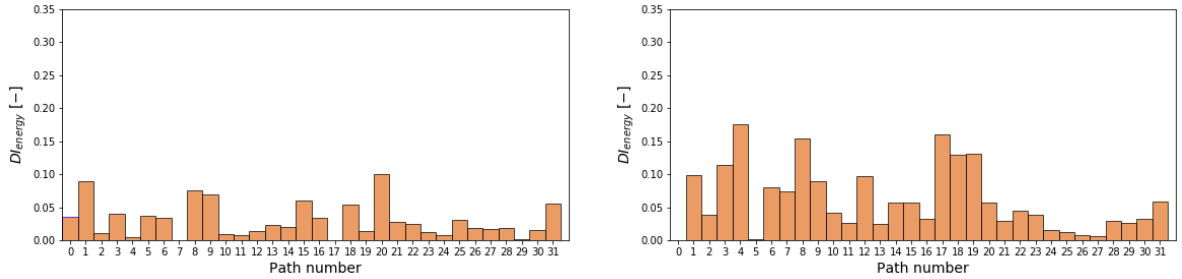

(a) $f_c = 150kHz$ (b) $f_c = 350kHz$

Figure 5.21: Energy damage index for scenario 4.

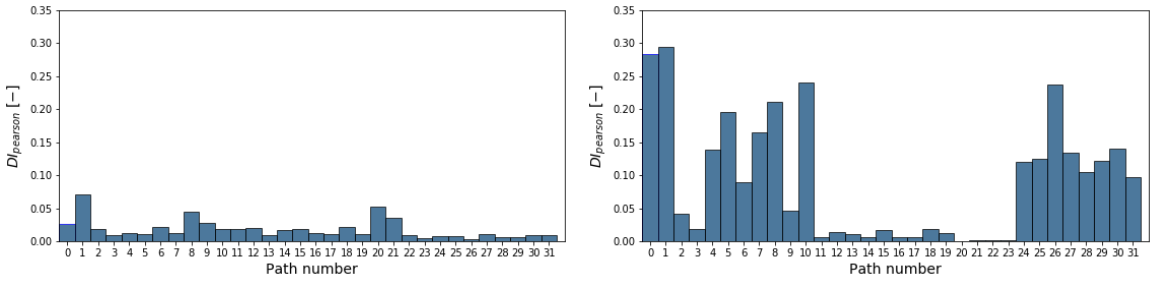

(a) $f_c = 150kHz$ (b) $f_c = 350kHz$

Figure 5.22: Pearson damage index for scenario 4.

In Figure 5.24 the same response signal is shown for path 26 from time 225 to 275μs. Although the sampling rate satisfies the Nyquist criteria, the signal looks quite rough. This will not have a very large influence on the DI_{energy}, but can have an effect on the $DI_{pearson}$ which is sensitive to a misalignment of signals. Thus, when the threshold for data acquisition or signal processing causes the signal to be shifted it will quickly result in the wrong values for $DI_{pearson}$. Re-aligning of the signals could be attempted by setting additional thresholds or by using cross correlation. However, correct re-aligning of the signals is difficult because damage might have caused a signal shift as well. It was also found that this disadvantageous effect will have a larger influence on signals with higher frequencies as alignment becomes more complicated due to the fact that less samples are used to construct a wave. For future research the author believes that the sampling rate of the response signals should be higher during sensor interrogation. Moreover, if one is determined to use the PCC to construct the DI it might be helpful to align signal recording with the bursts generated by the wave generator.

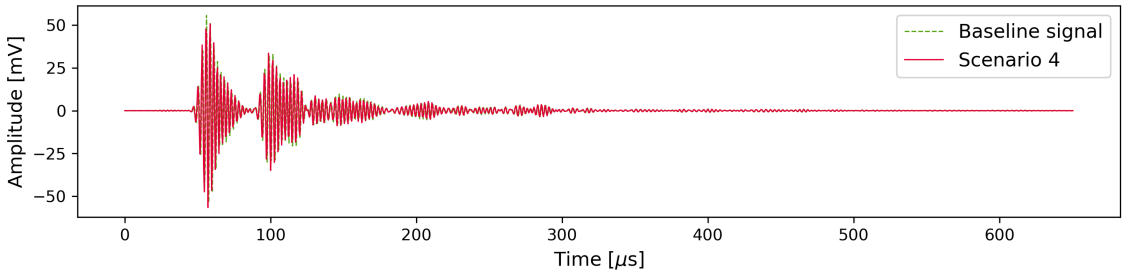

Figure 5.23: Path 26, actuator 7 & receiver 3 for 350kHz.

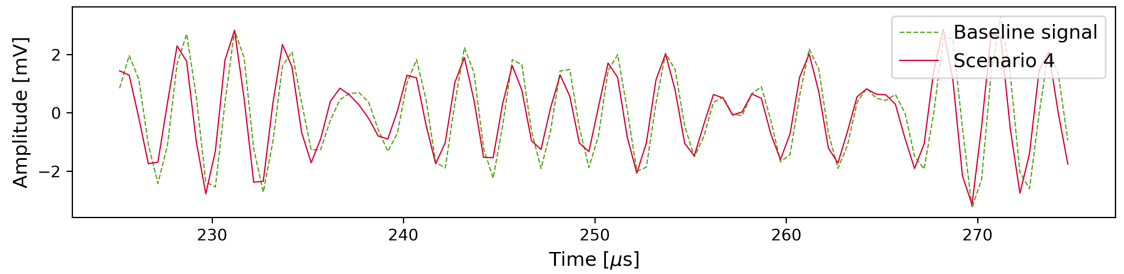

Figure 5.24: Path 26, actuator 7 & receiver 3 for 350kHz for $t = 225 : 275\mu s$.

Damage severity

From the reconstructed images in Figures 5.17 & 5.18 can be seen that the pixel intensity increases for an increase in damage. Figure 5.25 shows the change in pixel intensity experienced by the panel at the location of damage found using the c-scan (at $x = 28cm$ & $y = 32cm$). It also shows the cumulative AE energy of the QSI tests which can be used to define the extend of damage [80]. The graphs shows that both DI_{energy} & $DI_{pearson}$ increase for an increase in AE energy. However, the data points used to construct this graph are still limited.

Using clustering of AE signals and the different DIs, different damage types might then be identified. It could thus be interesting for future research to investigate if a relationship exists between these variables.

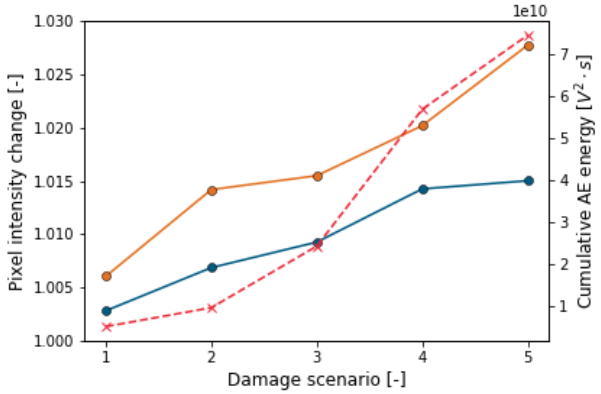

Figure 5.25: Increases in change in pixel intensity and cumulative AE energy.

The algorithms capability of recording damage growth is also visible when reviewing the values for the individual DIs. The DI resulting from the excitation signals at actuators 1,3 and 6 are shown in Figure 5.26 and Figure 5.27. From these images can be seen that damage growth was best captured by DI_{energy} while the $DI_{pearson}$ remained low, even for the more severe damage states. It also shows that more paths registered damage growth for DI_{energy} compared to $DI_{pearson}$.

Comparing the findings above to the performed analysis in Chapter 3 and the BVID creation using QSI testing discussed in Subsection 5.4.1 this difference between the DI formulations can be explained in different ways.

Firstly, the damage caused by indentation was very local. In a quasi-isotropic laminate multiple delaminations might be initiated but their size is expected to be small in comparison to a laminate made out of ply blocks as for example the cross-ply laminate from NASA. They also found that the dominant damage mode for a quasi-isotropic panel subjected to indentation is matrix cracking [80]. This means that the delamination damage could have been too small to have caused a signal disturbance.

Secondly, Lee reached the conclusion that the delamination mode during impact or indentation cannot be fully attributed to one particular fracture mode [75]. While it was shown that delaminations often originate from transverse matrix cracks in Mode I, they are driven by the shear stresses in Mode II. The delamination cracks are likely to be driven by different modes which are dependent on the location of transverse matrix cracks and the impact or indentation energy.

When the delaminations induced during the QSI tests were fully driven by Mode II, it could be that Lamb waves have not been separated by the delamination as was proposed earlier in Subsection 4.4.3. This implies that no signal shifts occur.

Finally, while a delamination in the cross-ply laminate would cause a stiffness change between the upper and lower layers, this effect could have been reduced by the quasi-isotropic lay-up so that the change in Lamb wave velocity was less apparent.

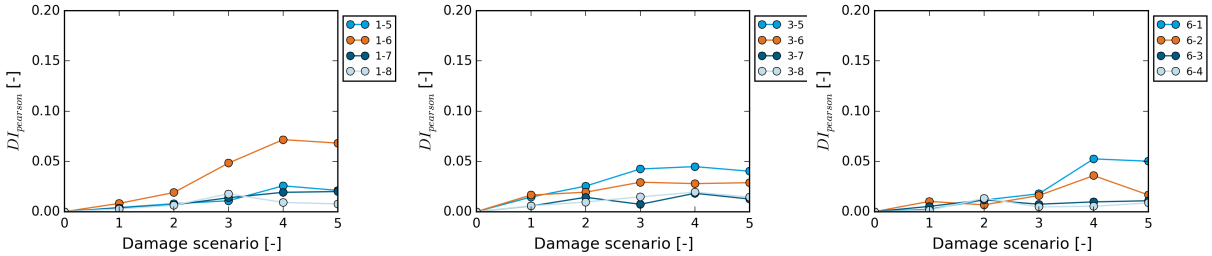

(a) Actuator 1 & receivers 5-8. (b) Actuator 3 & receivers 5-8. (c) Actuator 6 & receivers 1-4.

Figure 5.26: Pearson damage index for actuators 1,3 & 6 at $f_c = 150kHz$ for 5 damage scenarios.

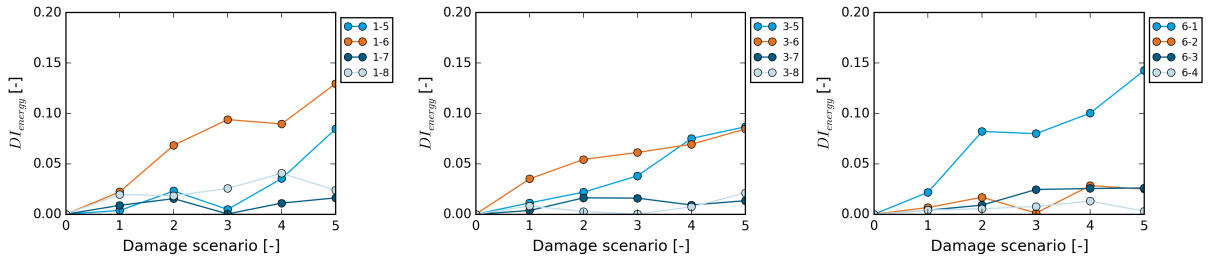

(a) Actuator 1 & receivers 5-8. (b) Actuator 3 & receivers 5-8. (c) Actuator 6 & receivers 1-4.

Figure 5.27: Energy damage index for actuators 1,3 & 6 at $f_c = 150kHz$ for 5 damage scenarios.

Besides evaluating the damage growth using the DI it was also attempted to apply a threshold to the reconstructed images in a similar manner as was discussed in Section 4.5.2. From Section 4.5.2 could be concluded that setting a threshold to the pixel intensity or to the change in pixel intensity led to the best results for the NASA dataset.

Figures 5.28 shows the reconstructed images for damage scenarios 4 and 5 using $DI_{pearson}$ and a threshold applied to the pixel intensity. The threshold was set to match the damage size of scenario 5 to the outcome of the C-scan.

As was mentioned at the beginning of this subsection, this is not entirely correct as the damage size obtained from the C-scan should match the response signals of scenario 6. Moreover, the damage size found using the C-scan was far below the ADL ($50.8mm$) described by the SRM so that a threshold could not be optimized for this limit.

Still when optimizing the threshold so that the damage in scenario 5 matches the results of the C-scan a threshold of $P_{thres} = 0.26$ was found. As a consequence, the algorithm defined scenarios 1-3 as undamaged.

In a similar manner a threshold was also applied to the pixel intensity for DI_{energy} shown in Figure 5.29. A threshold of $P_{thres} = 0.29$ was used to construct the images. This time, it was decided to adjust the threshold so that also scenario 3 would contain damage. However, it becomes clear from these figures that using such a threshold severely overestimates the damage sizes of scenario 4 & 5. This might be due to the fact that DI_{energy} is sensitive to matrix cracks which are not shown by the C-scan.

The change in pixel intensity was also evaluated and is shown in Appendix K. The same behaviour when applying a threshold was seen. It could moreover be concluded from these images that damage growth was less well monitored using the change in pixel intensity compared to the NASA dataset. This was because of the less dense sensor network.

Overall, it seems that the C-scan underestimated the damage with respect to the transverse matrix cracks. On the other hand, IMRA also overestimated damage when a threshold is applied to detect very small damage sizes. This was shown by applying a threshold to match damage scenario 3. This means that in order to evaluate the algorithm for its severity estimation on this panel, another NDT technique should be applied to identify the severity of matrix cracks present inside the structure. This could help to identify the right thresholds and validate the system.

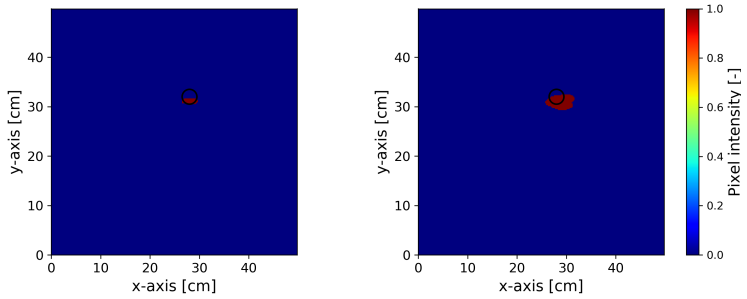

(a) Scenario 4: Displacement 12.3mm. (b) Scenario 5: Displacement 13.4mm.

Figure 5.28: Applying a threshold to the pixel intensity: Scenario 4-5 using $DI_{pearson}$, $f_c = 150kHz$ and $P_{thres} = 0.26$.

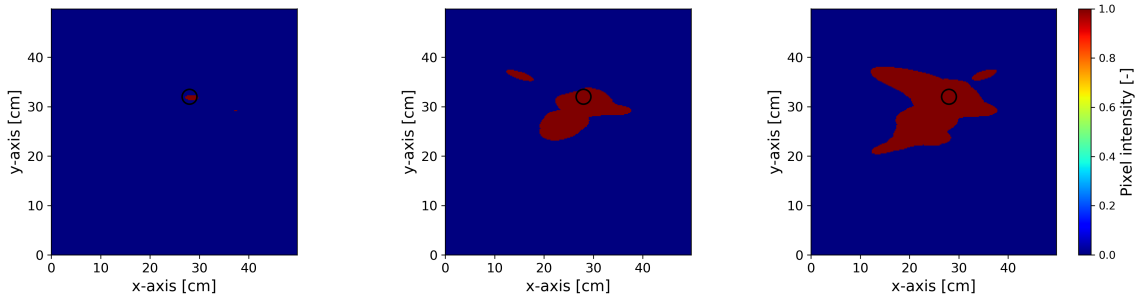

(a) Scenario 3: Displacement 9.7mm. (b) Scenario 4: Displacement 12.3mm. (c) Scenario 5: Displacement 13.4mm.

Figure 5.29: Applying a threshold to the pixel intensity: Scenario 3-5 using DI_{energy}, $f_c = 150kHz$ and $P_{thres} = 0.29$.

5.5.3. Sensor failure

In has been previously mentioned that one of the reasons for the slow implementation of SHM into the commercial aviation industry is the fear of the SHM system failing. Failing of the system can lead to false-negative, false-positive and incorrect localization and or sizing of damage. Initially, the author wanted to analyse the algorithms response to sensor failure by turning one of the sensors off during signal processing. However sensor 3 actually failed during the final QSI test and it was therefore not possible obtain a full dataset for scenario 6. It was thus decided to reconstruct the images for the final damage scenario using the other 7 sensors. In order to evaluate the influence of the failed sensor, the same sensor was turned off for a reconstruction of scenario 4 and 5.

The reconstructed images are shown in Figure 5.30 and Figure 5.31.

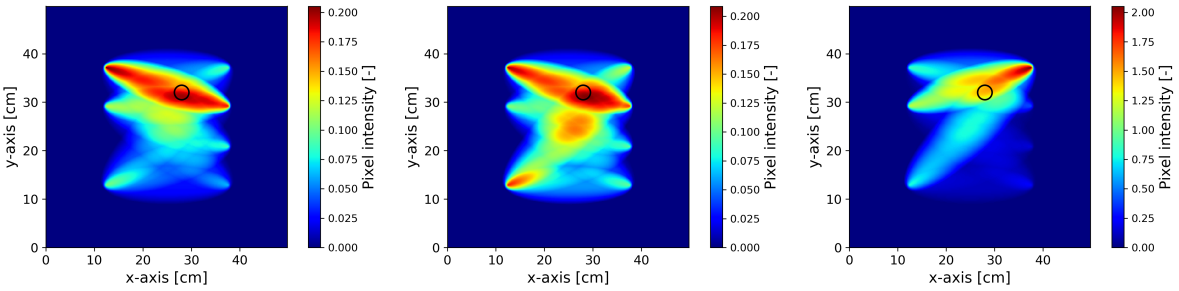

(a) Scenario 4: 12.3mm. (b) Scenario 5: 13.4mm. (c) Scenario 6: 15.5mm.

Figure 5.30: Image reconstruction with failed sensor 3 using $DI_{pearson}$ at $f_c = 150kHz$.

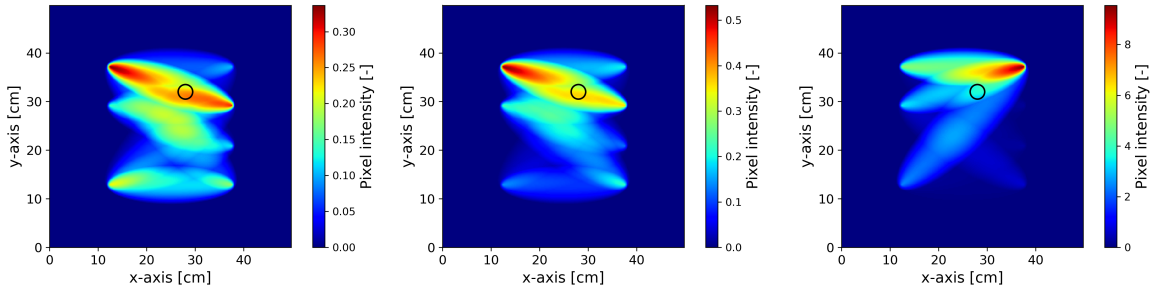

(a) Scenario 4: 12.3mm. (b) Scenario 5: 13.4mm. (c) Scenario 6: 15.5mm.

Figure 5.31: Image reconstruction with failed sensor 3 using DI_{energy} at $f_c = 150kHz$.

A few things should be mentioned for this particular series of reconstructed images. Every failed sensor will affect the algorithm's output in a different way. This depends on the location of the sensor with respect to other sensors and to the damage location itself. For this particular case it might be concluded that the failure of sensor 3 is very harmful for the algorithm's output.

This is due to the fact that the orientation angles between the paths for this sensor network are quite small. Sensor 3 is connecting the diagonal paths propagating through the damaged areas using the paths between sensors 3 & 5 and sensors 3 & 6. This causes the other paths to shape the damage like an ellipse. In this case the ellipse shows up between sensors 1 & 6.

Thus in order to reconstruct the right location of the damage it is important to have multiple paths crossing the same areas under different angles. This was also seen in Section 4.5.2 when applying a threshold to the DI. This effect could be reduced by changing the shape of the sensor network and the application of more sensors.

The DIs for all paths excluding sensor 3 are shown for scenario 6 in Figure 5.32. It can be seen that there has been a significant increase in the magnitude of the DI values compared to the values found for scenario 5. This means that the damage has increased substantially. From the DI values found is was concluded that the dominant damage mode is indeed matrix cracking. From the signal could also be seen that a large signal shift was now visible.

This shows that the damage in scenario 1-5 might not have been severe enough to have caused a change in the Lamb wave velocity or to have cause a mode conversion. Examples of two paths propagating through the damage showing signal shifts are shown in Figures 5.33a & 5.33b. These figures indicate the presence of a delamination because of the observe shifts and the increase in signal amplitude.

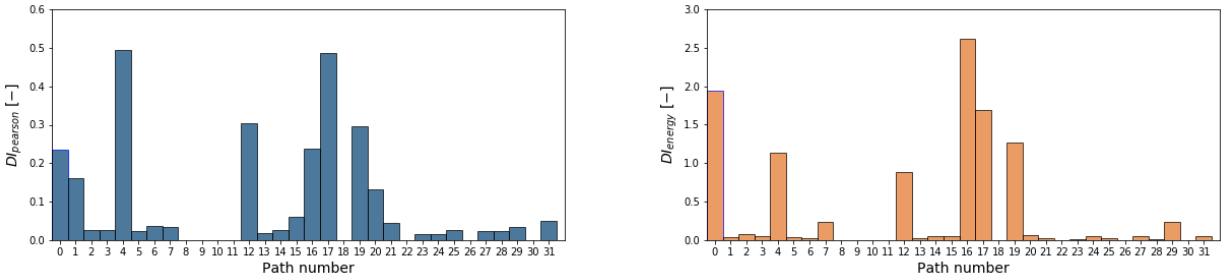

(a) Pearson damage index at $f_c = 150kHz$. (b) Energy damage index at $f_{exc} = 150kHz$.

Figure 5.32: Damage indices for scenario 6.

Finally, a threshold was also applied to the reconstructed images for scenario 6. This is shown in Figure 5.34. The large differences in DI values also resulted in a large difference for the pixel intensity. For this reason, no threshold could be applied to scenario 6 which matches the outcome of the C-scan and also considered scenarios 4 & 5 to be damage. Due to sensor failure IMRA also locates the damage at the wrong location.

From this subsection could be concluded that the damage in scenarios 1-5 was likely to have been very small. However, it could still be detected using IMRA. It also means that much more validation data is required during future research to find the optimal thresholds.

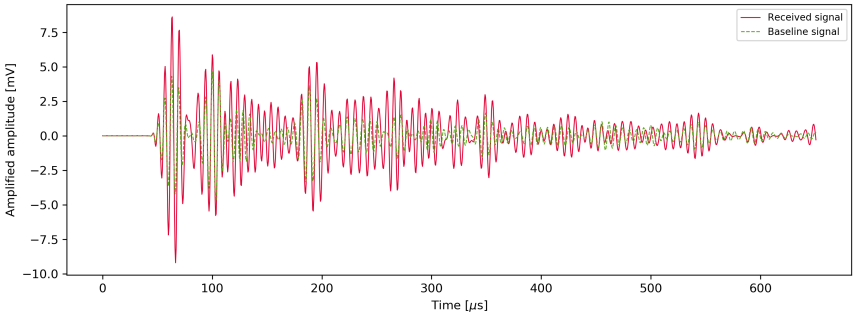

(a) Path 16, actuator 5 & receiver 1 for $f_c = 150kHz$.

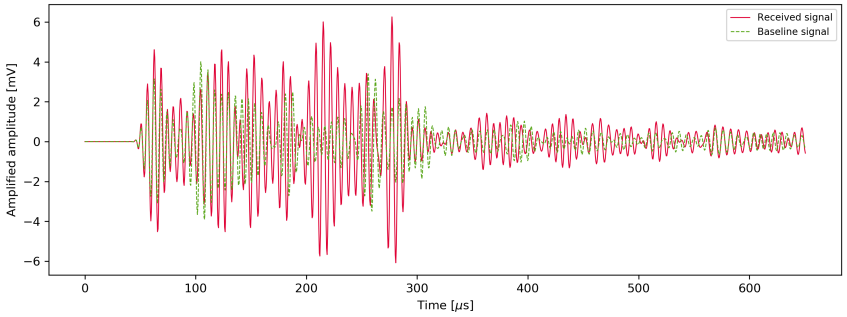

(b) Path 17, actuator 5 & receiver 2 for $f_c = 150kHz$.

Figure 5.33: Response signals for paths 16 and 17 for damage scenario 6.

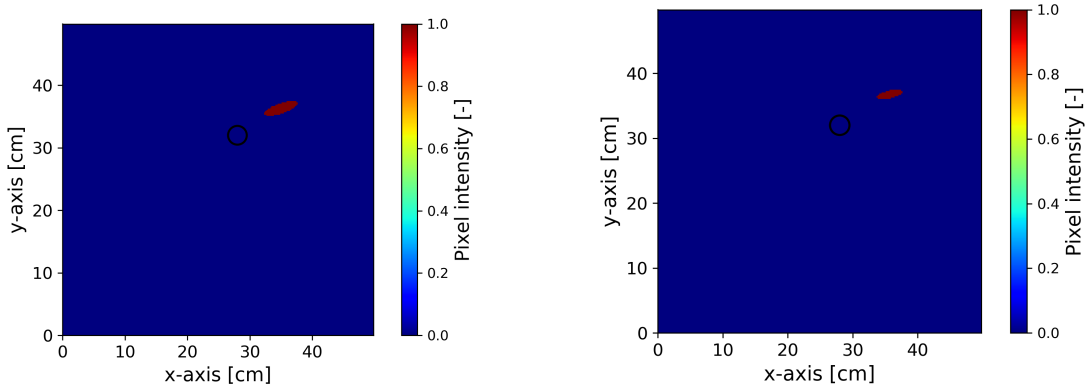

(a) Reconstruction using $DI_{pearson}$.

(b) Reconstruction using DI_{energy}.

Figure 5.34: Image reconstruction for the performed blind test for at $f_c = 150kHz$.

5.6. Conclusion

In this chapter a case study for a composite laminate similar to a Boeing 787 skin panel was presented. The design of the test panels resembled one of the door surrounding structures of a Boeing 787 fuselage which are prone to impact from ground operations. Because BVID might be overlooked during conventional inspections it is important to develop fast and accurate monitoring systems.

The purpose of this case study was to evaluate the algorithm's performance using a more realistic structure and damage type than what is often presented in literature. It was found that QSI tests can create similar BVID as LVI in a step-by-step process while the presence and progression of damage could be validated through an analysis of the force-displacement behaviour and the use of AE monitoring.

In Section 4.6 of the previous chapter four factors having a large influence on the performance of IMRA were identified. This case study revealed a number of additional factors which should be taken into consideration while designing future SHM systems. They are shown in Figure 5.35.

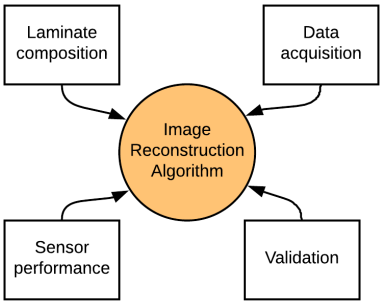

Figure 5.35: Factors that influence IMRA.

Firstly, the laminate composition was demonstrated to affect the capability of the algorithm to detect, located and size damage. The type and size of the damage mechanisms occurring after impact are dependent on the laminate composition, e.g. the material and lay-up. It moreover affects the way in which damage progresses and how Lamb waves interfere with the different damage types.

From a QSI test, transverse matrix cracks, delamination and fiber failure can be expected. However, during the case study in turned out to be difficult to detect and size the induced delaminations using IMRA. This could be due to several reasons. Firstly, it was found that the QSI test might not have caused delaminations which were large enough to be detected using Lamb waves. This is supported by the fact that the $DI_{pearson}$ values were very small after damage scenarios 1-5, while much higher values were found after scenario 6. Secondly, it could not be stated if a delamination after a QSI test is dominated by a Mode I or Mode II fracture mode. If the delamination is dominated by Mode II, the space between the delaminated plies might be too small to cause a real separation of the Lamb waves so that no velocity changes or mode conversions occur. Finally, it was found that delaminations in a cross-ply laminate cause a stiffness change between the layers above and below the delamination. This effect might be reduced by the quasi-isotropic lay-up of the test panels so that velocity changes are less severe.

Secondly, it became apparent from the blind QSI test that the presence of damage could not be determined without making a comparison to the outcome of an alternative NDT inspection. However, it was also shown that not all NDT techniques are capable of detecting the different damage mechanisms found in composites. For the blind test and the series of QSI tests, both the X-ray and C-scan inspections were unable to detect the intralaminar cracks, even after cracks could be clearly seen on the bottom of the second panel after scenario 6. The algorithm did indicate cracks at the location of the indenter for the blind test.

This brings us to the third factor shown in Figure 5.35. More experimental data is required to fully validate the system's output. Without additional measurements such an SHM system cannot be made applicable to the commercial aviation industry. The data is needed to select a suitable threshold as discussed at the end of Chapter 3. When applying a threshold to the pixel intensity, it showed that when damage is to be detected at an early stage the subsequent images tend to overestimate the damage size. However, from the C-scan alone it could be concluded by how much the damage is really overestimated as the algorithm is capable of taking the intralaminar matrix cracks into account.

In general this brings us to the conclusion that future research should also focus on obtaining validation data for the different/intermediate damage states as well. The author believes that there are two ways in which the SHM system's performance might be evaluated and improved. The first solution is to create a database so that thresholds can be established based on statistics. Secondly, simulations can be made of the panel to generate the required validation data. This does mean that the material properties should be known in order to simulate the structure's behaviour.

Finally it was observed that the data acquisition equipment affects the algorithm. It was shown that making use of AE equipment normally suited for passive SHM can results in errors in the alignment of the baseline and response signals. This error seems to increase for higher frequencies. It was moreover seen that the sampling rate of the signals should be high when the PCC is used for the DI formulation so that signal shifts due to damage are recorded correctly.

6

Conclusions & Recommendations

The research presented in this thesis aimed at contributing to an image reconstruction technique which is able to detect, locate, and monitor the progression of BVID. The increased use of composite materials in commercial aircraft demands the MRO industry to get rapidly acquainted with the maintenance of composite structures. Composite structures show complex failure modes. Little is known about what triggers them and how these modes interact. Composite structures are especially prone to in-service impact which can cause BVID. This type of damage is difficult to inspect, easy to be overlooked, and can grow to adversely affect the structural integrity of the structure.

By applying a suitable SHM system, the speed and ease of inspections can be increased. It might also lower both the direct and indirect costs of maintenance and offer more insight into the progression of composite damage. However, it was found that SHM systems are hardly ever implemented into the commercial aviation industry, while many SHM techniques have been argued to be commercially ready.

This research has focussed on the useful implementation of an active acoustic image reconstruction technique using PZT sensors by performing an analysis on the reconstruction algorithm itself and its input data. Firstly, a dataset from the NASA Prognostics Data Repository was analysed. Hereafter, a case study was performed to generate more input data. Two test campaigns were conducted on quasi-isotropic test panels resembling the Boeing 787 fuselage skin. The first campaign functioned as a blind test while the second campaign focussed on a series of QSI tests until failure.

For the analysis different excitation frequencies, DI formulations based on PCC and signal energy, and different threshold methods were explored. This functioned as the first step in the capability assessment of an image reconstruction technique which not only focusses on damage localization, but also on damage severity estimation. The main findings from the analysis in Chapter 4 and the case study performed in Chapter 5 can be divided into five categories:

Central excitation frequency of the input signal.
This research has shown that IMRA's performance is dependent on the central excitation frequency of the input signal. For both the NASA dataset and the case study, the algorithm worked particularly well at one of the excited frequencies, being $f_c = 200kHz$ and $f_c = 150kHz$ respectively. This suggested that the algorithm's functioning is limited to a range of frequencies which depends on the structure and should be identified prior to an SHM application.

In general, it could be concluded that a higher central excitation frequency relates to a smaller wavelength so that the DIs become more sensitive to smaller forms of damage. This was shown by the increased sensitivity of DI_{energy} to intralaminar matrix cracks. The influence of the excitation frequency also turned out to depend on the dispersive behaviour of the waves. For instance, the PCC was found more sensitive to delaminations at an $f \cdot d$ for which the Lamb waves behaved dispersive because this enhanced the differences in wave velocity.

Data acquisition and signal processing.
From the experimental campaigns was found that the equipment for data acquisition should be carefully selected. While the usage of an AE acquisition system allows for the blending of an passive and active SHM technique, it records waves based on the ToA and a voltage threshold. This might cause a misalignment

between the baseline and current state signals as the ToA can change due to damage or noise. The voltage threshold should thus be carefully selected. It was also found that a low sampling rate can negatively effect the values of the DI. It was shown that, even though the sampling rate of the recorded signals fulfilled the Nyquist criteria, it led to unrealistic high values of $DI_{pearson}$.

Finally, several articles proposed to window response signals around the direct propagated waves between two sensors, so that reflections from geometric boundaries and damage are excluded from the analysis. However, it was demonstrated that the boundaries of such a window might not or wrongly incorporate the disturbances of the response signals which were caused by damage. As a result, the reconstructed image could wrongly evaluate some locations to be more severely damaged than others.

Formulation of the damage index and threshold.
This research has also revealed that the formulation of the DI affects the location and estimated severity of damage found using IMRA. This was supported by a difference in behaviour between $DI_{pearson}$ and DI_{energy}. While the $DI_{pearson}$ was found to be more sensitive to delaminations, DI_{energy} was found to be more suitable for the detection of intralaminar matrix cracks in the lower frequency range. The positive side of this conclusion is that this finding suggests that through a careful selection of the DI, different types of damage can be identified. On the other hand, danger lies in the fact that apparently not every formulation of a DI is capable of capturing all sorts of damage.

Besides the formulation of the DI, it was found that the chosen threshold affects the algorithm's capability to correctly locate and size damage. The probabilistic nature of the algorithm caused damage at locations where multiple paths overlap to be estimated as more severe compared to locations where fewer paths overlap. This problem was partially overcome by evaluating the change in pixel intensity instead of the pixel intensity itself. For the NASA dataset, this showed very promising results. However, it was less promising for the data obtained during the case study. This was probably due to the sensor network being less dense.

Material composition.
It was found that the capability of the algorithm is influenced by the laminate composition, e.g. ply material and lay-up. Firstly the damage mechanisms that occur are affected by the laminate composition, and secondly it affects the Lamb wave interaction with damage. This means that when designing an SHM system to perform an inspection one needs to understand which damage mechanisms exists inside the material.

While for the cross-ply laminate taken from the NASA dataset a clear distinction between the delamination and matrix cracks could be seen from the response signals, this distinction was less obvious for the quasi-isotropic lay-up used during the case study. Damage created by the QSI test was very local, causing the signal shift due to delamination to be less severe. It was also found that the stiffness of the material above and below a delamination changes for a cross-ply laminate, which causes a change in Lamb wave velocity. This behaviour will be less apparent for a quasi-isotropic laminate as the change in stiffness is less profound.

Sensor performance.
Sensor failure during the experimental campaign of the case study demonstrated the negative effect on the algorithm's outcome. For this network and the location of damage it was found that this sensor failure causes the algorithm to be incapable of correctly locating the damage as the difference in orientation angles between the other paths was rather small. The damage therefore obtained an elliptical shape. However, the performed analysis was limited to the failure of one sensor only. Due to the low number of sensors and limited damage scenarios, an experiment should be performed on a larger scale to quantitatively state something about its influence.

Validation by an alternative technique.
The experimental campaign in Chapter 5 demonstrated that the outcome of an SHM system cannot be evaluated without making a comparison with another technique. The location and size estimation have to be justified using another NDT technique in order to optimally select parameters such as the DI, excitation frequency and also a threshold for the pixel intensity or change in pixel intensity.

Nevertheless, the campaign also showed that the applied NDT techniques were not always capable of providing the right damage diagnosis either. Damage which could be detected visually was not detected using an X-ray inspection. Moreover, the intralaminar matrix cracks detected by the algorithm were not shown on the C-scan. What should be taken away from this finding is that the author believes that further SHM research should also focus on how conventional NDT techniques can be compared to the SHM system's output.

While summarizing the findings above, it can be said that this research has shown the potential of the proposed data analysis method or IMRA to successfully detect, locate, and monitor the growth of BVID. It has been demonstrated that the location of damage could be determined within 1 to $2cm$ using the DI_{energy} on a quasi-isotropic lay-up. As damage progression was validated using a passive AE approach, both the individual values of the DI and the pixel intensities of IMRA's output were shown to increase for damage growth. However, a threshold must be carefully selected to evaluate the size of damage. Besides the capability to locate and size damage, the analysis of the DI formulation showed that IMRA could potentially also be useful for the identification of damage types in the future.

Overall, this study showed that various parameters limit the performance of IMRA. Many of these parameters were considered a constant in other research, such as the usage of one excitation frequency or one DI type. It was also concluded that using laminates commonly applied in research, such a cross-ply laminates show 'optimistic' results with respect to typical aircraft structures. Therefore, this research shows the importance of performing research on real aircraft structures to identify the hidden parameters affecting the behaviour of an SHM system well before it can become commercially applied.

Apart from the fact that the algorithm requires fine-tuning of several parameters for the generation of acceptable results, several other limitations to this research should be considered.

Firstly, the number of experiments conducted during the case study were limited. It showed to be difficult to compare the outcome of IMRA to the performed NDT tests. In order to establish a relationship between the real damage growth rate and growth rate found by the algorithm, more extensive experiments should be performed. Preferably, NDT tests should be performed inbetween the different QSI tests to investigate if besides an positive relation between the two, also more detailed relation could be found.

Moreover, it was seen that the laminate composition has an effect on the type of Lamb wave interaction with damage. However, this conclusion was drawn from a comparison between different types of test panels (a dog-bone specimen for NASA and a larger panel during the case study). In addition, the NASA specimen contained fatigue damage while impact damage was simulated during the case study. Further research is required to identify and quantify the differences for different lay-ups on a similar geometry.

Furthermore, QSI tests have been used to simulate impact damage. Although QSI can be used to evaluate the different phases of impact damage creation, it does not represent the progression of impact damage under fatigue loading as would be the case for a real aircraft structure. Therefore, the test panels should also be subjected to fatigue tests after impact damage is induced in order to monitor the grow of damage into more detail.

Considering the conclusions and limitations stated above, some additional recommendations were formulated for future research. Firstly, future research should focus on the creation of a database which not only contains response data of different damage types, levels of damage severity and material compositions, but it should also focus on creating a sufficient amount of validation data as this is currently the limiting factor in the evaluation of SHM systems.

Secondly, the results suggest that damage types can be identified by using different DI formulations. A future study could focus on the identification of damage types using different DIs and different lay-ups. For example, does a DI based on the PCC function for both the detection of Mode I and Mode II delaminations? It was also seen that the excitation frequency affects the sensitivity of the DIs. Future research could focus on how to select the excitation frequency in an efficient manner into more detail.

Moreover, although AE monitoring has not been certified as an allowed method of inspection for aircraft structures, the author believes it could be interesting to combine the response of AE monitoring with the output of IMRA to see if relationships can be found. The advantages of combining these two methods is that the same equipment might be used to analyse the structure.

On a final note, it might be concluded that an active SHM system based on Lamb waves offers a new alternative to existing methods of inspection. Image reconstruction has shown to be capable of detecting, locating and monitoring the growth of different types of damage. However, the work presented also showed that the image reconstruction is very sensitive to the fine-tuning of several parameters which made validation complicated. Additional experiments are required in order to substantiate the true potential of applying IMRA onto a commercial aircraft.

A

B787: Composite Structure Inspection

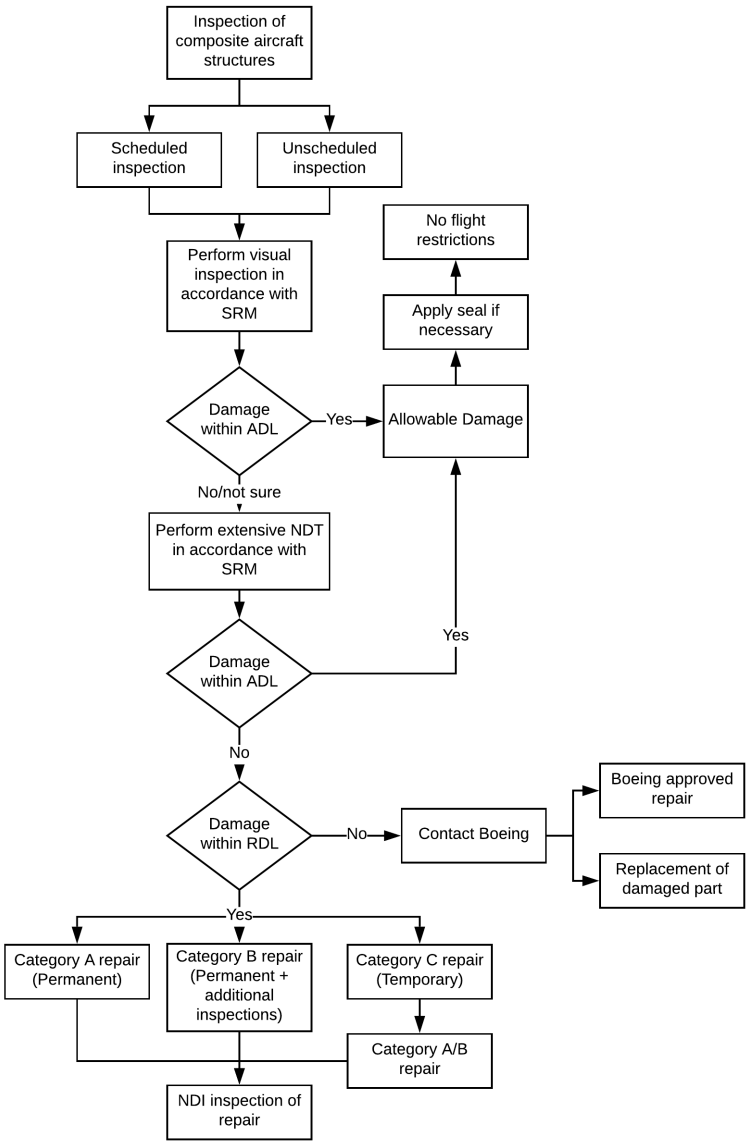

Figure A.1: Inspection of composite structures according to the Boeing 787 SRM [26].

B

IMRA: Structure of Python Code

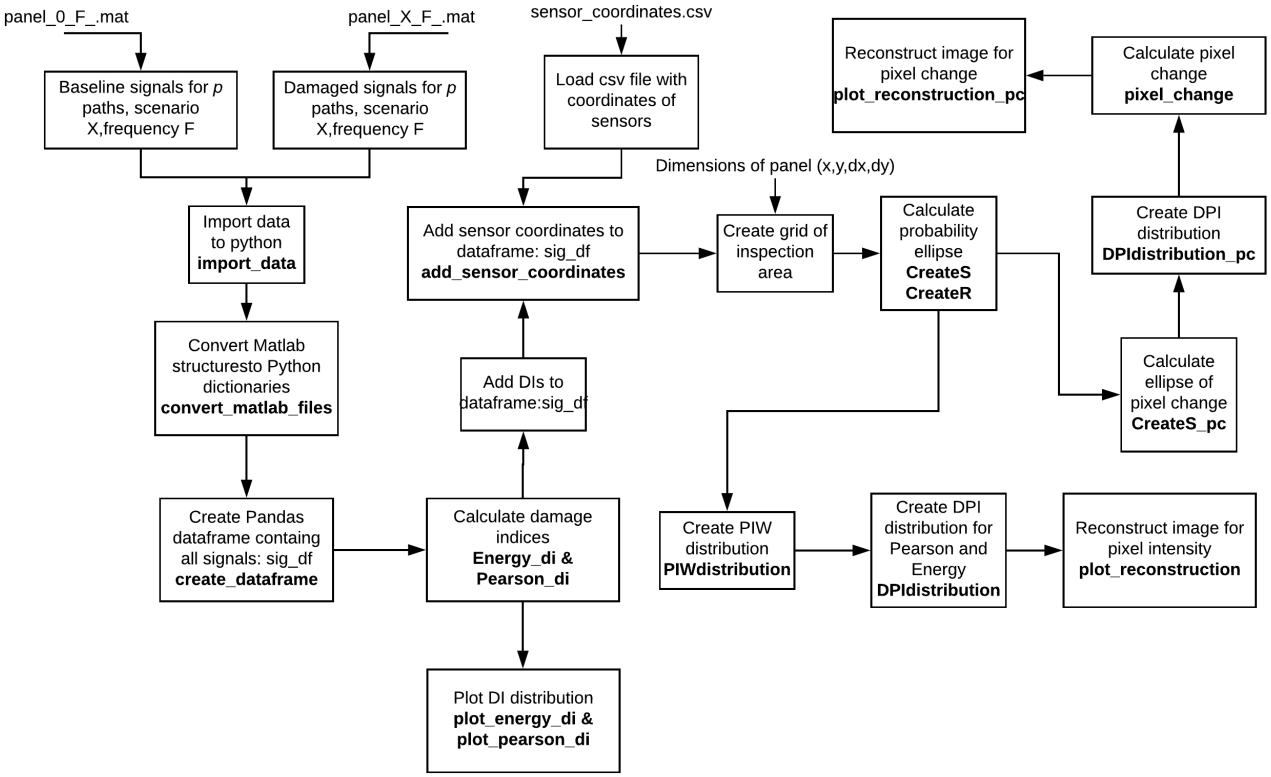

Figure B.1: Flowchart of the Python code.

C

NASA: Additional DI Charts

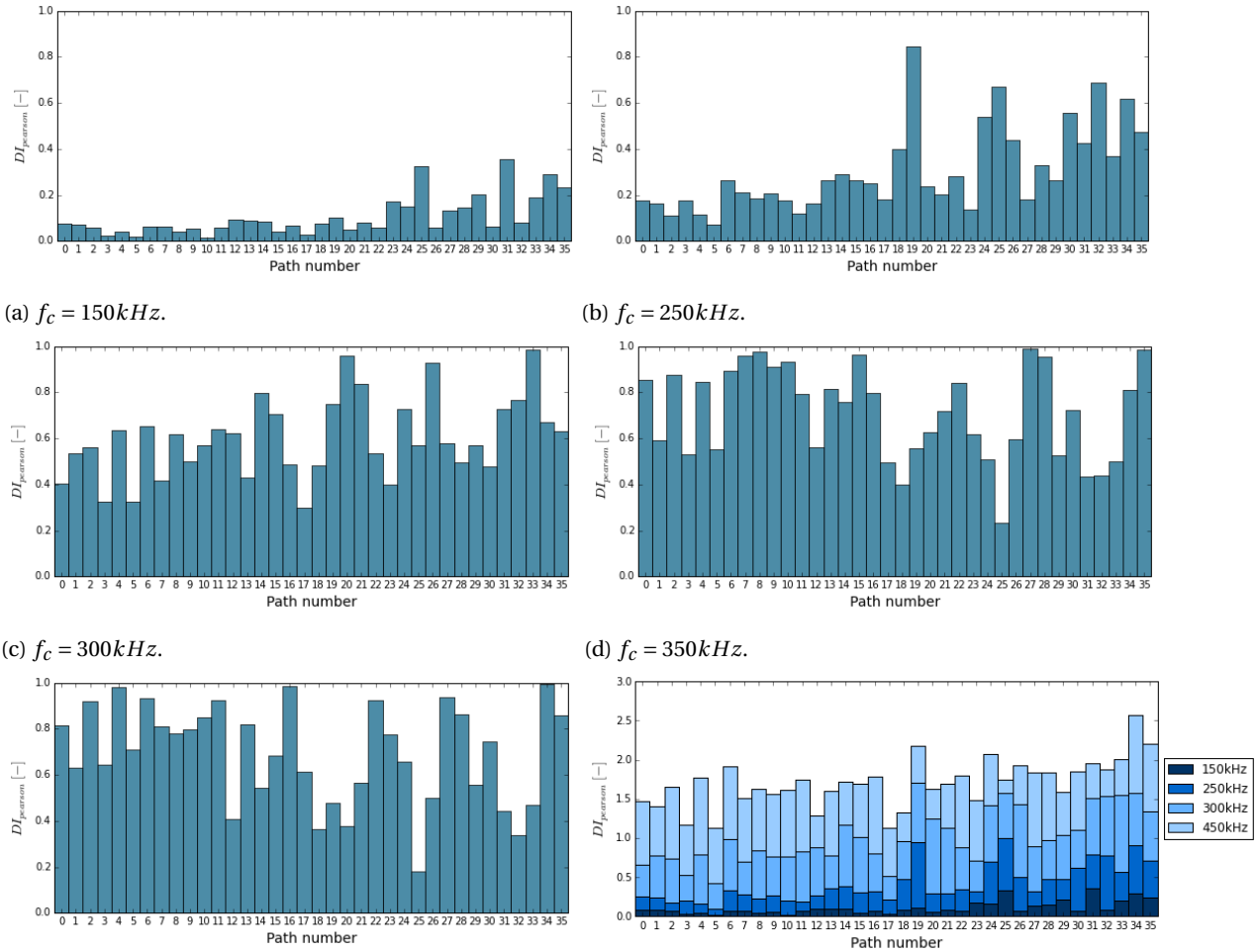

(a) $f_c = 150kHz$.

(b) $f_c = 250kHz$.

(c) $f_c = 300kHz$.

(d) $f_c = 350kHz$.

(e) $f_c = 450kHz$.

(f) Stacked $DI_{pearson}$ for multiple frequencies.

Figure C.1: Pearson damage indices for different frequencies for L1S19 after 100 cycles.

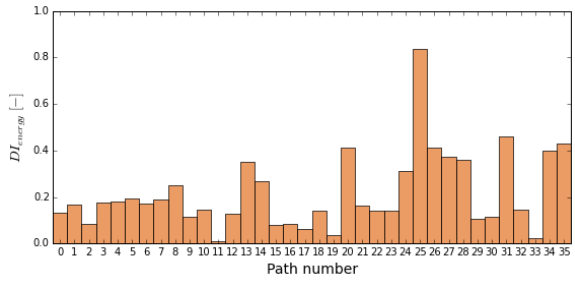

(a) $f_c = 150kHz$.

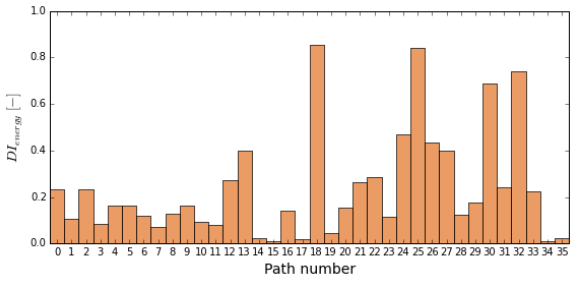

(b) $f_c = 250kHz$.

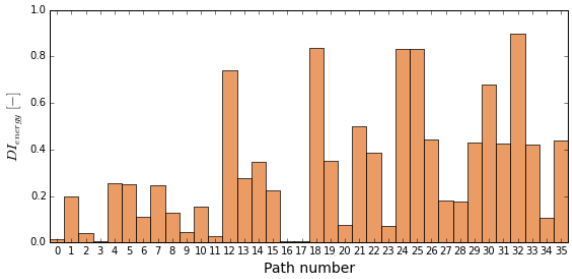

(c) $f_c = 300kHz$.

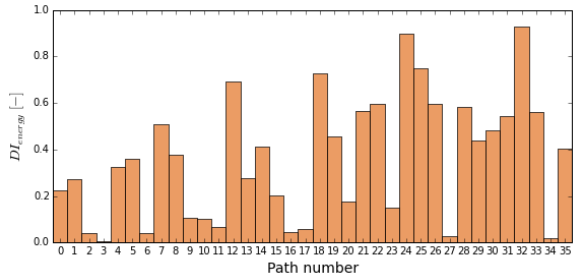

(d) $f_c = 350kHz$.

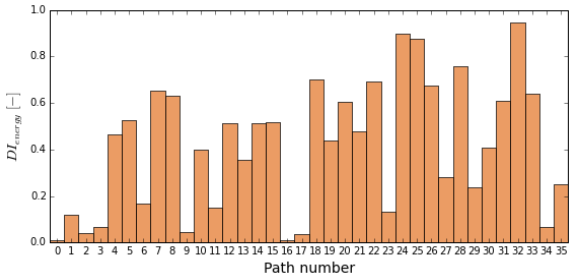

(e) $f_c = 450kHz$.

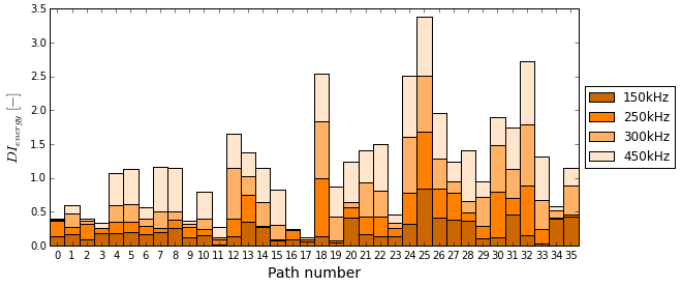

(f) Stacked DI_{energy} for multiple frequencies.

Figure C.2: Energy damage indices for different frequencies for L1S19 after 100 cycles.

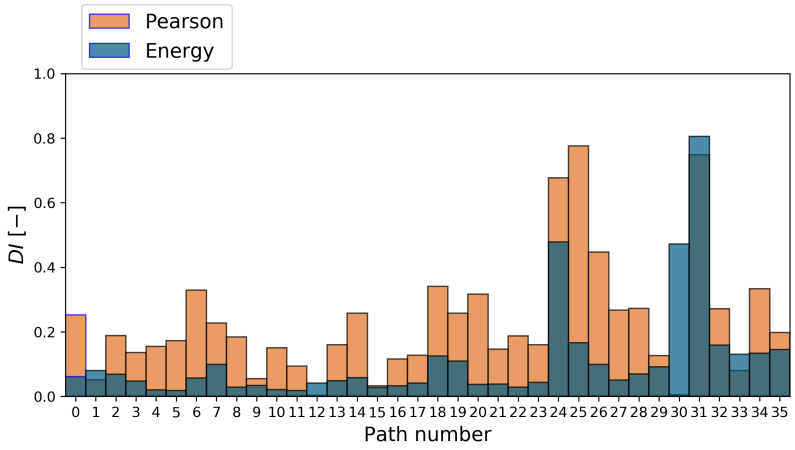

(a) After 10 cycles.

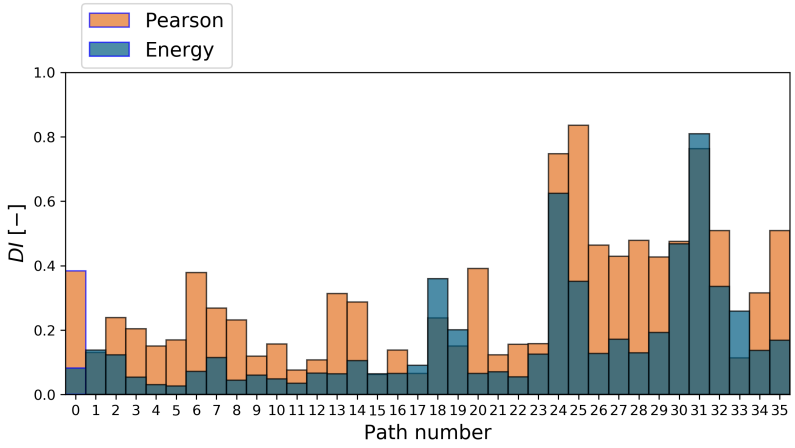

(b) After 100 cycles.

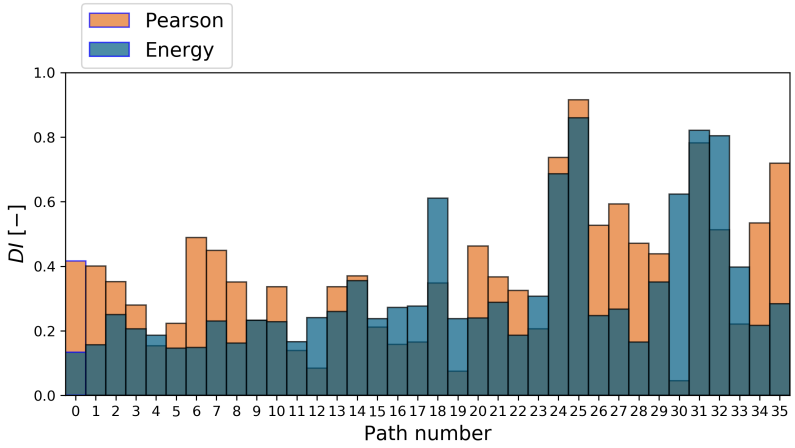

(c) After 1000 cycles.

Figure C.3: DI comparison for L1S19 after 10, 100 & 1000 fatigue cycles and $f_c = 200kHz$.

D

NASA: Additional Results

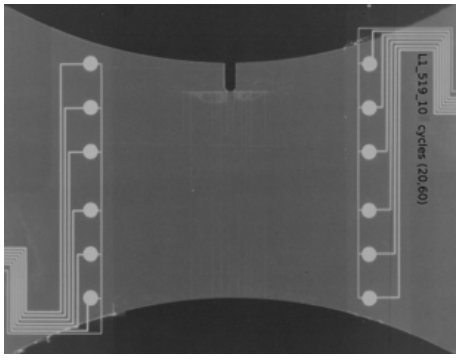

(a) After 10 cycles.

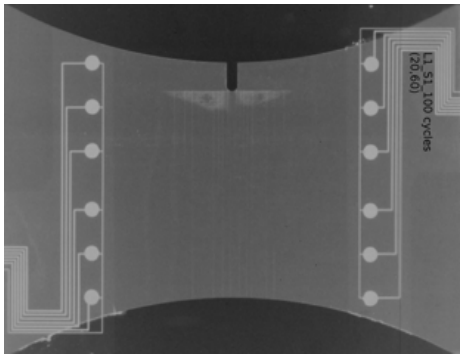

(b) After 100 cycles.

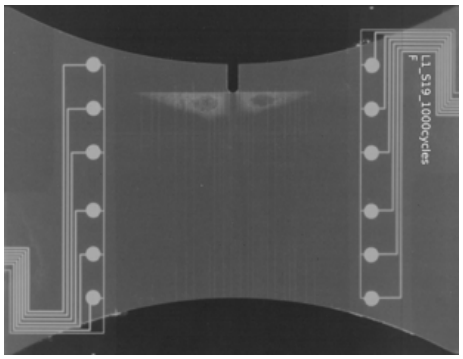

(c) After 1000 cycles.

Figure D.1: Original X-ray images taken from L1S19.

D.1. Pixel Intensity: $DI_{pearson}$

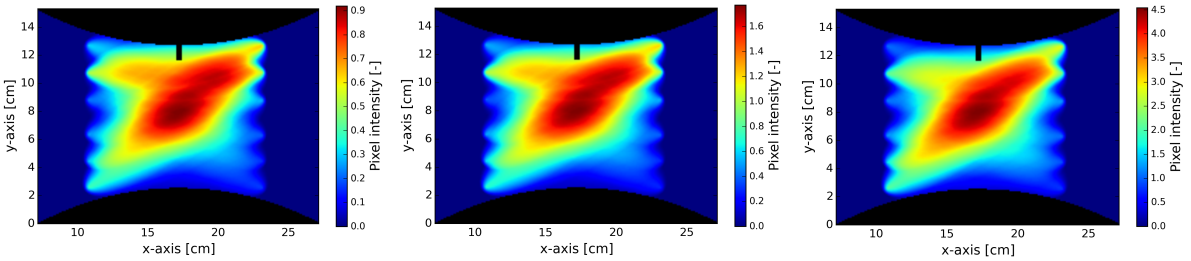

(a) After 10 cycles. (b) After 100 cycles. (c) After 1000 cycles.

Figure D.2: Pixel intensity using $DI_{pearson}$ and $f_c = 150kHz$.

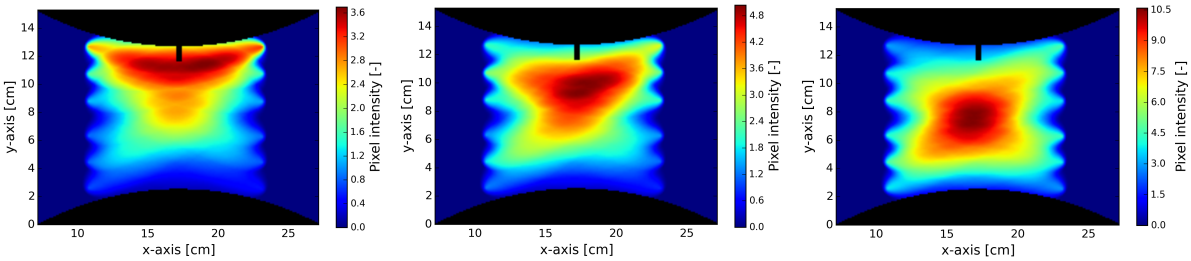

(a) After 10 cycles. (b) After 100 cycles. (c) After 1000 cycles.

Figure D.3: Pixel intensity using $DI_{pearson}$ and $f_c = 250kHz$.

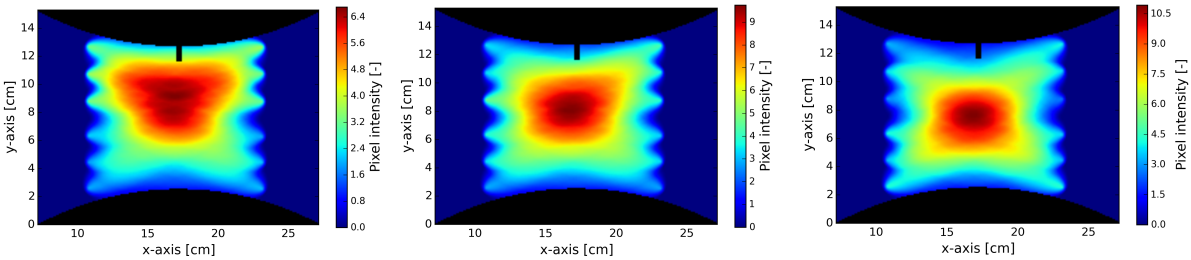

(a) After 10 cycles. (b) After 100 cycles. (c) After 1000 cycles.

Figure D.4: Pixel intensity using $DI_{pearson}$ and $f_c = 300kHz$.

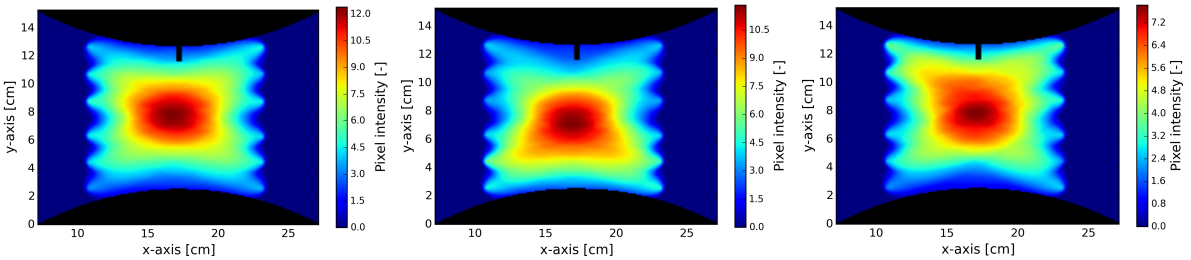

(a) After 10 cycles. (b) After 100 cycles. (c) After 1000 cycles.

Figure D.5: Pixel intensity using $DI_{pearson}$ and $f_c = 450kHz$.

D.2. Pixel Intensity: DI_{energy}

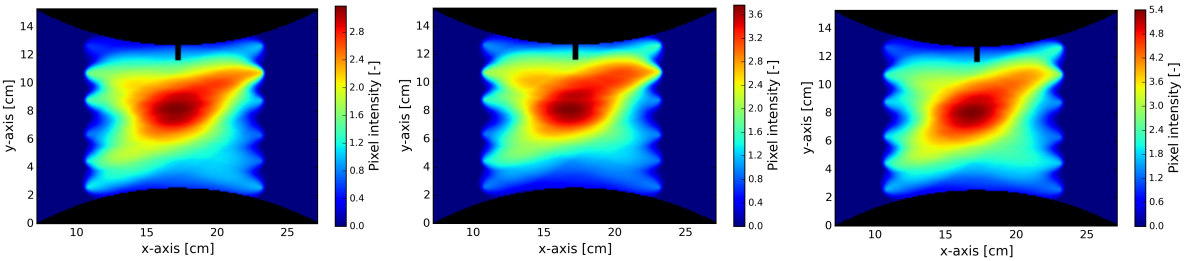

(a) After 10 cycles. (b) After 100 cycles. (c) After 1000 cycles.

Figure D.6: Pixel intensity using DI_{energy} and $f_c = 150kHz$.

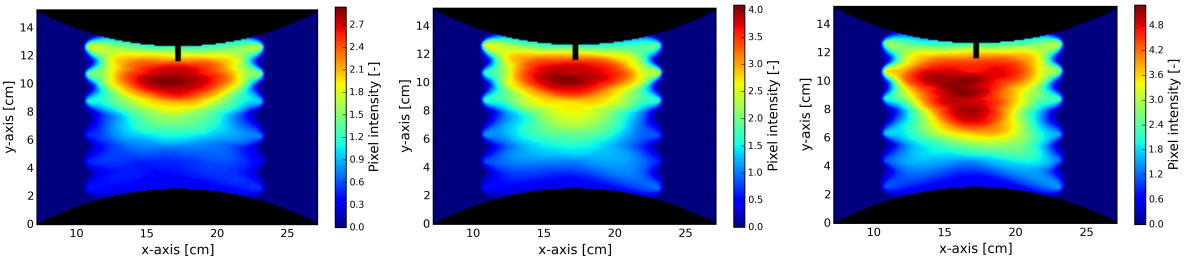

(a) After 10 cycles. (b) After 100 cycles. (c) After 1000 cycles.

Figure D.7: Pixel intensity using DI_{energy} and $f_c = 250kHz$.

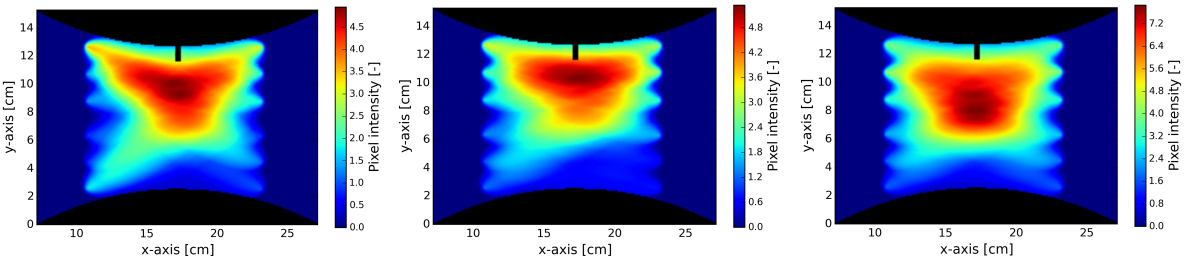

(a) After 10 cycles. (b) After 100 cycles. (c) After 1000 cycles.

Figure D.8: Pixel intensity using DI_{energy} and $f_c = 300kHz$.

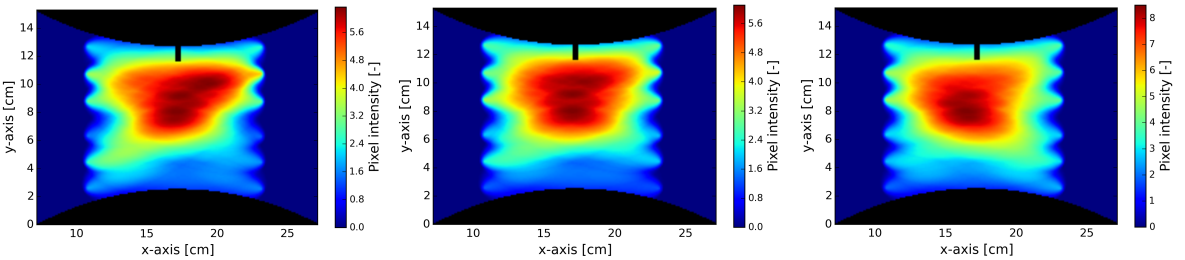

(a) After 10 cycles. (b) After 100 cycles. (c) After 1000 cycles.

Figure D.9: Pixel intensity using DI_{energy} and $f_c = 450kHz$.

D.3. Change in Pixel Intensity: $DI_{pearson}$

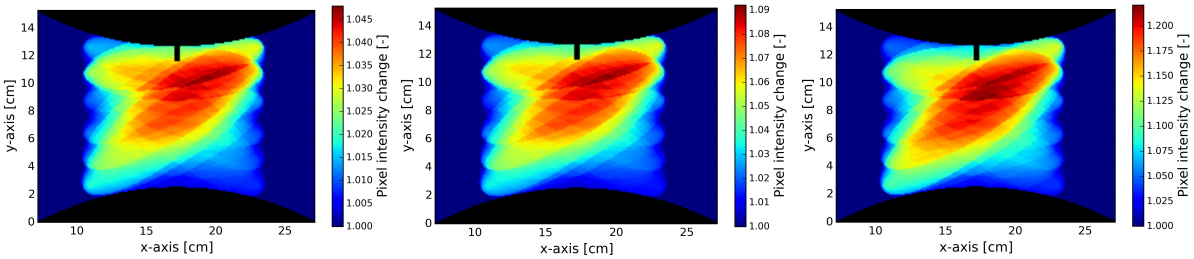

(a) After 10 cycles. (b) After 100 cycles. (c) After 1000 cycles.

Figure D.10: Change in pixel intensity using $DI_{pearson}$ and $f_c = 150kHz$.

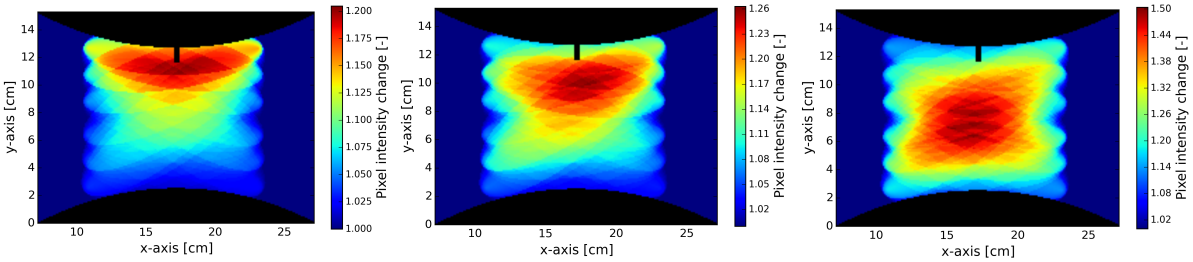

(a) After 10 cycles. (b) After 100 cycles. (c) After 1000 cycles.

Figure D.11: Change in pixel intensity using $DI_{pearson}$ and $f_c = 250kHz$.

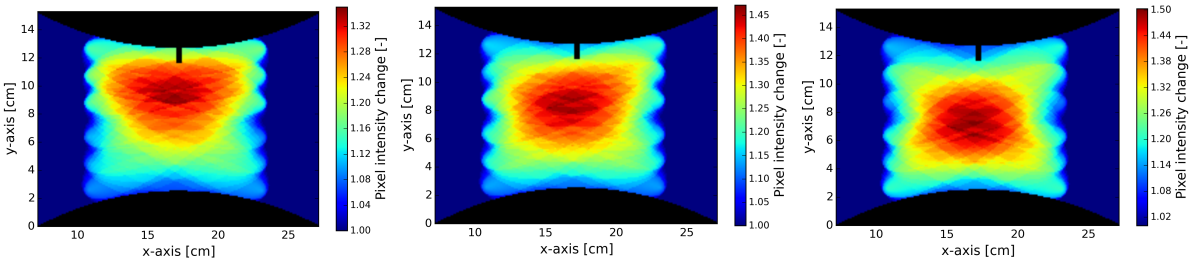

(a) After 10 cycles. (b) After 100 cycles. (c) After 1000 cycles.

Figure D.12: Change in pixel intensity using $DI_{pearson}$ and $f_c = 300kHz$.

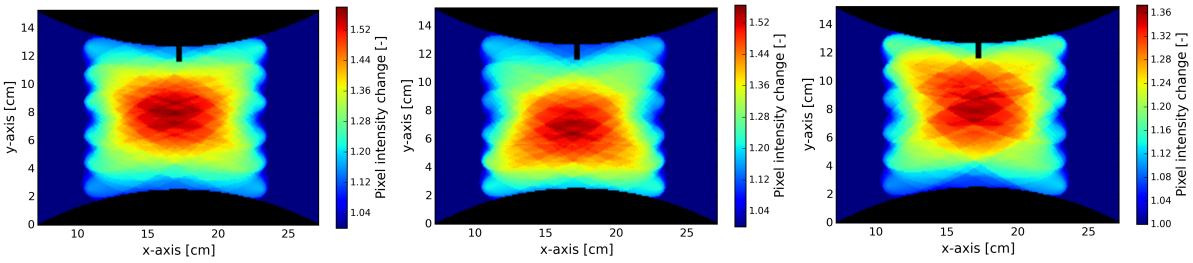

(a) After 10 cycles. (b) After 100 cycles. (c) After 1000 cycles.

Figure D.13: Change in pixel intensity using $DI_{pearson}$ and $f_c = 450kHz$.

D.4. Change in Pixel Intensity: DI_{energy}

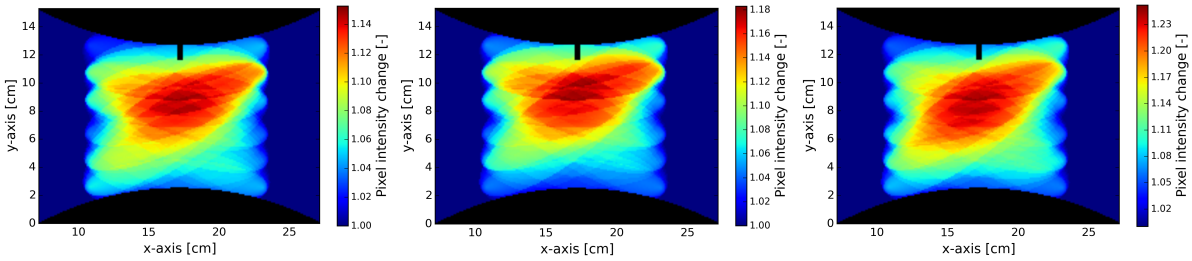

(a) After 10 cycles. (b) After 100 cycles. (c) After 1000 cycles.

Figure D.14: Change in pixel intensity using DI_{energy} and $f_c = 150kHz$.

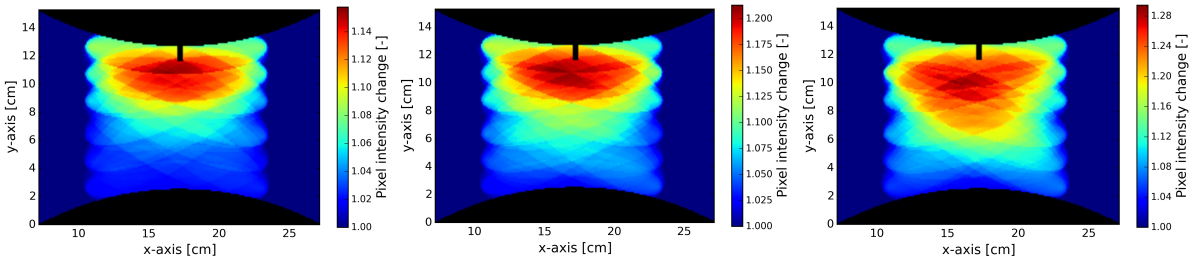

(a) After 10 cycles. (b) After 100 cycles. (c) After 1000 cycles.

Figure D.15: Change in pixel intensity using DI_{energy} and $f_c = 250kHz$.

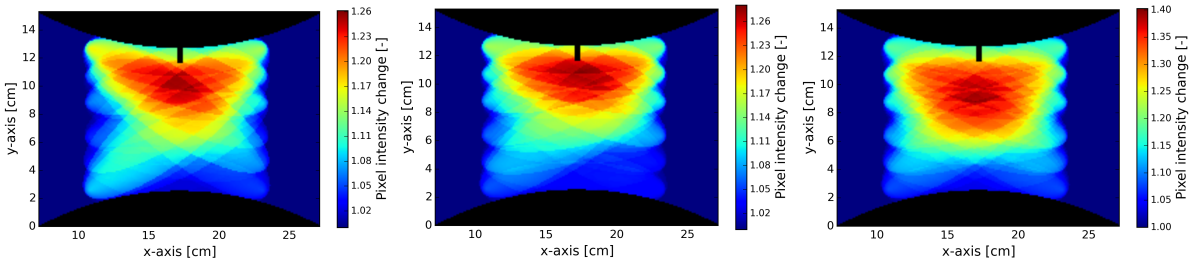

(a) After 10 cycles. (b) After 100 cycles. (c) After 1000 cycles.

Figure D.16: Change in pixel intensity using DI_{energy} and $f_c = 300kHz$.

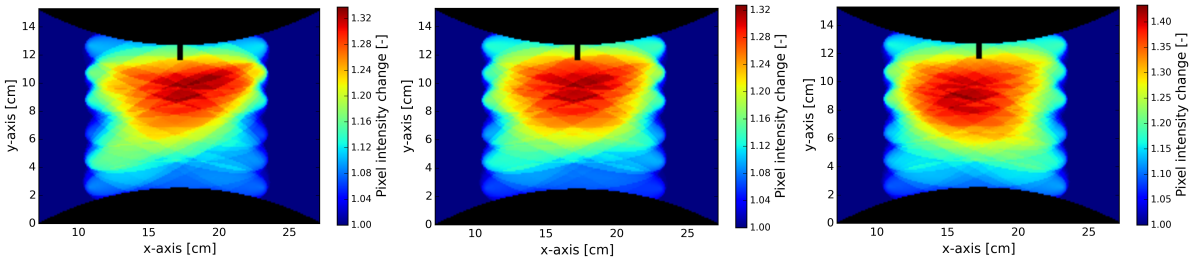

(a) After 10 cycles. (b) After 100 cycles. (c) After 1000 cycles.

Figure D.17: Change in pixel intensity using DI_{energy} and $f_c = 450kHz$.

E

Manufacturing of Test Panels

This Appendix discusses the manufacturing of the test panels used for the case study presented in Chapter 5.

E.1. Skin panel specification according to Boeing

Table E.1: Skin panel specifications provided in the SRM [26].

Ply	Direction	Material
P1	-	N0006681 | COCURED SUFRACER FILM AS GIVEN IN BMS 8-341 TYPE II GRADE 2 FORM 2 STYLE 2
P2*[1]	0 or 90 degrees	N0004777 | CARBON FIBER REINFORCED EPOXY SHEET AS GIVEN IN BMS 8-276 TYPE 40 CLASS 5 STYLE 6K-70-PW-PB4 FORM 1 COMPOSITION LEVEL 2
P3*[2]	0 or 90 degrees	N0004775 | CARBON FIBER REINFORCED EPOXY SHEET AS GIVEN IN BMS 8-276 TYPE 40 CLASS 2 STYLE 6K-70-PW FORM 1 COMPOSITION LEVEL 2
P4	45 degrees	N0004771 | CARBON FIBER REINFORCED EPOXY SHEET AS GIVEN IN BMS 8-276 TYPE 35 CLASS 8 GRAD 190 FORM 3 COMPOSITION LEVEL 2
P5	90 degrees	
P6	-45 degrees	
P7	0 degrees	
Inner Plies*[3]	Not given*[3]	
P(n)*[4]	0 or 90 degrees	N0004775 | CARBON FIBER REINFORCED EPOXY SHEET AS GIVEN IN BMS 8-276 TYPE 40 CLASS 2 STYLE 6K-70-PW FORM 1 COMPOSITION LEVEL 2

*[1] P2 material applicable everywhere except under wing to body fairing.
*[2] P3 material applicable under wing to body fairing only.
*[3] Ply information for repairs will be provided upon request.
*[4] P(n) is the innermost ply

E.2. Panel manufacturing

The following equipment was utilised during the manufacturing process:

- Cutting table
- Layup table
- Autoclave
- Vacuum connectors
- Latex or nitrile gloves
- Rollers
- Rulers
- Stanley knives
- Tacky tape (vacuum pump)
- Vacuum sealer tape (autoclave)
- Vacuum film (debulking)
- Vacuum bag (autoclave)
- Glass fiber tows
- Woven dry glass fabric
- Peel ply
- Pre-pregs

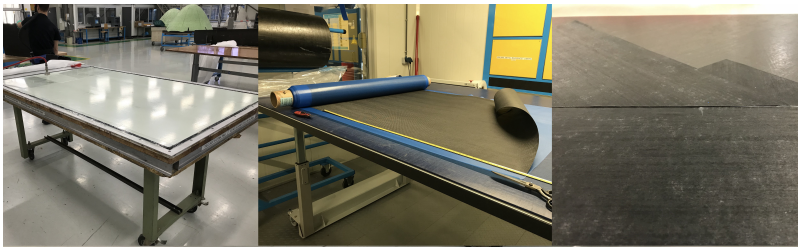

Figure E.1: Cutting pre-preg plies.

The following two pre-pregs have been used:

- CFRP epoxy sheet - BMS 8-276 Type 40 Class 2A Style 6K-70-PW Form 1 Composition Level 2: A woven carbon fiber pre-preg with 40% nominal resin content by weight and a handling life of 240 hours at $22 \pm 3^{\circ}C$.
- CFRP epoxy sheet - BMS 8-276 Type 35 Class 10 Grade 190 Form 3 Composition Level 2: This carbon fiber pre-preg has a 35% nominal resin content by weight and functions as an alternative to the Class 8 material which is suited for the automated tape laying equipment. Its handling life is 240 hours as well.

The skin panel, starting with P1, was laid up on a $100cmx100cm$ area according to Table 5.1. A metal worktable was cleaned, covered with a vacuumfilm and connected to a vacuumpump to provide a smooth surface for the laminate's lay up process. Following, each ply was cut under the right angle after which the plastic protection sheet on the pre-preg ply was removed, as in Figure E.1.

Each ply was carefully positioned (onto the previous layers) while avoiding too much tension onto the ply as this can cause the ply to fold or fracture. First a red plastic peel ply and second a piece of glass fiber fabric was placed on top of the layer. A vacuum film was used to cover the laminate and the vacuum pump was connected to debulk the layup, while making sure there was no bridging of bagging material. This ensures that the pre-preg plies have no residual air trapped in between them, thereby avoiding voids in the panel. Debulking was repeated for every ply as shown in Figure E.2.

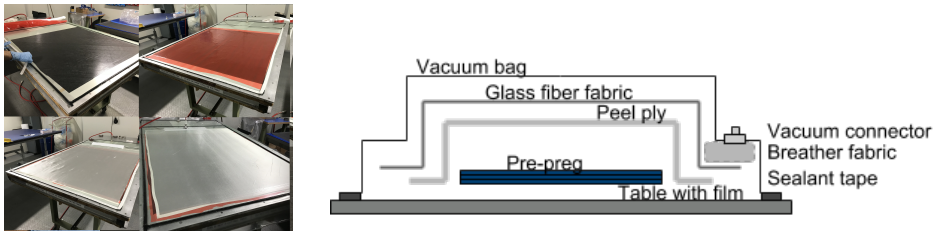

Figure E.2: Debulking of the laminate.

The laminate was cut into two obtaining two panels, $50cmx100cm$. They were placed on either side of a metal plate and wrapped in peel ply, glass fiber and breather fabric. Glass fiber rovings were placed at the corner of the panel to make contact with the breather fabric, allowing gas and resin to flow easier out of the laminate during autoclaving, Figure E.3. Hereafter, the panels were sealed using a vacuum bag and tested for leakage by first applying a vacuum of $900mbar$ and by reviewing the pressure loss over several minutes. The panel was then put into the autoclave and cured using the curing cycle taken from the Boeing Material Specification (BMS) document, as can be seen in Figure E.4 [81].

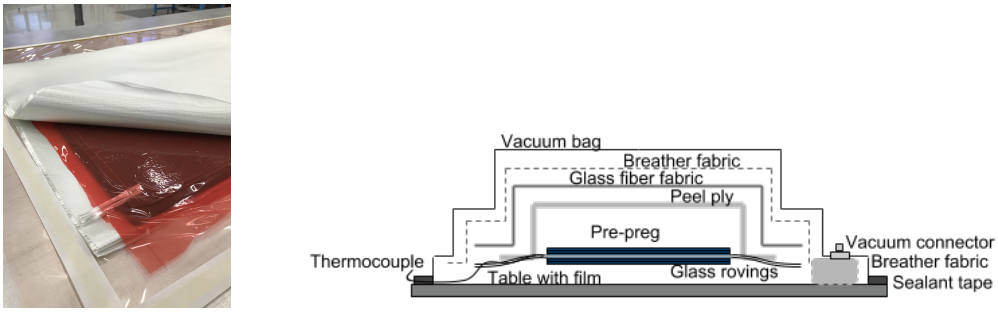

Figure E.3: Bagging panels for autoclaving.

F1 Apply $745 mbar$ minimum vacuum to the bag.

F2 Pressurize the autoclave to $5.86 bar$. When the pressure reaches $138 + 0.69/-0 bar$, vent the vacuum bag to atmosphere. Keep the bag vented until the end of the cure. Pressure under the vacuum bag shall be $0 + 0.344/-0 bar$ throughout the remainder of the cure cycle.

F3 Start applying heat after full pressurization of the autoclave.

F4 The heat-up rate shall be $0.56 to 2.78 ^\circ C/minute$.

F5 Hold for $120+60/-0 min$ at $179 \pm 5.56 ^\circ C$ and $5.86+0.69/-0 bar$. Keep temperature based on the lagging thermocouple. Curing begins when the last thermocouple reaches the minimum curing temperature. All thermocouples shall remain in cure temperature range.

F6 Cool the part under pressure until its temperature reaches $60 ^\circ C$ or below. A natural pressure drop of max $1.31 bar$ in the autoclave due to cool down is allowed. Cool-down rate shall be $2.78 ^\circ C/minute$ maximum.

F7 When part temperature reaches below 60°, release pressure and remove part.

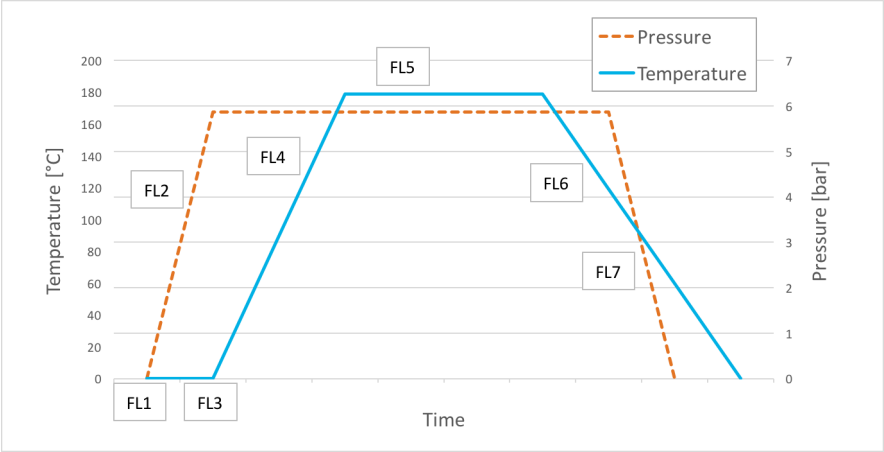

Figure E.4: BMS8-276 cure cycle [81].

F

Bonding procedure of PZT sensors

This Appendix discusses the bonding procedure of the PZT disc sensors, which is based on the procedure provided by *ir. P.A. Viegas Ochoa de Carvalho*.

F.1. Equipment

The following equipment was utilised during the bonding process:

- Nitrile gloves
- Isopropanol
- Distilled water
- Paper cleaning tissues
- Ruler
- Pencil
- Sanding paper K240
- Adhesive tape
- Teflon films
- PZT discs
- Metallic pincer
- Cyanoacrylate glue Z70
- Soldering tabs
- Soldering iron
- Soldering tin
- Electrical wires (one strand)
- (Propanone)

F.2. Procedure

1. Always wear the nitrile gloves.
2. Mark the positions of the PZT sensors.
3. Clean the bond area with isopropanol using paper tissues. Clean in a circular motion and end the process by cleaning in two directions forming a cross (swipe the location once, forming a cross).
4. Place some distilled water on the bond area.
5. Sand the panel in a circular motion.
6. Clean the sanded area using isopropanol and paper tissues again as in step 3.
7. Place the PZT disc and soldering tap onto a teflon film using the pincer.
8. Apply adhesive tape to the PZT and soldering tap while making one fold at the end of the tape.
    - Place the terminal points in a convenient direction for measuring.
    - Make sure to apply enough pressure to adhere the PZT and soldering tab to the tape.
9. Align the PZT with the marked position.
10. Place the PZT and soldering tab to the panel.
11. Places adhesive tape around the sensor location to prevent glue from leaking/spreading onto the panel.
12. Lift the adhesive tape holding the PZT and soldering tab, while keeping one side attached to the panel.
13. Apply the cyanoacrylate Z70 glue to the PZT's and soldering tab's surface. Avoid bubbles on the regions to be glued.
14. Bond the PZT and soldering tab to the surface by folding the adhesive tape back into position. Apply pressure to the PZT and soldering tab using a teflon film. Apply pressure for $\approx 2min$.
15. Remove all tape from the surface using pincers.
16. Use the soldering iron to connect the soldering tab to the PZT. Make sure that all the wires the terminal point in the same direction so avoid mistakes while measuring.
17. (In case the PZT or soldering tab needs to be removed due to a mistake, it can be removed from the panel using propanone and a very sharp and thin knife. Always be careful not to damage the panel.)

G

Experimental Signal Processing

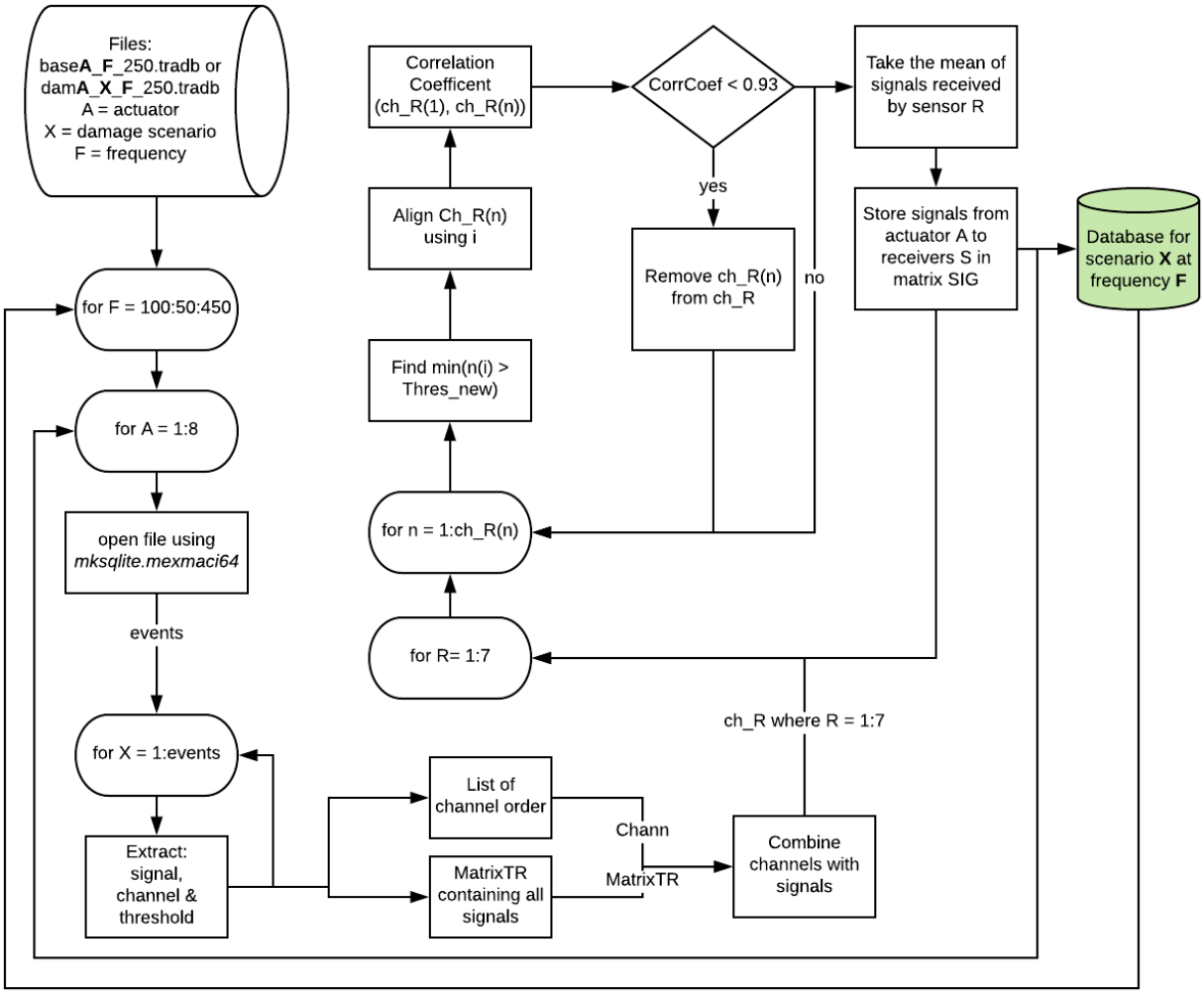

Figure G.1: Flowchart of signal processing as performed by the file: *'experimental_signal_processing.mat'*.

Blind QSI: NDT Inspections

This appendix shows the results of the A-scan, X-ray and C-scan results for the panel subjected to the blind QSI tests discussed in Sections 5.4.2 & 5.5.1.

H.1. A-scan

Figure H.1: A-scan at location of the indenter prior to blind QSI of 5mm.

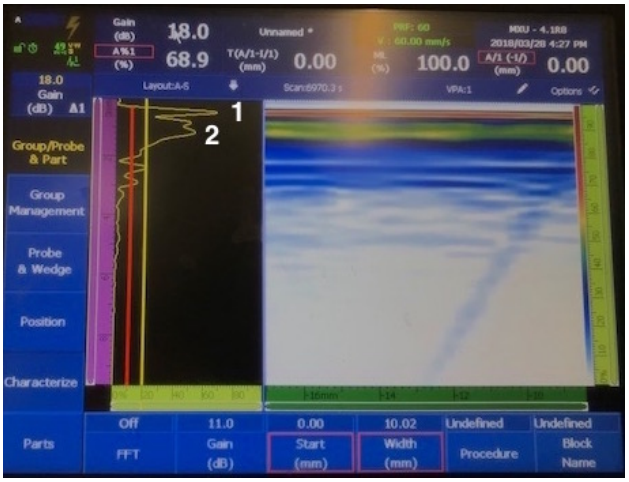

Figure H.2: A-scan at location of the indenter after blind QSI of 5mm.

H.2. X-ray

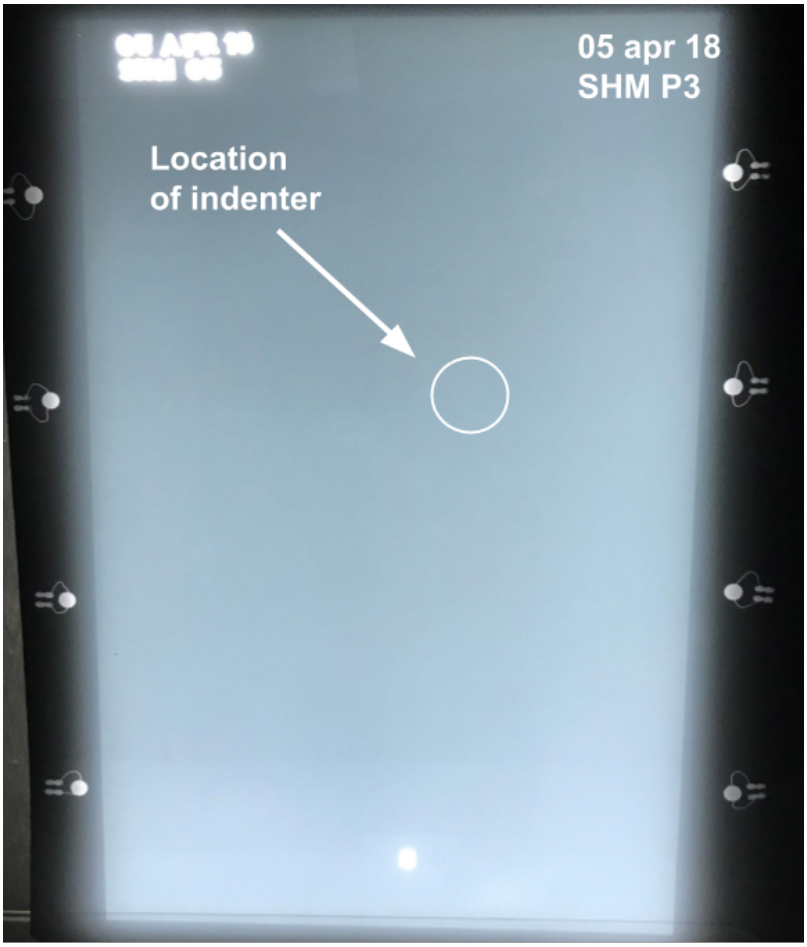

Figure H.3: Picture taken of the X-ray film placed inside the light box. The X-ray covered the inspection area only and was taken after the blind QSI of 5mm. The circle indicates the location of the indenter. No indication of damage is visible.

H.3. C-scan

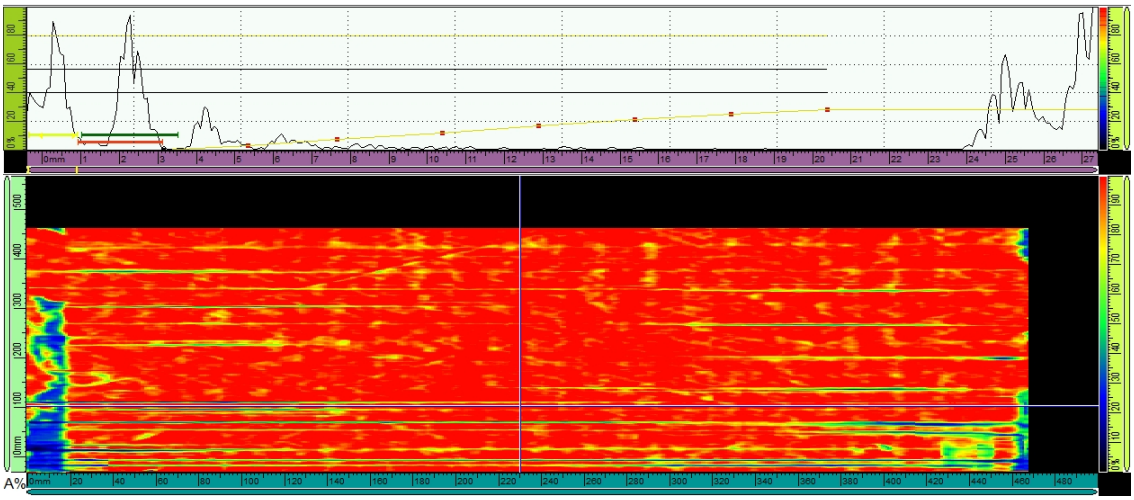

Figure H.4: C-scan taken of full panel prior to sensor attachment and the blind QSI of 5mm.

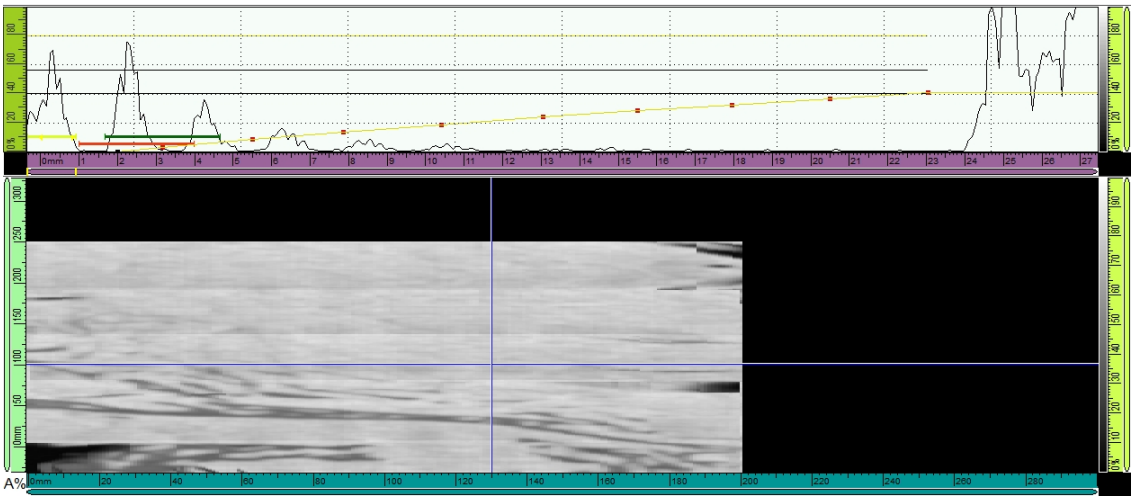

Figure H.5: C-scan taken of the inspection area between the sensors after blind QSI of 15.5mm.

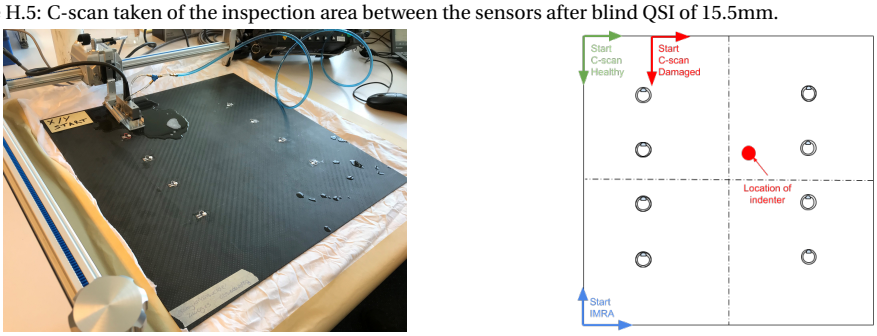

Figure H.6: C-scans were taken prior to and after blind QSI test. Note that the bottom left corners on the images are the top left corner with respect to the reconstructed images. This is were the C-scan was started.

Data AE Monitoring

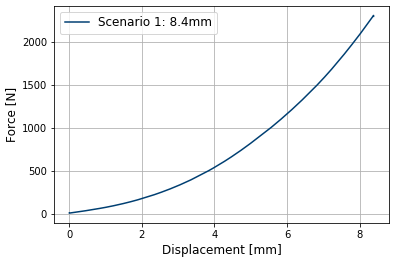

(a) Force-displacement curve.

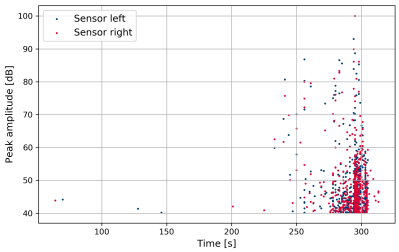

(b) AE.

Figure I.1: Scenario 1: Maximum displacement = 8.4mm & maximum load = 2310N.

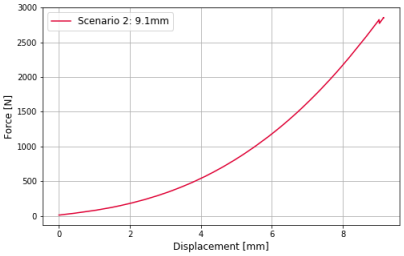

(a) Force-displacement curve.

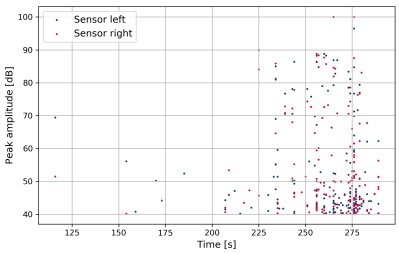

(b) AE.

Figure I.2: Scenario 2: Maximum displacement = 9.1mm & maximum load = 2860N.

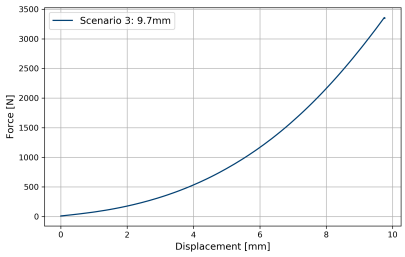

(a) Force-displacement curve.

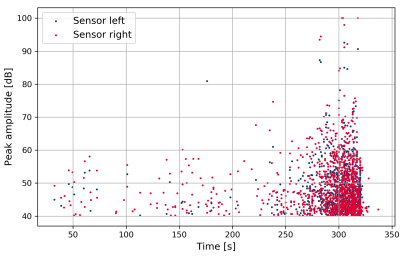

(b) AE.

Figure I.3: Scenario 3: Maximum displacement = 9.7mm & maximum load = 3360N.

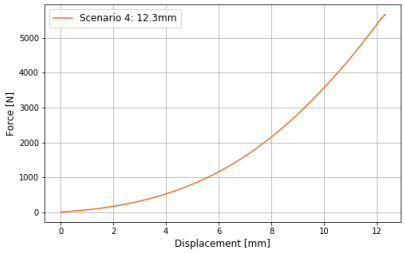

(a) Force-displacement curve.

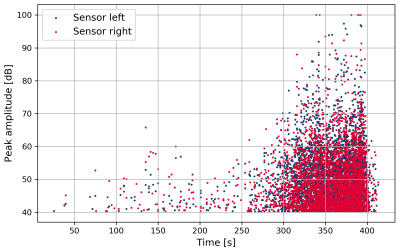

(b) AE.

Figure I.4: Scenario 4: Maximum displacement = 12.3mm & maximum load = 5670N.

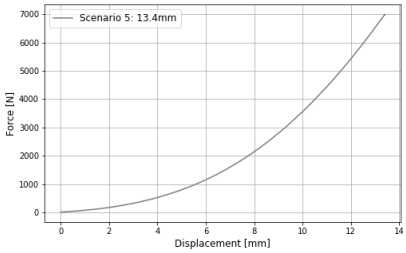

(a) Force-displacement curve.

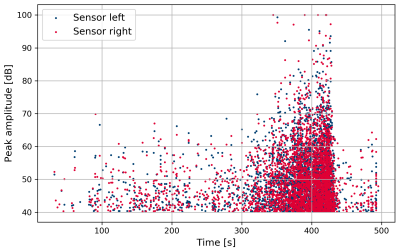

(b) AE.

Figure I.5: Scenario 5: Maximum displacement = 13.4mm & maximum load = 6990N.

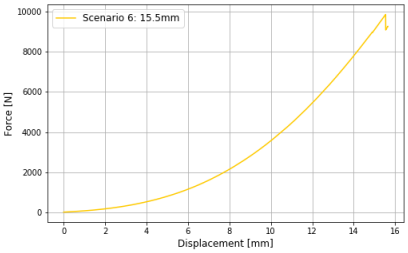

(a) Force-displacement curve.

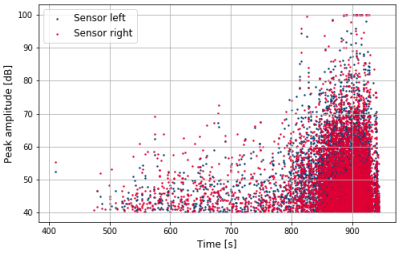

(b) AE.

Figure I.6: Scenario 6: Maximum displacement = 15.5mm & maximum load = 9860N.

J

QSI with AE: NDT Inspections

This appendix shows the results of the x-ray and C-scan results for the panel subjected to multiple QSI tests discussed in Sections 5.4.3 & 5.5.2.

J.1. X-ray

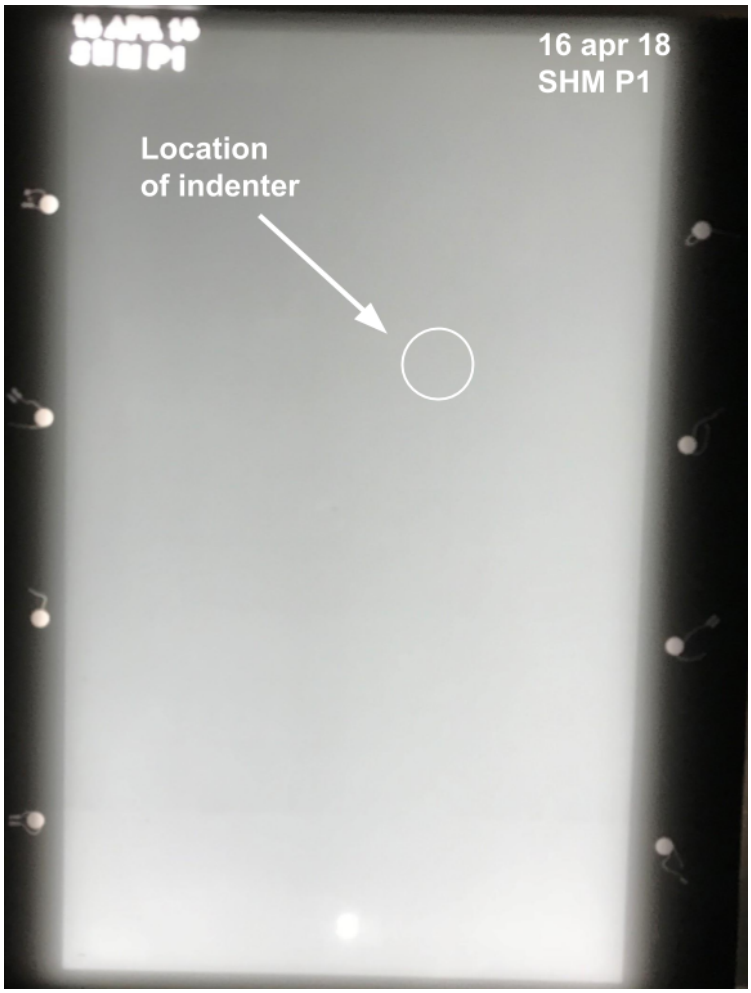

Figure J.1: Picture taken of the X-ray film placed inside the light box. The X-ray covered the inspection area only and was taken after the blind QSI of 15.5mm (damage scenario 6). The circle indicates the location of the indenter. The X-ray does not contain any indications of damage.

J.2. C-scan

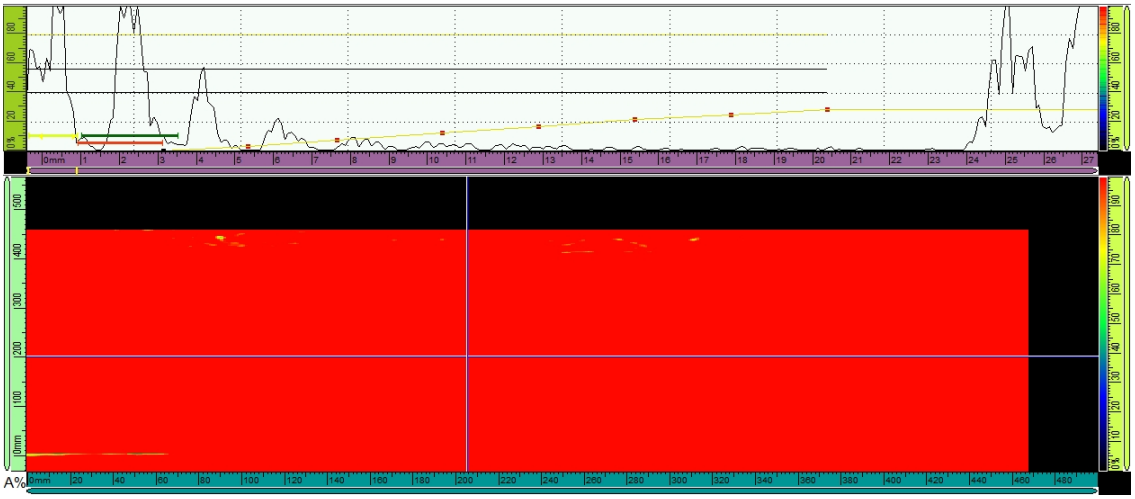

Figure J.2: C-scan taken of full panel prior to sensor attachment.

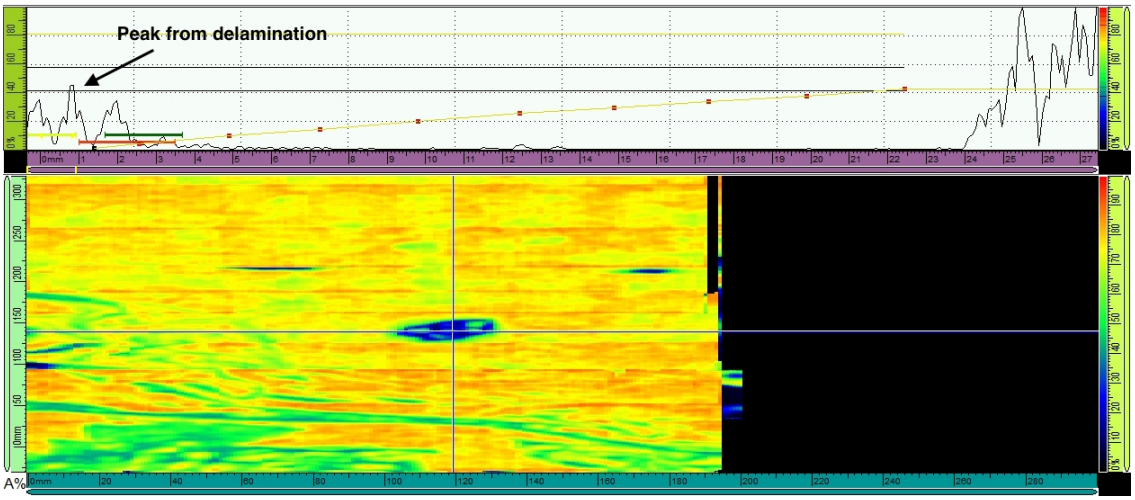

Figure J.3: C-scan taken of the inspection area/area of interest after scenario 6.

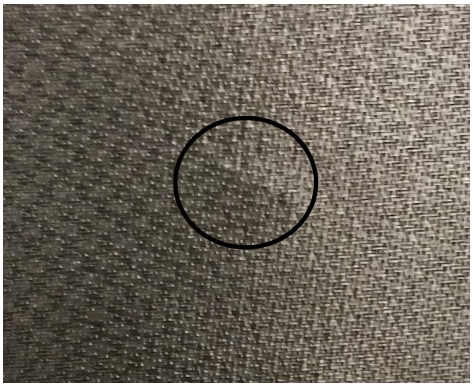

Figure J.4: Crack visible on bottom side of the test panel

K

Case Study: Additional Results

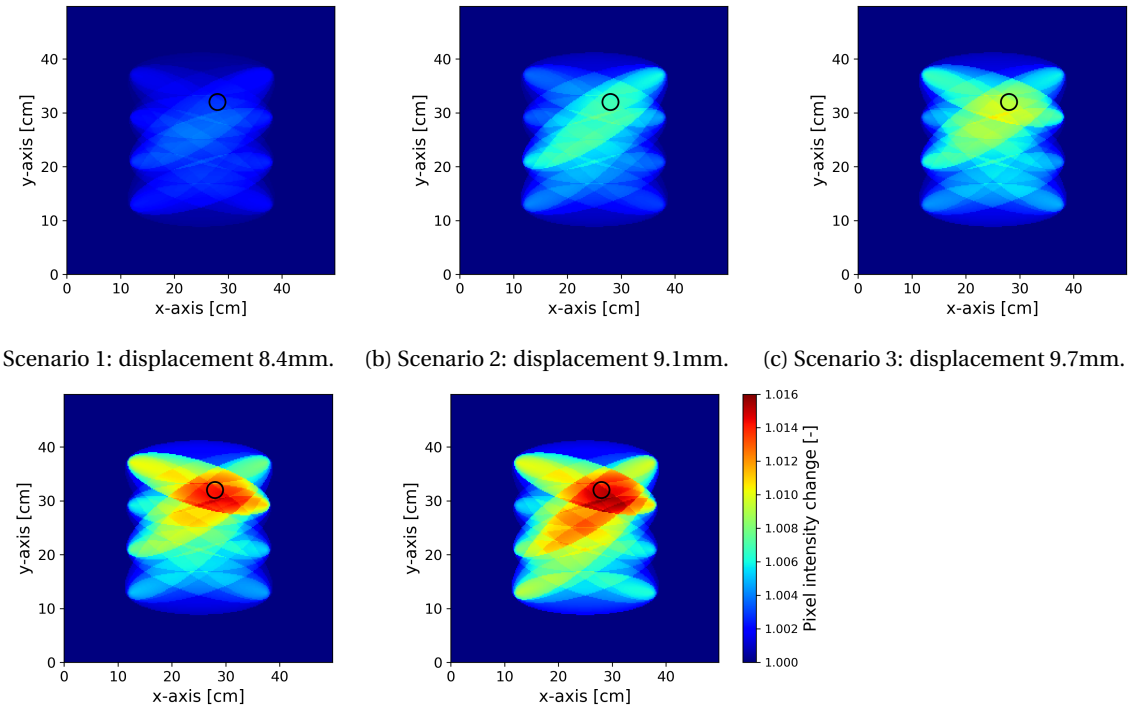

(a) Scenario 1: displacement 8.4mm. (b) Scenario 2: displacement 9.1mm. (c) Scenario 3: displacement 9.7mm.

(d) Scenario 5: displacement 12.3mm. (e) Scenario 5: displacement 13.4mm.

Figure K.1: Change in pixel intensity: Scenario 1-5 for $f_c = 150kHz$ and $DI_{pearson}$.

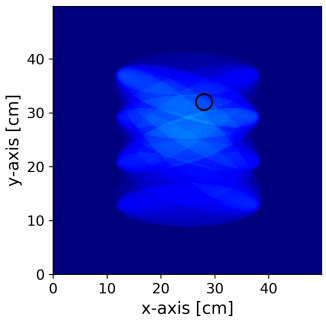

(a) Scenario 1: displacement 8.4mm.

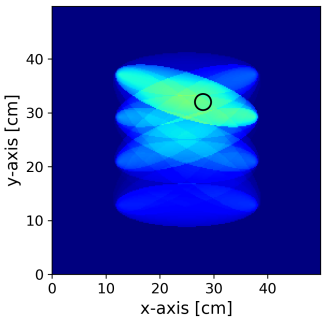

(b) Scenario 2: displacement 9.1mm.

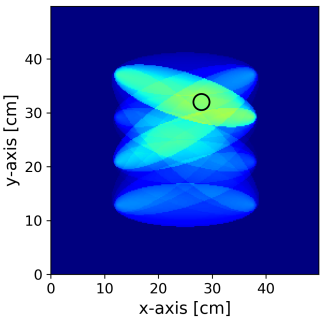

(c) Scenario 3: displacement 9.7mm.

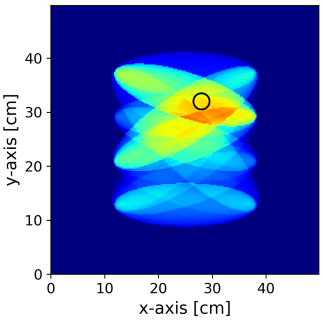

(d) Scenario 5: displacement 12.3mm.

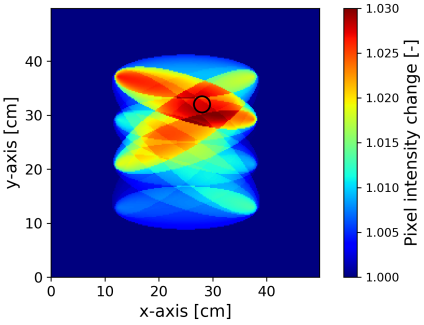

(e) Scenario 5: displacement 13.4mm.

Figure K.2: Change in pixel intensity: Scenario 1-5 for $f_c = 150kHz$ and DI_{energy}.

Bibliography

[1] T. Cooper, J. Smiley, C. Porter, and C. Precours. Global fleet & mro market forecast summary 2017-2027. http://www.oliverwyman.com/content/dam/oliver-wyman/v2/publications/2017/feb/2017%20Global%20Fleet%20MRO%20Market%20Forecast%20Summary%20Final_Short%20Version_1.pdf. [Online; accessed 2017-08-08].

[2] V. Giurgiutiu. *Structural Health Monitoring of Aerospace Composites*. Academic Press, 2015.

[3] Rùnar UnnÞòrsson, MT Jonsson, and TP Runarsson. Ndt methods for evaluating carbon fiber composites. *Proceedings of the Composites Testing and Model Identification, Bristol, UK*, pages 21–23, 2004.

[4] SAE International. ARP6461 guidelines for implementation of structural health monitoring of fixed wing aircraft, 2013.

[5] H. Speckmann and H. Roesner. Structural health monitoring: a contribution to the intelligent aircraft structures in proc. of ecndt 2006, 9th european conference on ndt, berlin, germany, 2006.

[6] K. Worden, C. Farrar, G. Manson, and G. Park. The fundamental axioms of structural health monitoring. *Proceedings of a royal society*, 463:1639–1664, 2007.

[7] R. Demir. 2015 global mro market forecast and key trends. https://www.slideshare.net/reyyandemir/global-fleet-and-mro-market-forecast-trends-and, 2015. [Online; accessed 2017-08-12].

[8] C. Farrar and K. Worden. *Structural Health Monitoring: A Machine Learning Perspective*. John Wiley and Sons, first edition, 2012.

[9] K. Worden, E.J. Cross, N. Dervilis, E. Papatheou, and I. Antoniadou. Structural health monitoring: from structures to systems-of-systems. *IFAC-PapersOnLine*, 48(21):01–17, 2015.

[10] C. Boller. Structural health monitoring - an introduction and definitions. In C. Boller, F. Chang, and Y. Fujino, editors, *Encyclopedia of Structural Health Monitoring*, chapter 1, pages 1–23. Jonh Wiley and Sons, 2009.

[11] T. Tinga. *Principle of Loads and Failure Mechanisms: Applications in Maintenance, Reliability and Design*. Springer, first edition, 2007.

[12] Air Transport Association of America INC. Ata msg-3 operator/manufacturer scheduled maintenance development. https://www.easa.europa.eu/download/imrbpb/IP92and103combined%20final%20version.pdf, 2011. [Online; accessed: 2017-07-25].

[13] D. Piotrowski, D. Roach, A. Melton, J. Bohler, T. Rice, S. Neidigk, and J. Linn. Implementation of structureal health monitoring (shm) into an airline maintenance program, 2014.

[14] A. Saxena, K. Goebel, C.C. Larrosa, and F-K. Chang. Cfrp composites data set. http://ti.arc.nasa.gov/project/prognostic-data-repository. Online; accessed: 2018-10-01.

[15] N. Hussain. Structural health monitoring and its role in affordability. Presentation at IWSHM 2015, Standford, USA, 2015.

[16] C. Boller. Implementation strategies for shm in civil and military applications. In A. Suleman, editor, *Structural Health Monitoring of Military Vehicles*, page 21. Nato Science and Technology organization, 2014.

[17] H. Kapoor, C. Braun, and C. Boller. Modelling and optimisation of maintenance intervals to realize structural health monitoring applications on aircraft. In F. Casciato and M. Giordano, editors, *Fifth European Workshop on Structural Health Monitoring 2010*, pages 55–62. 2010.

[18] Pedro Ochôa, Virgínia Infante, José M Silva, and Roger M Groves. Detection of multiple low-energy impact damage in composite plates using lamb wave techniques. *Composites Part B: Engineering*, 80:291–298, 2015.

[19] F. Smith. The use of composites in aerospace: Past, present and future challenges, avalon consultancy services ltd. https://avaloncsl.files.wordpress.com/2013/01/avalon-the-use-of-composites-in-aerospace-v2.pdf, 2013. [Online; accessed 2017-08-08].

[20] K. Diamanti and C. Soutis. Structural health monitoring techniques for aircraft composite structures. *Progress in Aerospace Sciences*, 46:342–352, 2010.

[21] Composite materials: Repairing the "black gold", part 1. https://www.lufthansa-technik.com/composite-materials-repair-1. Online; Access: 2018-02-19.

[22] Ground operations occurrences at australian airports 1998 to 2008, the australian transport safety bureau. https://www.atsb.gov.au/media/1529837/ar2009042.pdf, 2010. [Online; accessed 2017-08-05].

[23] G. Gardiner. Primary structure repair: The quest for quality. https://www.compositesworld.com/articles/primary-structure-repair-the-quest-for-quality, 2011. [Online; accessed 2017-08-15].

[24] R.M Groves. 3.12 inspection and monitoring of composite aircraft structures. In Peter W.R. Beaumont and Carl H. Zweben, editors, *Comprehensive Composite Materials {II}*, pages 300 – 311. Elsevier, Oxford, 2018.

[25] D. Roach and S. Neidigk. Does the maturity of structural health monitoring technology match user readiness? in: Proceedings of the 8th iwshm international workshop on structural health monitoring. http://web.stanford.edu/group/sacl/workshop/documents/Keynote%20presentations/IWSHM%202011%20Keynote_Dennis%20Roach.pdf, 2011. [Online; accessed 2017-08-08].

[26] The Boeing Company. B787-9 structural repair manual. Technical report, 2014.

[27] Derek Hull and Yi Bing Shi. Damage mechanism characterization in composite damage tolerance investigations. *Composite Structures*, 23(2):99–120, 1993.

[28] T.-W. Shyr and Y.-H. Pan. Impact resistance and damage characteristics of composite laminates. *Composite Structures*, 62:193–203, 2003.

[29] M De Freitas, A Silva, and L Reis. Numerical evaluation of failure mechanisms on composite specimens subjected to impact loading. *Composites Part B: Engineering*, 31(3):199–207, 2000.

[30] B.-W. Jang and C.-G. Kim. Real-time detection of low-velocity impact-induced delamination onset in composite laminates for efficient management of structural health. *Composites Part B*, 123(3):124–135, 2017.

[31] D.G. Aggelis, N.-M. Barkoula, T.E. Matikas, and A.S. Paipetis. Acoustic structural health monitoring of composite materials: Damage identification and evaluation in cross ply laminates using acoustic emission and ultrasonics. *Composites Science and Technology*, 72:1127–1133, 2011.

[32] R.M. Groves and M.C.M. Bakker. Ae4asm108 reader, experimental techniques & non-destructive testing. 2016-2017.

[33] Nieuwland R. Guest lecture ae4asm108 (2016-2017): Lecture – fiber optic sensing.

[34] H. Tsuda. Ultrasound and damage detection in cfrp using fiber bragg grating sensors. *Composites science and technology*, 66(5):676–683, 2006.

[35] PT Coverley and W.J. Staszweski. Impact damage location in composite structures using optimized sensor triangulation procedure. *Smart materials and structures*, 12(5):795–803, 2003.

[36] L Draudvilienė and L Mažeika. Analysis of the zero-crossing technique in relation to measurements of phase velocities of the s0 mode of lamb waves. *Ultragarsas" Ultrasound"*, 65(3):11–14, 2010.

[37] F. Ciampa and M. Meo. A new algorithm for acoustic emission localization and flexural group velocity determination in anisotropic structures. *Composites Part A: Applied Science and Manufacturing*, 41(12):1777–1786, 2010.

[38] Y. Sai, M. Jiang, Q. Sui, S. Lu, and L. Jia. Composite plate low energy impact localization system based on fbg sensing network and hybrid algorithm. *Optical Fiber Technology*, 24:84–88, 2015.

[39] E. Kirkby, R. De Oliveira, V. Michaud, and J.A. Månson. Impact localisation with fbg for a self-healing carbon fibre composite structure. *Composite Structures*, 94(1):8–14, 2011.

[40] P. Shrestha, J.H. Kim, P. Yurim, and C.G. Kim. Impact localization on composite structure using fbg sensors and novel impact localization technique based on error outliers. *Composite Structures*, 142(Supplement C):263 – 271, 2016.

[41] S. Lu, M. Jiang, Q. Sui, Y. Sai, and L. Jia. Damage identification system of cfrp using fiber bragg grating sensors. *Composite Structures*, 125:400–406, 2015.

[42] J. Frieden, J. Cugnoni, J. Botsis, and T. Gmur. Low energy impact damage monitoring of composites using dynamic strain signals from fbg sensors – part i: Impact detection and localization. *Composite Structures*, 94:438–445, 2012.

[43] H. Zhao, X.and Gao, G. Zhang, B. Ayhan, F. Yan, C. Kwan, and J.L. Rose. Active health monitoring of an aircraft wing with embedded piezoelectric sensor/actuator network: I. defect detection, localization and growth monitoring. *Smart materials and structures*, 16(4):1208, 2007.

[44] D. Wang, L. Ye, Y. Lu, and F. Li. A damage diagnostic imaging algorithm based on the quantitative comparison of lamb wave signals. *Smart materials and structures*, 19(6), 2010.

[45] A. De Fenza, G. Petrone, and M. Pecora, R.and Barile. Post-impact damage detection on a winglet structure realized in composite material. *Composite Structures*, 169:129–137, 2017.

[46] M. Hettler, J.and Tabatabaeipour, S. Delrue, and K. Van Den Abeele. Linear and nonlinear guided wave imaging of impact damage in cfrp using a probabilistic approach. *Materials*, 9(11), 2016.

[47] G. Petculescu, S. Krishnaswamy, and J.D. Achenbach. Group delay measurements using modally selective lamb wave transducers for detection and sizing of delaminations in composites. *Smart Materials and Structures*, 17(1):015007, 2007.

[48] I. Trendafilova, R. Palazzetti, and A. Zucchelli. Damage assessment based on general signal correlation. application for delamination diagnosis in composite structures. *European Journal of Mechanics-A/Solids*, 49:197–204, 2015.

[49] U. Polimeno and M. Meo. Detecting barely visible impact damage detection on aircraft composites structures. *Composite structures*, 91(4):398–402, 2009.

[50] Intro to guided waves. `http://www.gwultrasonics.com/knowledge/gw-intro/`. Online; accessed: 2018-10-03.

[51] Lord Rayleigh. On waves propagated along the plane surface of an elastic solid. *Proceedings of the London Mathematical Society*, 1(1):4–11, 1885.

[52] Rayleigh wave. `https://earthquake.usgs.gov/learn/glossary/?term=Rayleigh%20wave`. [Online; accessed 2017-09-16].

[53] Z. Su and L. Ye. *Identification of Damage Using Lamb Waves: From Fundamentals To Applications*. Springer, 2014.

[54] B. Alem and K. Abedian, A.and Nasrollahi-Nasab. Reference-free damage identification in plate-like structures using lamb-wave propagation with embedded piezoelectric sensors. *Journal of Aerospace Engineering*, 29(6), 2016.

[55] K Diamanti and C Soutis. Structural health monitoring techniques for aircraft composite structures. *Progress in Aerospace Sciences*, 46(8):342–352, 2010.

[56] Pawel Kudela, Maciej Radzienski, and Wieslaw Ostachowicz. Impact induced damage assessment by means of lamb wave image processing. *Mechanical Systems and Signal Processing*, 102:23–36, 2018.

[57] Yassin Alkassar, VK Agarwal, and Eman Alshrihi. Simulation of lamb wave modes conversions in a thin plate for damage detection. *Procedia Engineering*, 173:948–955, 2017.

[58] V Memmolo, E Monaco, ND Boffa, L Maio, and F Ricci. Guided wave propagation and scattering for structural health monitoring of stiffened composites. *Composite Structures*, 184:568–580, 2018.

[59] Abhinav Saxena, Kai Goebel, Cecilia C Larrosa, Vishnuvardhan Janapati, Surajit Roy, and Fu-Kuo Chang. Accelerated aging experiments for prognostics of damage growth in composite materials. Technical report, NATIONAL AERONAUTICS AND SPACE ADMINISTRATION MOFFETT FIELD CA AMES RESEARCH CENTER, 2011.

[60] H Gao, Y Shi, and JL Rose. Guided wave tomography on an aircraft wing with leave in place sensors. In *AIP Conference Proceedings*, volume 760, pages 1788–1794. AIP, 2005.

[61] V. Memmolo, F. Ricci, N.D. Boffa, L. Maio, and E. Monaco. Structural health monitoring in composites based on probabilistic reconstruction techniques. *Procedia Engineering*, 167:48–55, 2016.

[62] Z Sharif-Khodaei and MH Aliabadi. Assessment of delay-and-sum algorithms for damage detection in aluminium and composite plates. *Smart materials and structures*, 23(7):075007, 2014.

[63] Ching-Tai Ng and M Veidt. A lamb-wave-based technique for damage detection in composite laminates. *Smart materials and structures*, 18(7):074006, 2009.

[64] Jennifer E Michaels. Ultrasonic structural health monitoring: strategies, issues, and progress. In *Smart Sensor Phenomena, Technology, Networks, and Systems 2008*, volume 6933, page 69330Z. International Society for Optics and Photonics, 2008.

[65] J. Tang Tian Le. Manufacturing a fuselage panel of the boeing 787 dreamliner. Master's thesis, Inholland University of Applied Sciences, 2016.

[66] Bing Li, Lin Ye, Zheng Li, Zhaoyang Ma, and Hamed Kalhori. Quantitative identification of delamination at different interfaces using guided wave signals in composite laminates. *Journal of Reinforced Plastics and Composites*, 34(18):1506–1525, 2015.

[67] N Toyama, Y Kikushima, and J Takatsubo. Effect of delamination on lamb wave velocity in cross-ply laminates. *Journal of materials science letters*, 21(24):1891–1893, 2002.

[68] Fabrizio Ricci, Ernesto Monaco, Harsh Baid, and AK Mal. Guided waves in a disbonded honeycomb composite structure. *Structural Health Monitoring*, pages 910–917, 2013.

[69] N. Takeda, Y. Okabe, J. Kuwahara, and T. Kojima, S.and Ogisu. Development of smart composite structures with small-diameter fiber bragg grating sensors for damage detection: Quantitative evaluation of delamination length in cfrp laminates using lamb wave sensing. *Composite Science and Technology*, 65:2575–2587, 2005.

[70] M. Eckert. Boeing's plastic planes. `https://harpers.org/blog/2013/07/boeings-plastic-planes/`. Online; accessed: 2018-27-03.

[71] Gyuhae Park, Charles R Farrar, Francesco Lanza di Scalea, and Stefano Coccia. Performance assessment and validation of piezoelectric active-sensors in structural health monitoring. *Smart Materials and Structures*, 15(6):1673, 2006.

[72] Sumedha Moharana and Suresh Bhalla. A continuum based modelling approach for adhesively bonded piezo-transducers for emi technique. *International Journal of Solids and Structures*, 51(6):1299–1310, 2014.

[73] Behrouz Alem, Ali Abedian, and Komeil Nasrollahi-Nasab. Reference-free damage identification in plate-like structures using lamb-wave propagation with embedded piezoelectric sensors. *Journal of Aerospace Engineering*, 29(6):04016062, 2016.

[74] Yuichiro Aoki, Hiroshi Suemasu, and Takashi Ishikawa. Damage propagation in cfrp laminates subjected to low velocity impact and static indentation. *Advanced composite materials*, 16(1):45–61, 2007.

[75] Shaw Ming Lee and Paul Zahuta. Instrumented impact and static indentation of composites. *Journal of Composite Materials*, 25(2):204–222, 1991.

[76] Zeng Shen, YG Xu, and Andreas Chrysanthou. Contact behaviour of composite laminate under quasi-static indentation load. In *Key Engineering Materials*, volume 577, pages 545–548. Trans Tech Publ, 2014.

[77] G.A. Schoeppner and S. Abrate. Delamination threshold loads for low velocity impact on composite laminates. In *Composites Part A: Applied Science and Manufacturing*, volume 31, pages 903–915. 2000.

[78] SWF Spronk, Mathias Kersemans, JCA De Baerdemaeker, FA Gilabert, RDB Sevenois, D Garoz, C Kassapoglou, and Wim Van Paepegem. Comparing damage from low-velocity impact and quasi-static indentation in automotive carbon/epoxy and glass/polyamide-6 laminates. *Polymer Testing*, 65:231–241, 2018.

[79] Liping Huang, Liang Zeng, and Jing Lin. Baseline-free damage detection in composite plates based on the reciprocity principle. *Smart Materials and Structures*, 27(1):015026, 2017.

[80] Milad Saeedifar, Mehdi Ahmadi Najafabadi, Dimitrios Zarouchas, Hossein Hosseini Toudeshky, and Meisam Jalalvand. Clustering of interlaminar and intralaminar damages in laminated composites under indentation loading using acoustic emission. *Composites Part B: Engineering*, 144:206–219, 2018.

[81] BMS8-276. Technical report, The Boeing Company, 2017.